Sign-changing s-wave symmetry in iron-based superconductors: Manifestations and extensions

A DISSERTATION
SUBMITTED TO THE FACULTY OF THE GRADUATE SCHOOL
OF THE UNIVERSITY OF MINNESOTA
BY

Alberto Hinojosa Alvarado

IN PARTIAL FULFILLMENT OF THE REQUIREMENTS
FOR THE DEGREE OF
Doctor of Philosophy

Andrey V. Chubukov

December, 2016

Acknowledgements

There are many people that have greatly contributed to the completion of my graduate studies. I would like to thank my thesis advisor, Andrey Chubukov, for all I have learned from him and for his guidance and support throughout the years. Also special thanks to Saurabh Maiti for helping so much in my transition from high energy to condensed matter and to Dushko Kuzmanovski for very long and fruitful discussions.

I am also in debt to my fellow condensed matter theorists Yuxuan Wang, Sam Ducatman, Yuriy Sizyuk, and Xiaoyu Wang for many interesting conversations and continued friendship. Other invaluable friends in graduate school were Chris Anderson, Zach Billey, Cristian Martinez, Tim Lyon, and Lucas Morton. Without you my time in in graduate would have been indeed dull.

Finally, I want to thank Annie Pasbrig for her unconditional support in difficult times, my parents for helping me get to where I am, and the countless professors who inspired me both in high school, college, and graduate school.

Dedication

To my parents, for their unending support throughout the years.

Abstract

I perform theoretical studies of the family of iron-based superconductors, which are a group of materials that can achieve a relatively high critical temperature T_c. In most of these multi-band compounds the superconducting gap parameter has s-wave symmetry along the Fermi surfaces, but the sign of the gap can change between Fermi surfaces yielding the so-called s^{+-} symmetry. In this dissertation I focus on the experimental consequences of this gap structure and later on two of its possible extensions.

In the first part, I review how the resonance in inelastic neutron scattering can be explained as a pole in the spin susceptibility in an s^{+-} superconductor, computed using the random phase approximation. Then I extend the analysis to include the effect of pairing fluctuations and show that except in special cases these fluctuations merely shift the frequency of the resonance by a few percentage points. I also consider Raman spectroscopy experiments that measured the susceptibility in the B_{1g} symmetry channel and found a strong temperature dependence in the static part and a resonance below T_c in the dynamic part. I show how both of these can be explained through the coupling of fermions to spin fluctuations via the Aslamazov-Larkin process.

In the second part, I study the gap structure when superconductivity develops from a preexisting antiferromagnetic state. I show that magnetism induces an additional spin-triplet pairing component in addition to the standard singlet pairing. This additional pairing state can coexist with the standard one and leads to superconductivity that breaks time-reversal symmetry. I also consider the case of materials whose gap structure has accidental nodes on the electron pockets. I analyze how two competing types of hybridization effects between the electron pockets shift the nodes in different directions and the consequences for the gap structure.

Contents

List of Tables

List of Figures

Chapter 1

Introduction

1.1 The puzzle of high-temperature superconductivity

The field of high-temperature superconductivity began in 1986 with the experimental observation of superconductivity in the copper-based compound $Ba_xLa_{5-x}Cu_5O_{5(3-y)}$ [2]. The same phenomenon was reported in many similar materials soon after, which constitute a family known as the cuprate superconductors. Two decades later, in 2008, superconductivity was also found in $LaFeAsO_{1-x}F_x$ [3], the first member of the second family, called the iron-based superconductors (FeSCs). These materials have the exciting property that their critical temperature T_c, below which they are superconducting, is significantly larger than that of conventional superconductors. For comparison, superconductivity was first discovered in mercury, which has $T_c = 4.2$ K, while the record T_c for FeSCs approaches 60 K (and possibly 110 K in monolayer systems)[4].

Despite decades of theoretical and experimental effort, there is still debate about how superconductivity emerges in these materials [4]. This is in contrast with the case of conventional superconductors, like mercury, which are successfully described by the Bardeen-Cooper-Schrieffer (BCS) theory [5, 6, 7]. In these materials, the interaction between electrons and phonons (the quanta of lattice vibrations) is attractive in a certain energy range. As a result, there is an effective attraction between electrons which overcomes their electrostatic Coulomb law repulsion and allows them to form bound pairs of total momentum zero. These so-called Cooper pairs then behave like bosonic

particles and condense, leading to superconductivity. However, this theory cannot account for the high T_c of the cuprates and FeSCs, based on the known strength of the electron-phonon interaction in these materials. A successful microscopic theory must therefore identify a mechanism that can lead to the formation of Cooper pairs despite the Coulomb repulsion.

An important hint for identifying this mechanism comes from studying the order parameter of superconductivity, also called the gap function because in BCS theory its magnitude is equal to the energy gap that develops in the quasiparticle dispersion. In general, the gap function Δ is complex-valued and can vary along the Fermi surface and even change between Fermi surfaces in multiband materials. In fact, a gap function that changes sign between Fermi surfaces (i.e., has opposite phase) can solve the problem of binding Cooper pairs when the interaction between electrons is purely repulsive, as long as the interband repulsion is greater than the intraband repulsion [8]. The subject of this dissertation is a particular symmetry of the gap function which realizes this scenario in the FeSCs: The sign-changing s wave, also called s^{+-} symmetry. Before discussing the gap function in more detail, it is convenient to review the general characteristics of the materials in this family.

1.2 General traits of the iron-based superconductors

The FeSCs are layered, crystalline materials whose common feature is planes of iron atoms arranged in a square lattice [9, 10]. Depending on the specific material, either a pnictogen or a chalcogen atom is also located at the center of each square of iron atoms. These pnictogens or chalcogens alternate between being raised above or below the iron plane, in a checkerboard pattern (see Fig. 1.1). The unit cell of this structure contains two iron atoms since there are two inequivalent iron sites. However, it is often convenient to ignore this distinction and work with a one iron (1Fe) unit cell (unfolding the Brillouin zone) instead of the actual two iron (2Fe) unit cell.

The majority of the FeSCs have additional atoms of other elements located between the iron planes described above. The structure of these additional atoms leads to a subdivision of the FeSCs into groups. The first group contains FeSe and FeTe, which are simplest members of the FeSCs. Since they contain exactly two different elements

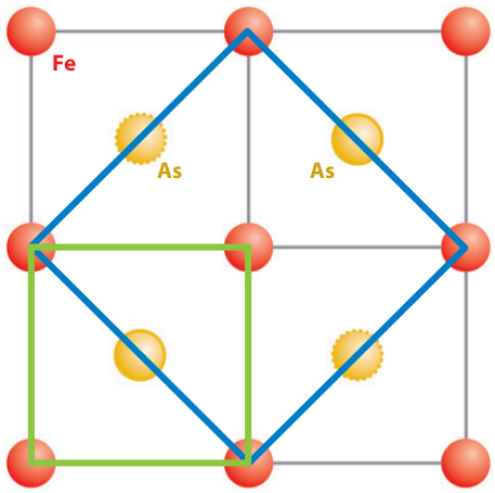

Figure 1.1: Iron plane of FeAs, representing a typical FeSC. The circles labeled As in general represent the position of pnictogen or chalchogen atoms. The smooth circles with this label indicate the atoms above the iron plane, while the circles with sinous edges indicate atoms below the iron plane. Reproduced with permission from Ref. [1]. Copyrighted by the American Physical Society.

in equal proportions, this group is labeled as the 11 materials. The naming of the other groups follows this convention. For example, there are 1111 systems like RFeAsO (where R is a rare-earth element), 122 systems like XFe_2As_2 (where X is an alkaline earth metal), and 111 systems like LiFeAs.

The parent compounds listed above, with few exceptions, are not actually superconducting. Chemical substitution or applied pressure are generally required to make the superconducting state possible. The majority of the systems follow a generic phase diagram (Fig. 1.2), which contains regions of magnetism, superconductivity, and a structural transition of the crystal lattice, in which the arrangement of the iron atoms changes from tetragonal to orthorhombic. This transition occurs at a higher temperature than the magnetic transition and breaks the C_4 point group symmetry while preserving the spin rotational $O(3)$ symmetry. In the magnetic phase, the latter symmetry is also broken, resulting in a spatially inhomogeneous magnetization with the form $M(\mathbf{r}) \propto \cos(\mathbf{Q} \cdot \mathbf{r})$, where the ordering vector $\mathbf{Q}$ in most materials is located on the iron planes and is either $(0, \pi)$ or $(\pi, 0)$, in 1Fe unit cell notation, with the convention of setting the length of the unit cell to 1. Ordering vectors that are incommensurate

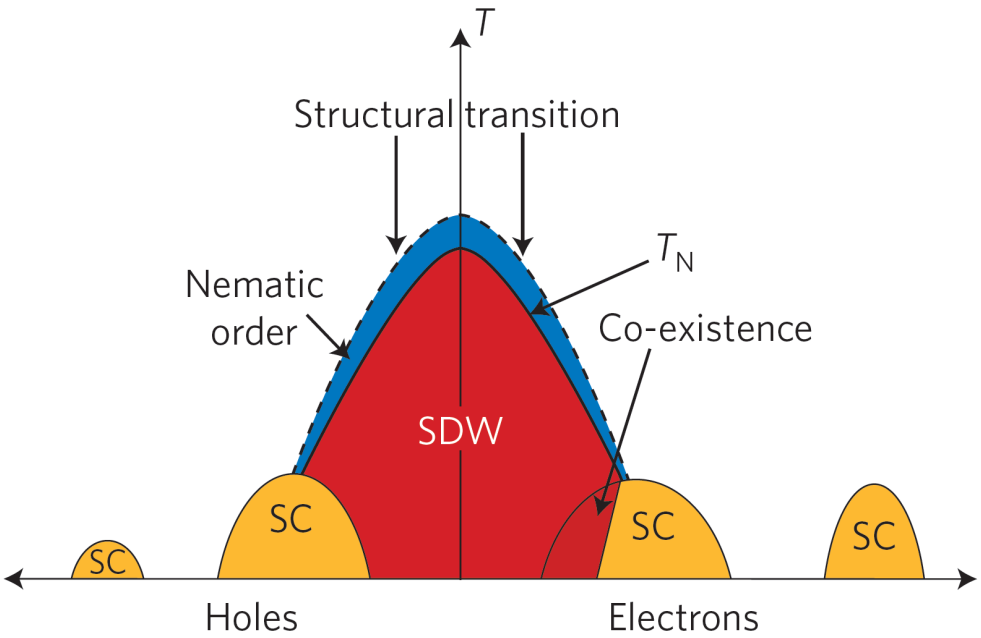

Figure 1.2: Generic phase diagram of iron-based superconductors. The horizontal axis indicates the doping level of holes or electrons. Reproduced with permission from Ref. [1]. Copyrighted by the American Physical Society.

with the iron lattice are also possible. This antiferromagnetic state is known as a spin density wave (SDW) and emerges from itinerant electrons rather than from localized magnetic moments.

In order to understand the unique features of the superconducting state in the FeSCs one needs to first discuss their electronic structure. These materials generally have multiple bands which cross the Fermi surface and originate mainly from the $3d$ orbitals of the iron atoms. In most cases, the dispersion of quasiparticles has little or no dependence on the momentum perpendicular to the iron plane. Because of this, one can describe their band structure from a quasi-two-dimensional perspective. In this picture, the iron d_{xy}, d_{xz}, and d_{yz} orbitals form two concentric hole pockets at the center of the Brillouin zone (the Γ point) and two electron pockets centered at $(\pi, 0)$ and $(0, \pi)$ [the M_x and M_y points, respectively]. In a few materials a third pocket develops depending on the doping level, but for the sake of generality it is convenient to avoid this complication.

1.3 Superconducting state and research summary

The richness of the band structure allows for a plethora of possibilities for the gap function in the superconducting state. As mentioned above, a gap parameter Δ which changes sign between Fermi surfaces provides a solution to the problem of finding a channel of attraction between electrons which normally repel each other. This can be realized with s symmetry if Δ has one sign on the hole pockets and the opposite sign on the electron pockets. This scenario is called s^{+-} symmetry, to distinguish it from a scenario in which all Fermi surfaces have the same sign (s^{++} or conventional s symmetry). In this dissertation I focus on this possibility and begin by presenting two experimental observations that can be explained with the assumption that this is the correct symmetry of the gap function.

The first experimental observation I discuss, which is often quoted as the strongest evidence for s^{+-} gap symmetry[4] is the resonance seen in inelastic neutron scattering experiments. It appears only below T_c and has been seen both in the cuprates and the FeSCs. This resonance is observed as a sharp peak centered at (or near) momentum transfer $(0, \pi)$ and $(\pi, 0)$ in the 1Fe Brillouin zone, which is the same momentum that connects hole and electron Fermi surfaces in the FeSCs. Theoretical work shows that the dynamical magnetic susceptibility of a superconductor with that symmetry develops a pole, which physically corresponds to a spin exciton, a collective mode consisting of a bound state of an electron and a hole with total spin of 1. In Chapter 2, I review this calculation and extend it to include particle-particle excitations, which are often neglected in the literature. This work as been published as Ref. [11], in collaboration with Andrey Chubukov and Peter Wölfle and is copyrighted by the American Physical Society.

The other experimental feature I discuss has been observed in polarization-sensitive Raman spectroscopy of $NaFe_{1-x}Co_xAs$ [12], AFe_2As_2 (where A =Eu,Sr) [13, 14], and $Ba(Fe_{1-x}Co_x)_2As_2$ [15, 16]. Polarized light was used to probe the Raman response in different symmetry channels, classified by the irreducible representations of the D_{4h} crystallographic point group [17, 18]. In the superconducting state, the imaginary part of the Raman susceptibility in the B_{1g} channel displays a strong resonance-type peak

at around 50 cm^{-1}, but there is no such resonance peak in other channels. In addition, in the normal state the real part of the (almost) static and uniform B_{1g} Raman susceptibility is strongly temperature dependent—it increases below 300 K roughly as $1/(T - T_0)$. In Chapter 3, I show that both features can be explained by the coupling of electrons to pairs of magnetic fluctuations. For the resonance there are two possible scenarios: It can be seen as an exciton in which the electron and hole are bound because of the attraction mediated by the fluctuations, or as a different kind of collective mode caused by the attraction between the fluctuations themselves, which is in turn mediated by the electrons. In either case, the form of the magnetic fluctuations depends strongly on s^{+-} symmetry because of the spin exciton mode they contain. Furthermore, the temperature dependence in the normal state is explained by the same process and is the combination of the temperature dependence of two functions: a) The vertex that couples light to magnetic fluctuations and b) the Ising-nematic susceptibility, which serves as the interaction between the fluctuations. This work has been published as Ref. [19] and was done in collaboration with Andrey Chubukov and Jiashen Cai and is copyrighted by the American Physical Society.

Even if s^{+-} is indeed the gap symmetry of most members of the FeSCs, there are special circumstances which can modify it and which need to be considered in order to have a more complete description of the materials. In Chapter 4, I study the case where superconductivity emerges from a preexisting magnetic state. In this region of the phase diagram, superconductivity may develop a component which is a mixture of intrapocket singlet s^{++} pairing and interpocket spin-triplet pairing (named the t state). The coupling constant for the t channel is proportional to the SDW order parameter and involves interactions that do not contribute to superconductivity outside of the SDW region. I argue that the s+- and t-type superconducting orders coexist at low temperatures, and the relative phase between the two is, in general, different from 0 or π, manifesting explicitly the breaking of the time-reversal symmetry promoted by long-range SDW order. I argue that time reversal may get broken even before true superconductivity develops. This work has been published as Ref. [20] in collaboration with Andrey Chubukov and Rafael Fernandes is copyrighted by the American Physical Society.

Another circumstance that can modify s^{+-} superconductivity is hybridization between electron pockets. In Chapter 5, I consider the case of a gap function that has accidental nodes, i.e., nodes whose position is determined by the parameters in the system instead of fixed by symmetry. I argue that hybridization reconstructs the Fermi surfaces and also induces an additional interpocket pairing component. I analyze how these two effects modify the gap structure by tracing the position of the nodal points of the energy dispersions in the superconducting state. I find three possible outcomes. In the first, the nodes simply shift their positions in the Brillouin zone; in the second, the nodes merge and disappear, in which case the gap function has either equal or opposite signs on the electron pockets; in the third, a new set of nodal points emerges, doubling the original number of nodes. This work was published as Ref. [21] in collaboration with Andrey Chubukov and is copyrighted by the American Physical Society.

1.4 Outline of the dissertation

The structure of the dissertation is the following:

- Chapter 2 analyzes the resonance in inelastic neutron scattering within the framework of s^{+-} gap symmetry. The results presented in this chapter have been published in Ref. [11]. Copyrighted by the American Physical Society (APS).
- Chapter 3 presents an explanation for the experimental features seen in Raman spectroscopy which concern both the normal and superconducting state of FeSCs. The features in the superconducting state are again dependent on s^{+-} symmetry. These results were published Ref. [19]. Copyright by APS.
- Chapter 4 presents an extension of s^{+-} symmetry which emerges when superconductivity develops from a preexisting magnetic state. In this case, a state in which superconductivity breaks time-reversal symmetry is possible. Published in Ref. [20]. Copyright by APS.
- Chapter 5 presents another extension of s^{+-} symmetry, which emerges due to hybridization of the electron pockets. Published in Ref. [21]. Copyright by APS.
- Chapter 6 contains the conclusions.

Chapter 2

Effect of pairing fluctuations on the spin resonance

2.1 Introduction

The spin resonance, observed by inelastic neutron scattering (INS) experiments first in the cuprates[22, 23, 24, 25, 26, 27, 28] and then in heavy-fermion [29, 30] and Fe-based superconductors (FeSCs)[31, 32, 33, 34, 35, 36, 37, 38], has been the subject of intense theoretical and experimental studies over the past decade using both metallic [39, 40, 41, 42, 43, 44, 45, 46, 47, 48, 49, 50, 51, 52, 53, 54] and near-localized strong-coupling scenarios [55] (see Ref. [56] for a review). The theoretical interpretations of the resonance can be broadly split into two classes. The first class of theories assumes that the spin resonance is a magnon, overdamped in the normal state due to the strong decay into low-energy particle-hole pairs, but emerging prominently in the superconducting state due to reduction of scattering at low energies [54, 57]. In this line of reasoning the resonance energy Ω_{res} is the magnon energy and as such it is uncorrelated with the superconducting gap Δ. However, the decay of magnons into particle-hole pairs is only suppressed at energies below 2Δ, hence the magnons become sharp in a superconductor only if their energy is below 2Δ. The symmetry of the superconducting state does not play a crucial role here. It is only relevant that the superconducting gap is finite at the Fermi surface (FS) points connected by the gap momentum $\mathbf{Q}$.

Theories from the second class assume that the resonance does not exist in the

normal state and emerges in the superconducting state as a feedback effect from superconductivity, like e.g., the Anderson-Bogolyubov mode in the case of a charge neutral single condensate component, a Leggett mode in the case of several gap components, a wave-like excitation of a spin-triplet order parameter, or a pair vibration mode in the case of a gap parameter possessing internal structure [58]. These "feedback" theories can be further split into three sub-classes. In the first the resonance is viewed as a spin-exciton, i.e., the pole in the dynamical spin susceptibility $\chi(\mathbf{q}, \Omega)$ dressed by multiple particle-hole bubbles [59, 52, 53]. Such $\chi(\mathbf{q}, \Omega)$ can be obtained by using a computational scheme based on the random-phase approximation (RPA). It was argued that, if the superconducting gap changes sign between FS points connected by $\mathbf{Q}$, the residual attraction pulls the resonance frequency to $\Omega_{res} < 2\Delta$, where the decay into particle-hole pairs is reduced below T_c and vanishes at $T = 0$. As a result, at $T = 0$, $\chi^{''}(\mathbf{q}, \Omega)$ has a $\delta-$functional peak at Ω_{res}. In this respect, if the resonance is an exciton, its existence necessary implies that the superconducting gap changes sign either between patches of the FS connected by $\mathbf{Q}$ or between different Fermi pockets again connected by $\mathbf{Q}$. The role of the resonance in allowing to determine the structure of the gap in a number of different superconductors has been highlighted in [60]. Theories of the second subclass explore the fact that in a superconductor the particle-hole and particle-particle channels are mixed and argue that the strongest resonance is in the particle-particle channel and the measurements of the spin susceptibility just reflect the "leakage" of this resonance into the particle-hole channel. The corresponding resonance has been labeled as the π-exciton [61, 62], where the π boson is a particle-particle excitation with total momentum $\mathbf{Q}$ (a "pair density-wave" in modern nomenclature [63, 64, 65]). Finally, theories of the third class explore the possibility that the resonance emerges due to coupling between fluctuations in particle-hole and particle-particle channel. Within RPA, such resonance is due to non-diagonal terms in the generalized RPA which includes both particle-hole and particle-particle bubbles. It was called a plasmon [66, 67] to stress the analogy with collective excitations in an electronic liquid.

The interplay between the "damped spin-wave", spin-exciton, π-resonance, and plasmon scenarios for 2D high-T_c cuprates has been studied in detail in the past decade. The outcome is that near and above optimal doping the resonance is best described as a spin-exciton, with relatively weak corrections from coupling to the particle-particle

channel[52, 68, 69], while in the underdoped regime, where superconductivity emerges from a pre-existing pseudogap phase, both spin-exciton and spin-wave scenarios have been argued to account for the neutron resonance [56]. The situation is more complicated in 3D heavy-fermion systems [57, 70] because there the excitonic resonance has a finite width even at $T = 0$ if the locus of FS points separated by $\mathbf{Q}$ intersects a line of gap nodes.

In this chapter, we discuss the interplay between spin-exciton, $\pi-$resonance, and plasmon scenarios in FeSCs. Previous studies of the resonance in FeSCs [53] focused only on the response in the particle-hole (spin-exciton) channel and neglected the coupling between particle-hole and particle-particle channels. Our goal is to analyze the effect of such coupling.

As we said, the resonance peak has been observed below T_c in several families of FeSCs[31, 32, 33, 34, 35, 36, 37, 38]. The spin response above T_c in FeSCs is rather featureless away from small doping, which implies that the magnetic excitations in the normal state are highly overdamped and don't behave as damped spin waves. The full analysis of the spin resonance in FeSCs is rather involved as these systems are multi-band materials with four or five FSs, on which the superconducting gap has different amplitudes and phases. Still, the basic conditions for spin-excitonic resonance are the same as in the cuprates and heavy fermion materials: namely, the resonance emerges at momentum $\mathbf{Q}$ if the superconducting gap changes sign between FS points connected by $\mathbf{Q}$. This condition holds if the superconducting gap has s^{+-} symmetry, as most researchers believe, and changes sign between at least some hole and electron pockets. An alternative scenario [71], which we will not discuss in this dissertation is that the superconducting state has a conventional, sign-preserving s^{++} symmetry, and the observed neutron peak is not a resonance but rather a hump at frequencies slightly above 2Δ.

In FeSCs that contain both hole and electron pockets, the resonance has been observed at momenta around $\mathbf{Q} = (\pi, \pi)$, which is roughly the distance between hole and electron pockets in the actual (folded) Brillouin zone. To account for the resonance and, at the same time, avoid unnecessary complications, we consider a minimal three-band model (one hole pocket and two electron pockets), and neglect the angular dependence of the interactions along the FSs. Including this dependence and additional hole pockets

will complicate the analysis but we don't expect it to lead to any qualitative changes to our results.

We find that for repulsive density-density and pair-hopping interactions, the resonance peak is, to a good accuracy, a spin-exciton. The $\pi-$resonance does not develop on its own, and the coupling between the resonant spin-exciton channel and the non-resonant $\pi-$channel only slightly shifts the energy of the excitonic resonance. We also considered the case (less justified microscopically) when the interaction in the π channel is attractive, such that both spin-exciton and π resonance develop on their own at frequencies below 2Δ. One could expect in this situation that the full dynamical spin susceptibility has two peaks. We found, however, that this happens only if we make the coupling between particle-hole and particle-particle channels artificially small. When we restored the original coupling, we found, in general, only one peak below 2Δ. The peak is a mixture of a spin-exciton and π-resonance and at least in some range of system parameters its energy is smaller than that of a spin-exciton and a π-resonance. This implies that, when both channels are attractive, the coupling between the two plays a substantial role in determining the position of the true resonance which can, at least partly, be viewed as a plasmon. A somewhat similar result has been obtained earlier for the cuprates [52, 69, 66, 67]. For some system parameters we did find two peaks in $\mathrm{Im}\chi_S(\mathbf{Q},\omega)$, but for one of them $\mathrm{Im}\chi_S$ has the wrong sign. We verified that this indicates that for such parameters the system is unstable either against condensation of π excitations (i.e., against superconductivity at momentum $\mathbf{Q}$), or against the development of SDW order in co-existence with superconductivity.

The chapter is organized as follows: In the next section we consider the model. In Sec. 2.3 we obtain the dynamical spin susceptibility within the generalized RPA scheme, which includes the coupling between particle-hole and particle-particle channels. In Sec. 2.4 we analyze the profile of $\chi_S(\mathbf{Q},\omega)$ first for purely repulsive density-density and pair-hopping interactions, and then for the case when we allow the density-density interaction to become attractive. We summarize our conclusions in Sec. 2.5.

2.2 The model

The FeSCs are multiband metals with two or three hole FS pockets centered around the Γ point $(0,0)$ and two elliptical electron pockets centered at (π,π) in the folded BZ with two iron atoms per unit cell. The electron pockets are elliptical and related by symmetry, while the hole pockets are C_4-symmetric, but generally differ in size. Since we are only interested in studying the role of the particle-particle channel in the spin response function, for which the non-equivalence between hole pockets is not essential, we consider the case of two hole pockets and assume that they are circular and identical, and also neglect the ellipticity of electron pockets. Under these assumptions our model reduces effectively to only one hole pocket (c fermions) and one electron pocket (f fermions). The fact that there are actually two hole and two electron pockets only adds up combinatoric factors.

The free part of the Hamiltonian is

$$H_0 = \sum_{\mathbf{k},\sigma} \left(\xi^c_{\mathbf{k}} c^\dagger_{\mathbf{k}\sigma} c_{\mathbf{k}\sigma} + \xi^f_{\mathbf{k}+\mathbf{Q}} f^\dagger_{\mathbf{k}+\mathbf{Q}\sigma} f_{\mathbf{k}+\mathbf{Q}\sigma} \right), \tag{2.1}$$

where

$$\xi^c_{\mathbf{k}} = \mu_c - \frac{k_x^2 + k_y^2}{2m_c}, \tag{2.2}$$

$$\xi^f_{\mathbf{k}+\mathbf{Q}} = -\mu_f + \frac{k_x^2 + k_y^2}{2m_f} \tag{2.3}$$

We do not study here how superconductivity develops from interactions, as that work has been done elsewhere [72]. Instead, we simply assume that the system reaches a superconducting state with s^{+-} symmetry before it becomes unstable towards magnetism and take the superconducting gaps as inputs. In this state, the free part of the Hamiltonian is

$$H_0^{SC} = \sum_{\mathbf{k},\sigma} \left(E^c_{\mathbf{k}} c^\dagger_{\mathbf{k}\sigma} c_{\mathbf{k}\sigma} + E^f_{\mathbf{k}+\mathbf{Q}} f^\dagger_{\mathbf{k}+\mathbf{Q}\sigma} f_{\mathbf{k}+\mathbf{Q}\sigma} \right), \tag{2.4}$$

where the dispersions are $E^c_{\mathbf{k}} = \sqrt{(\xi^c_{\mathbf{k}})^2 + (\Delta^c)^2}$ and $E^f_{\mathbf{k}+\mathbf{Q}} = \sqrt{(\xi^f_{\mathbf{k}+\mathbf{Q}})^2 + (\Delta^f)^2}$, and $\Delta^c = -\Delta^f \equiv \Delta$.

Now we consider interactions that contribute to the spin susceptibility. They consist of a density-density interband interaction u_1 and a correlated interband hopping u_3. Intraband repulsion only affects the chemical potentials but does not otherwise contribute

to the spin susceptibility. Interband exchange in principle contributes in the π channel but in renormalization group analysis it flows to small values[73]. In general, u_1 and u_3 depend on the angle in momentum space via coherence factors associated with the transformation from the orbital to the band basis [74, 75]. However, this complication is not essential for our purposes and we take both interactions to be momentum independent. The interaction Hamiltonian is

$$\begin{aligned} H_{\text{int}} = u_1 & \sum_{[1234],\sigma\neq\sigma'} c^\dagger_{\mathbf{p}_1\sigma} f^\dagger_{\mathbf{p}_2\sigma'} f_{\mathbf{p}_3\sigma'} c_{\mathbf{p}_4\sigma} \\ + u_3 & \sum_{[1234],\sigma\neq\sigma'} \left(c^\dagger_{\mathbf{p}_1\sigma} c^\dagger_{\mathbf{p}_2\sigma'} f_{\mathbf{p}_3\sigma'} f_{\mathbf{p}_4\sigma} + \text{h.c.} \right), \end{aligned} \tag{2.5}$$

where the sum over momenta obeys momentum conservation as usual ($\mathbf{p}_1 + \mathbf{p}_2 = \mathbf{p}_3 + \mathbf{p}_4$).

Because the interactions in the band basis are linear combinations of Hubbard and Hund interactions in the orbital basis, weighted with orbital coherence factors, the sign of u_1 and u_3 depends on the interplay between intra-orbital and inter-orbital interactions [71, 76, 77]. The interaction u_3 contributes to the superconducting channel, and for an s^{+-} gap structure must be repulsive. The sign of u_1 is a priori unknown. In most microscopic studies it comes out positive (repulsive), but in principle it can also be negative (attractive). We do not assume a particular sign of u_1 and consider first a case where u_1 is positive and then when it is negative. For the first case we show that a resonance can only originate from the particle-hole channel. For negative u_1 the π channel can produce collective modes as well, and we show that in general the resonant mode is a mix between spin exciton and a π-resonance.

2.3 Susceptibilities and RPA

We focus on susceptibilities at antiferromagnetic momentum $\mathbf{Q}$ which separates the centers of hole and electron pockets. Following similar work done on the cuprates[52],

we define spin and π operators as

$$S^z(\mathbf{Q}) = \frac{1}{\sqrt{N}} \sum_{\mathbf{k}} \left[c^\dagger_{\mathbf{k}\alpha} \sigma^z_{\alpha\beta} f_{\mathbf{k}+\mathbf{Q}\beta} + f^\dagger_{\mathbf{k}+\mathbf{Q}\alpha} \sigma^z_{\alpha\beta} c_{\mathbf{k}\beta} \right], \tag{2.6}$$

$$\pi(\mathbf{Q}) = \frac{1}{\sqrt{N}} \sum_{\mathbf{k}} \left[c_{\mathbf{k}\alpha} \sigma^x_{\alpha\beta} f_{\mathbf{Q}-\mathbf{k}\beta} \right]. \tag{2.7}$$

To make a closer connection to [52], the operator π can be equivalently defined as $\pi = \frac{1}{\sqrt{N}} \sum_{\mathbf{k}} \left[g_{\mathbf{k}} a_{\mathbf{k}\alpha} \sigma^x_{\alpha\beta} a_{\mathbf{Q}-\mathbf{k}\beta} \right]$, with $|g_{\mathbf{k}}| = 1/2$ and the sign of $g_{\mathbf{k}}$ is chosen so that it is positive near the hole FS and negative near the electron FS ($g_{\mathbf{k}} = -g_{\mathbf{Q}-\mathbf{k}}$).

For notational convenience we split S^z into two operators such that $S^z = S_c + S_f$, where

$$S_c(\mathbf{Q}) = \frac{1}{\sqrt{N}} \sum_{\mathbf{k}} c^\dagger_{\mathbf{k}\alpha} \sigma^z_{\alpha\beta} f_{\mathbf{k}+\mathbf{Q}\beta}, \tag{2.8}$$

$$S_f(\mathbf{Q}) = \frac{1}{\sqrt{N}} \sum_{\mathbf{k}} f^\dagger_{\mathbf{k}+\mathbf{Q}\alpha} \sigma^z_{\alpha\beta} c_{\mathbf{k}\beta}. \tag{2.9}$$

We now define the susceptibilities $\chi_{ab}(\Omega_m)$ in terms of Matsubara frequencies as

$$\chi_{ab}(\Omega_m) = \int_0^{1/T} \mathrm{d}\tau' e^{i\Omega_m \tau'} \left\langle T_\tau A_a(\tau') A^\dagger_b(0) \right\rangle, \tag{2.10}$$

where $A_a = (S_c, S_f, \pi, \pi^\dagger)_a$. The actual spin susceptibility is given by $\chi_S = \chi_{11} + \chi_{12} + \chi_{21} + \chi_{22}$.

The bare susceptibilities χ^0_{ab} can be calculated in the usual way in terms of Green's functions and are given by bubbles made out of c and f-fermions, with different Pauli matrices in the vertices. At $T = 0$ and after performing analytic continuation to real frequency space, the (retarded) susceptibilities have the following form:

$$\chi^0_{ab}(\omega) = \frac{2}{N} \sum_{\mathbf{k}} \left[-\frac{A_{ab}(\mathbf{k})}{\omega - E^c_{\mathbf{k}} - E^f_{\mathbf{k}+\mathbf{Q}} + i\gamma} + \frac{B_{ab}(\mathbf{k})}{\omega + E^c_{\mathbf{k}} + E^f_{\mathbf{k}+\mathbf{Q}} + i\gamma} \right], \tag{2.11}$$

where χ^0_{ab}, A_{ab}, and B_{ab} are symmetric matrices. The expressions for A_{ab} and B_{ab} are presented in Table 2.1 in terms of coherence factors which are given by:

$$u^c_{\mathbf{k}} = \sqrt{\frac{1}{2}\left(1 + \frac{\xi^c_{\mathbf{k}}}{E^c_{\mathbf{k}}}\right)}, \tag{2.12}$$

$$v^c_{\mathbf{k}} = \sqrt{\frac{1}{2}\left(1 - \frac{\xi^c_{\mathbf{k}}}{E^c_{\mathbf{k}}}\right)} \operatorname{sgn} \Delta^c, \tag{2.13}$$

a	b	$A_{ab}(\mathbf{k})$	$B_{ab}(\mathbf{k})$
1	1	$(v^c_{\mathbf{k}} u^f_{\mathbf{k}'})^2$	$(u^c_{\mathbf{k}} v^f_{\mathbf{k}'})^2$
1	2	$-u^c_{\mathbf{k}} v^c_{\mathbf{k}} u^f_{\mathbf{k}'} v^f_{\mathbf{k}'}$	$-u^c_{\mathbf{k}} v^c_{\mathbf{k}} u^f_{\mathbf{k}'} v^f_{\mathbf{k}'}$
1	3	$u^c_{\mathbf{k}} v^c_{\mathbf{k}} (u^f_{\mathbf{k}'})^2$	$-u^c_{\mathbf{k}} v^c_{\mathbf{k}} (v^f_{\mathbf{k}'})^2$
1	4	$(v^c_{\mathbf{k}})^2 u^f_{\mathbf{k}'} v^f_{\mathbf{k}'}$	$-(u^c_{\mathbf{k}})^2 u^f_{\mathbf{k}'} v^f_{\mathbf{k}'}$
2	2	$(u^c_{\mathbf{k}} v^f_{\mathbf{k}'})^2$	$(v^c_{\mathbf{k}} u^f_{\mathbf{k}'})^2$
2	3	$-(u^c_{\mathbf{k}})^2 u^f_{\mathbf{k}'} v^f_{\mathbf{k}'}$	$(v^c_{\mathbf{k}})^2 u^f_{\mathbf{k}'} v^f_{\mathbf{k}'}$
2	4	$-u^c_{\mathbf{k}} v^c_{\mathbf{k}} (v^f_{\mathbf{k}'})^2$	$u^c_{\mathbf{k}} v^c_{\mathbf{k}} (u^f_{\mathbf{k}'})^2$
3	3	$(u^c_{\mathbf{k}} u^f_{\mathbf{k}'})^2$	$(v^c_{\mathbf{k}} v^f_{\mathbf{k}'})^2$
3	4	$u^c_{\mathbf{k}} v^c_{\mathbf{k}} u^f_{\mathbf{k}'} v^f_{\mathbf{k}'}$	$u^c_{\mathbf{k}} v^c_{\mathbf{k}} u^f_{\mathbf{k}'} v^f_{\mathbf{k}'}$
4	4	$(v^c_{\mathbf{k}} v^f_{\mathbf{k}'})^2$	$(u^c_{\mathbf{k}} u^f_{\mathbf{k}'})^2$

Table 2.1: Coefficients of bare susceptibilities. Note: $\mathbf{k}' = \mathbf{k} + \mathbf{Q}$.

and similar expressions for $u^f_{\mathbf{k}'}$ and $v^f_{\mathbf{k}'}$.

To obtain the full susceptibilities χ_{ab} we used the generalized RPA approach. Within this approach

$$\chi_{ab} = (1 - \chi^0 V)^{-1}_{ac} \chi^0_{cb}, \tag{2.14}$$

where the sum over repeated indices is implied and V is given by

$$V = \frac{1}{2} \begin{pmatrix} u_1 & u_3 & 0 & 0 \\ u_3 & u_1 & 0 & 0 \\ 0 & 0 & -u_1 & 0 \\ 0 & 0 & 0 & -u_1 \end{pmatrix}. \tag{2.15}$$

The solution for the full spin susceptibility can be written in a simpler form once we note that the matrix χ^0_{ab} has additional symmetry. Indeed, the functions $A_{ab}(\mathbf{k})$ and $B_{ab}(\mathbf{k})$ can be separated into parts that are even or odd with respect to $\xi^c_{\mathbf{k}}$ and $\xi^f_{\mathbf{k}}$. If the momentum sums are evaluated only near the FSs, where the integration region can be chosen to be symmetric with respect to positive and negative values of $\xi^c_{\mathbf{k}}$ and $\xi^f_{\mathbf{k}}$, then the odd parts cancel out and χ^0_{ab} acquires the following form:

$$\chi^0 = \begin{pmatrix} a & b & c & -d \\ b & a & d & -c \\ c & d & e & f \\ -d & -c & f & e \end{pmatrix} \tag{2.16}$$

If we rotate the basis of operators from $(S_c, S_f, \pi, \pi^\dagger)$ to $(S_c + S_f, \pi - \pi^\dagger, S_c - S_f, \pi + \pi^\dagger)$ we find that both V and χ^0 become block diagonal, so the first 2×2 system decouples from the second one. In this case, the solution for the subset $(S_c + S_f, \pi - \pi^\dagger)$ takes the simple form

$$\chi_S = \frac{\chi_S^0 + \delta\chi_S^0}{1 - u_S(\chi_S^0 + \delta\chi_S^0)}, \tag{2.17}$$

$$\chi_\pi = \frac{\chi_\pi^0 + \delta\chi_\pi^0}{1 - u_\pi(\chi_\pi^0 + \delta\chi_\pi^0)}, \tag{2.18}$$

where

$$\delta\chi_S^0 = \frac{u_\pi}{1 - u_\pi\chi_\pi^0}\left(\chi_{S\pi}^0\right)^2, \tag{2.19}$$

$$\delta\chi_\pi^0 = \frac{u_S}{1 - u_S\chi_S^0}\left(\chi_{S\pi}^0\right)^2. \tag{2.20}$$

and $u_S = (u_1 + u_3)/4$ and $u_\pi = -u_1/4$. The bare susceptibilities in this basis are given by

$$\chi_S^0 = \chi_{11}^0 + \chi_{12}^0 + \chi_{21}^0 + \chi_{22}^0 = 2(\chi_{11}^0 + \chi_{12}^0), \tag{2.21}$$

$$\chi_\pi^0 = \chi_{33}^0 - \chi_{34}^0 - \chi_{43}^0 + \chi_{44}^0 = 2(\chi_{33}^0 - \chi_{34}^0), \tag{2.22}$$

$$\chi_{S\pi}^0 = \chi_{13}^0 - \chi_{14}^0 + \chi_{23}^0 - \chi_{24}^0 = 2(\chi_{13}^0 - \chi_{14}^0). \tag{2.23}$$

The first two bare susceptibilities contain contributions of products of two normal Green's functions and of two anomalous Green's functions, while $\chi_{S\pi}^0$ is composed of one normal and one anomalous Green's function (see Fig. 2.1 for some contributions of $\chi_{S\pi}^0$ to the spin response function).

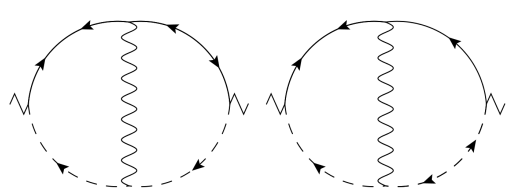

Figure 2.1: Some mixed-channel contributions to the spin susceptibility and Raman scattering. The solid lines represent f fermions and the dashed lines c fermions, corresponding to quasiparticles from the electron and hole pockets, respectively.

We obtained expressions for the real parts of the bare susceptibilities by replacing the momentum sums by integrals and evaluating them within an energy range from $-\Lambda$ to Λ about the FSs. They are valid in the range $0 < \omega < 2\Delta$ in the limit when the broadening $\gamma \to 0$.

$$\mathrm{Re}\chi_S^0(\omega) = L + \frac{\omega^2}{4\Delta^2}\mathrm{Re}\chi_\pi^0(\omega), \tag{2.24}$$

$$\mathrm{Re}\chi_\pi^0(\omega) = \frac{m}{\pi}\frac{4\Delta^2}{\omega\sqrt{4\Delta^2-\omega^2}}\arctan\left(\frac{\omega}{\sqrt{4\Delta^2-\omega^2}}\right), \tag{2.25}$$

$$\mathrm{Re}\chi_{S\pi}^0(\omega) = \frac{\omega}{2\Delta}\mathrm{Re}\chi_\pi^0(\omega), \tag{2.26}$$

where $L = \frac{m}{\pi}\log(2\Lambda/\Delta)$ and we have neglected terms of order $(\Delta/\Lambda)^2$.

In Fig. 2.2 we present the results of numerical calculations of the bare susceptibilities in the case of perfectly nested FSs ($\mu_c = \mu_f \equiv \mu$). The susceptibility χ_S^0 would diverge at $\omega = 0$ in the absence of superconductivity, but becomes finite at a finite Δ. Conversely, χ_π^0 at $\omega = 0$ would be zero in the absence of superconductivity, but becomes non-zero because of Δ. Note that all three susceptibilities monotonically increase with frequency in the domain $0 \leq \omega \leq 2\Delta$ and diverge at $\omega = 2\Delta$. The imaginary parts of the three bare susceptibilities (not shown in the plot) are infinitesimally small and undergo a discontinuous jump at $\omega = 2\Delta$. If we make the electron pocket elliptical, the divergence in the real part is replaced by a local maximum.

We see that $\chi_S^0(\omega)$ and $\chi_\pi^0(\omega)$ have finite value at $\omega = 0$. We recall that, in the absence of superconductivity, $\chi_S(0)$ would diverge and $\chi_\pi(0)$ would vanish at perfect nesting. At $\omega = 2\Delta$ both bare susceptibilities diverge. The cross-susceptibility $\chi_{S\pi}^0(\omega)$ vanishes at $\omega = 0$ simply because it is composed from one normal and one anomalous Green's function but rapidly increases with ω and becomes comparable to $\chi_S(\omega)$ and $\chi_\pi(\omega)$ at $\omega \leq 2\Delta$.

The cross-susceptibility between particle-hole and particle-particle channels has been recently analyzed for an s^{+-} superconductor in the context of Raman scattering [78]. There, it was computed in the charge channel and was found to be very small due to near-cancellation between contributions from Fermi surfaces with plus and minus values of the superconducting gap. In our case we found that the contributions from hole and electron FSs add up rather than cancel. The difference is that in Raman scattering the side vertices in the susceptibility bubble have the spin structure given by $\delta_{\alpha,\beta}$, while

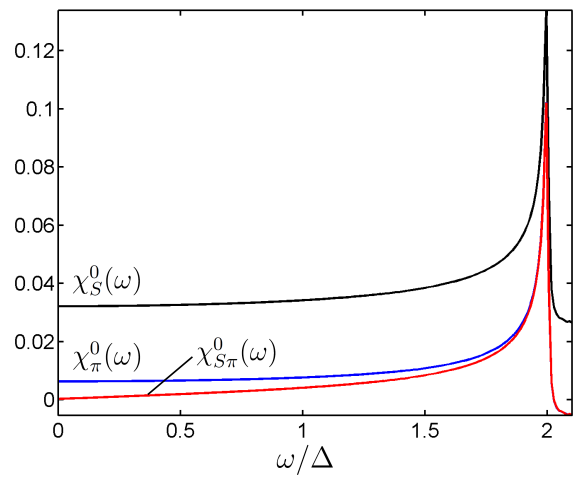

Figure 2.2: Real part of the bare spin susceptibilities ($T = 0$, units of Δ^{-1}) in the case of perfectly nested circular pockets ($m \equiv m_c = m_f = \frac{1}{100\Delta}$). In all numerical calculations $\mu = 10\Delta$ and we include a finite broadening $\gamma = \Delta/200$ when evaluating momentum integrals.

in our case the spin structure is, say, $\sigma^z_{\alpha,\beta}$. For an s^{+-} gap, Raman bubbles from hole and electron pocket have the same vertex structure but differ in the sign of the anomalous Green's function, hence the two contributions to cross-susceptibility have opposite signs, resulting in a cancellation that is complete in the case of perfect nesting and near-complete in the case of one circular and one elliptical pocket. This cancellation does not occur in our case because the σ^z structure of the side vertices additionally flips the sign of one of the two diagrams, and the contributions to $\chi^0_{S\pi}(\omega)$ from hole and electron FSs add constructively.

We next note that the terms $\delta\chi^0_S$ and $\delta\chi^0_\pi$ are precisely what is neglected when the particle-particle channel is not included in the calculation of the spin susceptibility. Setting these terms to zero reduces the expressions for the full χ_S and χ_π to the usual RPA results

$$\chi_S = \frac{\chi^0_S}{1 - u_S\chi^0_S}, \qquad \chi_\pi = \frac{\chi^0_\pi}{1 - u_\pi\chi^0_\pi}. \tag{2.27}$$

The effect of coupling the two channels can be seen more clearly by substituting (2.19)

into (2.17), which yields

$$\begin{aligned}\chi_S =& \frac{\chi_S^0(1-u_\pi\chi_\pi^0)+u_\pi(\chi_{S\pi}^0)^2}{(1-u_S\chi_S^0)(1-u_\pi\chi_\pi^0)-u_S u_\pi(\chi_{S\pi}^0)^2} \\ =& \frac{1}{u_S}\left[-1+\frac{1-u_\pi\chi_\pi^0}{(1-u_S\chi_S^0)(1-u_\pi\chi_\pi^0)-u_S u_\pi(\chi_{S\pi}^0)^2}\right]\end{aligned} \tag{2.28}$$

The positions of resonance peaks are given by the zeroes of the denominator in this equation and we can see that the particle-hole and particle-particle channels are coupled through the mixed-channel susceptibility $\chi_{S\pi}^0(\omega)$.

2.4 Results

2.4.1 Purely repulsive interaction: $u_1 > 0$, $u_3 > 0$.

For repulsive interactions $u_S > |u_\pi| > 0$ and $u_\pi < 0$. In the absence of $\chi_{S\pi}^0$ the resonance in χ_S is present for any u_S because the bare susceptibility χ_S^0 is positive and diverges at $\omega = 2\Delta$, hence the equation $1 - u_S \mathrm{Re}\chi_S^0(\omega) = 0$ has a solution for $0 < u_S < (\mathrm{Re}\chi_S^0(0))^{-1}$. In contrast, the fact that $\mathrm{Re}\chi_\pi^0 > 0$ means that no resonance originates from this channel. When $\chi_{S\pi}^0$ is included, we found in our numerical calculations that the effect of the particle-particle channel is that the peak in the imaginary part of the full susceptibility is shifted to a higher frequency (since $\mathrm{Re}\{u_S u_\pi(\chi_{S\pi}^0)^2\} < 0$). We show representative behavior of real and imaginary parts of the full spin susceptibility in Fig. 2.3

This result is also obtained when we consider an elliptical electron pocket, except that there is a minimum value for u_S below which no resonance is observed. This is due to the fact that the bare susceptibilities have a local maximum instead of a divergence at $\omega = 2\Delta$.

2.4.2 Partially attractive interaction: $u_1 < 0, u_3 > 0$.

We now consider an alternative case where the density-density interaction $u_1 < 0$, hence $u_\pi = -u_1/4 > 0$. We still assume $u_3 > |u_1|$ such that $u_S > 0$. For positive u_π, the π channel can acquire a resonance on its own since the equation $1 - u_\pi \mathrm{Re}\chi_\pi^0(\omega) = 0$ necessarily has a solution at a frequency between 0 and 2Δ if $u_\pi < (\mathrm{Re}\chi_\pi^0(0))^{-1}$. We assume

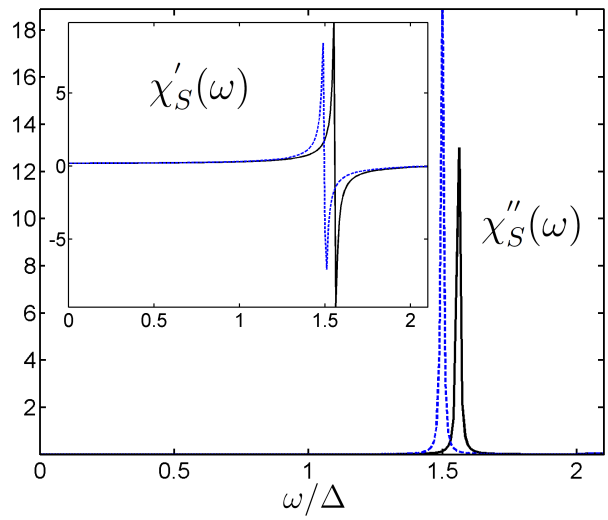

Figure 2.3: Imaginary part (main plot) and real part (insert) of the full spin susceptibility ($T = 0$, units of Δ^{-1}) in the case of repulsive interactions. In this plot $u_S = 26\Delta$ and $u_\pi = -13\Delta$. The solid, black line indicates the full calculation. For comparison, the dashed, blue line indicates a calculation that neglects particle-particle contributions.

that this inequality holds together with $u_S < (\mathrm{Re}\chi_S^0(0))^{-1}$. If any of these two conditions are not satisfied, the system becomes unstable either towards π superconductivity with total momentum of a Cooper pair $\mathbf{Q}$ or towards magnetic order. In both cases, the analysis of the spin susceptibility has to be modified to include the new condensates. If the spin-exciton and π channels were not coupled (i.e., if $\chi_{S\pi}^0(\omega)$ was absent), we would find resonances in the spin and π channels at frequencies ω_S and ω_π, respectively, set by $1 - u_S\mathrm{Re}\chi_S^0(\omega_S) = 0$ and $1 - u_\pi\mathrm{Re}\chi_\pi^0(\omega_\pi) = 0$. This suggests the possibility that there may be two resonance peaks in the full spin susceptibility $\chi_S(Q, \omega)$ once we restore the coupling $\chi_{S\pi}^0(\omega)$.

However, we found that for all values of u_S and u_π for which the pure s^{+-} state is stable, there is only a single peak in the spin susceptibility at a frequency lower than both ω_S and ω_π. We show representative behavior in Fig. 2.4. The existence of a single peak is due to the fact that $\chi_{S\pi}^0$ is small at small frequencies, hence it does not prevent the increase of the real part of the spin susceptibility with increasing ω (see insert in Fig. 2.4) and only shifts the position of the lower pole (ω_S or ω_π) to a smaller value ω_{res}. At the same time, at higher frequencies, $\chi_{S\pi}^0$ is no longer small relative to the other bare

susceptibilities χ_S^0 and χ_π^0. As a result, the denominator in $\chi_S(\mathbf{Q},\omega)$ in (2.28) passes through zero at $\omega = \omega_{res}$ and then remains negative all the way up to $\omega = 2\Delta$ and does not cross zero for the second time.

To better understand this, we artificially add a factor ϵ to $\chi_{S\pi}^0$ and consider how the solutions evolve as we progressively increase ϵ between 0 and 1. At small ϵ, the two solutions obviously survive and just further split from each other – the peak that was at a higher frequency shifts to a higher frequency and the other peak shifts to to a lower frequency. As ϵ increases, the peak at a higher frequency rapidly moves towards 2Δ. If we keep $\mathrm{Im}\chi_{ab}^0$ strictly zero, this peak survives up to $\epsilon = 1$ with exponentially vanishing amplitude. If, however, we keep a small but finite fermionic damping in the computations of χ_{ab}^0, we find that the functions $\chi_{ab}^0(\omega)$ increase but do not diverge at 2Δ. In this situation, the higher frequency peak in $\chi_S(\mathbf{Q},\omega)$ vanishes already at some $\epsilon < 1$.

We also considered the evolution of the two-peak solution with ϵ in a different way: we postulated that the two peaks should be at $\omega_{res,1}$ and $\omega_{res,2}$, both below 2Δ and solved the set of equations for u_S and u_π which would correspond to such a solution. At small ϵ we indeed found some real u_S and u_π which satisfy "boundary conditions" $u_S\chi_S^0 < 1$ and $u_\pi\chi_\pi^0 < 1$. However this holds only up to some ϵ_{cr}. At higher ϵ the solutions for u_s and u_π become complex, which implies that the two-peak solution is no longer possible. At even higher ϵ real solutions for u_s and u_π reappear, but they do not satisfy the boundary conditions. We searched for a range of $\omega_{res,1}$ and $\omega_{res,2}$ and for all values that we tested we found $\epsilon_{cr} < 1$, i.e., again there is only a single peak for the actual case of $\epsilon = 1$.

Another way to see that there is only one peak in the full χ_S is to substitute the expressions for the real parts of the susceptibilities, Eqs. (2.24)-(2.26), into the denominator of Eq. (2.28) and express the real part of the term $D = (1 - u_S\chi_S^0)(1 - u_\pi\chi_\pi^0) - u_S u_\pi(\chi_{S\pi}^0)^2$ via $\chi_\pi^0 = \chi_\pi^0(\omega)$. We obtain

$$\mathrm{Re}D = (1 - u_S L) - \left[u_S\frac{\omega^2}{4\Delta^2} + u_\pi(1 - u_S L)\right]\mathrm{Re}[\chi_\pi^0(\omega)]. \tag{2.29}$$

Because $(1 - u_S L)$ and $(1 - u_\pi\chi_\pi^0(0))$ are required to be positive for the stability of the paramagnetic state, at zero frequency, D is surely positive. At finite ω, the first term in (2.29) is positive, while the second one is negative and its magnitude monotonically

increases with increasing ω. As a result, the denominator crosses zero only once, at some $\omega < 2\Delta$.

The single resonance peak is a mixture of a spin-exciton and π-resonance and for the representative case shown in Fig. 2.4 its energy is smaller that that of spin-exciton and a π-resonance. This implies that, when both channels are attractive, the coupling between the two plays substantial role in determining the position of the true resonance. From this perspective, the resonance at $u_1 < 0$ can, at least partly, be viewed as a plasmon. A somewhat similar result has been earlier obtained in the analysis of the resonance in the cuprates in the parameter range where $\pi-$resonance is allowed [52, 69, 66, 67].

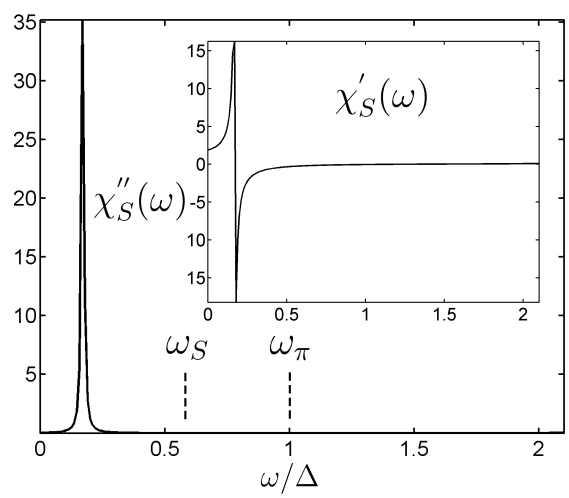

Figure 2.4: Imaginary part (main plot) and real part (insert) of the full spin susceptibility ($T = 0$, units of Δ^{-1}) in the case of $u_S = 30.5\Delta$ and $u_\pi = 130\Delta$. In the absence of coupling we would observe resonance peaks in the spin and π channels at frequencies $\omega_S \approx 0.57\Delta$ and $\omega_\pi \approx 1.0\Delta$, respectively, indicated on the plot.

2.5 Summary

We have studied the spin resonance at antiferromagnetic momentum (π, π) in an s^{+-} superconducting state of FeSCs by including contribution from the particle-particle channel, which in the superconducting state gets mixed with the particle-hole channel. We have shown that for purely repulsive interactions the inclusion of this channel does not qualitatively change the spin resonance, which remains predominantly spin-exciton

and only slightly shifts to higher frequencies. For attractive density-density interaction, when both spin-exciton resonance in the particle-hole channel and π-resonance in the particle-particle channel are allowed, we found that strong coupling between the two channels destroys the two-peak structure and only one peak survives, whose frequency is smaller than would be that of a spin-exciton and $\pi-$resonance in the absence of the coupling. We argued that strong coupling between the particle-hole and particle-particle channels is peculiar to the spin susceptibility, while for the charge susceptibility, which, e.g., is relevant for Raman scattering, the coupling is much smaller.

Chapter 3

Raman resonance: The magnetic scenario

3.1 Introduction

Raman scattering in Fe-based superconductors has attracted substantial interest in the past few years due to the number of new features associated with multi-orbital/multi-band nature of these materials (see, e.g., Refs. [17, 18, 79, 80, 81, 82, 83, 84, 85, 86]). The subject of this chapter is the theoretical analysis of the features in Raman scattering revealed by polarization-sensitive Raman spectroscopy in the normal and the superconducting states of Fe-based materials $NaFe_{1-x}Co_xAs$ [12], AFe_2As_2, A =Eu,Sr [13, 14], and $Ba(Fe_{1-x}Co_x)_2As_2$ [15, 16]. Polarized light was used to probe the Raman response in different symmetry channels, classified by the irreducible representations of the D_{4h} crystallographic point group [17, 18]. In the normal state the real part of the (almost) static and uniform Raman susceptibility in the B_{1g} channel in one-iron unit cell notation (same as the B_{2g} channel in two-iron notation used in Refs. [12, 13, 15]) is strongly temperature dependent—it increases below 300 K roughly as $1/(T - T_0)$, where T_0 is positive at small doping, but changes sign and becomes negative above optimal doping. In the superconducting state the imaginary part of the B_{1g} Raman susceptibility displays a strong resonance-type peak at around 50 cm^{-1}. There is no such resonance peak in other channels, although the Raman intensity in the A_{1g} channel does show a broad maximum at a somewhat higher frequency [12].

In the effective mass approximation (in which the coupling of light to fermions is proportional to the square of vector potential) the measured Raman intensity in a particular channel (A_{1g}, B_{1g}, B_{2g},...) is proportional to the imaginary part of the fully renormalized particle-hole polarization bubble $\chi_R(\mathbf{p}, \Omega)$ with proper symmetry factors in the vertices, taken at vanishingly small transferred momentum $\mathbf{p}$ and finite transferred frequency Ω [87, 88, 89].

The free-fermion polarization bubble vanishes in the normal state for $\Omega > v_F p$, where v_F is the Fermi velocity, and obviously it cannot account for the observed strong temperature dependence of B_{1g} Raman intensity above T_c. It is nonzero in the superconducting state, but does not display a peak. The effect must then come from the renormalization of the Raman vertex due to coupling to some low-energy fluctuations (final state interaction in Raman literature [90, 91]). This coupling may come from three different sources. First, the B_{1g} Raman vertex changes sign under $k_x \leftrightarrow k_y$ (i.e., under interchanging the x and y directions in real space), hence it couples to strain (structural fluctuations). Second, the B_{1g} vertex is anti-symmetric with respect to the interchange between the iron d_{xz} and d_{yz} orbitals and hence couples to orbital fluctuations. Third, symmetry allows the coupling between the B_{1g} Raman vertex and Ising-nematic spin fluctuations [the ones that distinguish between the magnitudes of spin-density-wave order parameters with ordering vectors $(0, \pi)$ and $(\pi, 0)$] because both are anti-symmetric with respect to 90° rotations in the momentum space.

Structural fluctuations, orbital fluctuations, and Ising-nematic spin-fluctuations are the three key candidates to drive the nematic order, observed in most of the Fe-based materials. How to choose the primary candidate among these three has become one of the key issues in the studies of Fe-based superconductors [92]. We intend to verify whether the Raman data can help distinguish between the three candidates.

The effects of structural and orbital fluctuations has been discussed before (see Refs. [93, 94, 95] and references therein). Structural fluctuations (acoustic phonons associated with strain) practically do not affect the Raman intensity because the coupling to phonons changes the B_{1g} Raman susceptibility $\chi_R(\mathbf{p}, \Omega)$ to

$$\tilde{\chi}_R(\mathbf{p}, \Omega) = \left[\chi_R^{-1}(\mathbf{p}, \Omega) - \frac{\lambda_{ph}^2 p^2}{C_{ph}^2 p^2 - \Omega^2} \right]^{-1}, \tag{3.1}$$

where λ_{ph} is electron-phonon coupling and C_{ph} is the elastic constant for orthorhombic

strain. Such coupling is relevant in the static limit, where $\tilde{\chi}_R^{-1}(\mathbf{p},0) = \chi_R^{-1}(\mathbf{p},0) - (\lambda_{ph}/C_{ph})^2$ differs from $\chi_R^{-1}(\mathbf{p},0)$ by a constant term, but is irrelevant in the limit of vanishing p and finite Ω, where Raman measurements have been performed [12, 15, 16]. (In the B_{1g} channel the minimum p is, strictly speaking, nonzero [96], but is generally of order of inverse system size).

Orbital fluctuations do affect the B_{1g} Raman susceptibility via renormalizations involving particular combinations of intra-orbital and inter-orbital Hubbard and Hund terms, compatible with the fact that the B_{1g} Raman vertex changes sign between d_{xz} and d_{yz} orbitals. By orbital fluctuations we mean fluctuations which renormalize the B_{1g} Raman vertex by inserting series of ladder and bubble diagrams, as shown schematically in Fig. 3.1 and in more detail in Figs. 3.17 and 3.18 in section 3.6.

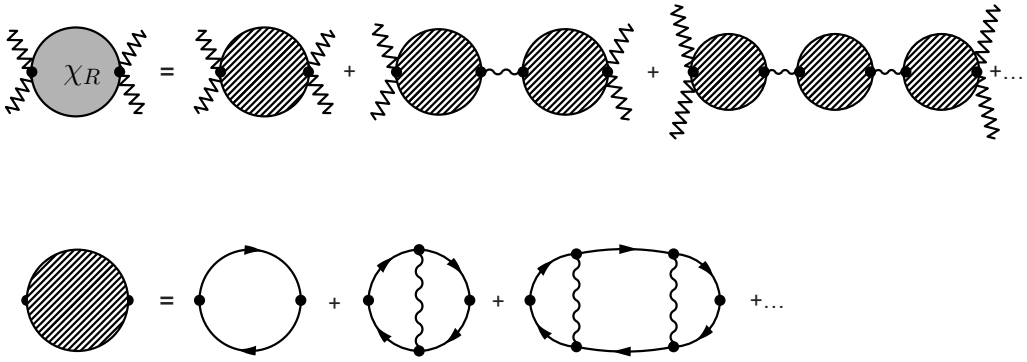

Figure 3.1: Ladder and bubble diagrams for the renormalization of the B_{1g} Raman intensity within RPA. Each combination of Green's functions with equal momenta gives a particle-hole polarization bubble $\Pi_{B_{1g}}(\Omega)$ and the combination of vertical and horizontal interaction lines gives the coupling λ. We obtain λ explicitly in section 3.6 for a system with dominant intra-orbital Hubbard interaction.

In the band basis, the interaction lines in these diagrams are Hubbard and Hund terms dressed by coherence factors, associated with the transformation from the orbital to the band basis, and projected into B_{1g} channel. (Each interaction contains one incoming and one outgoing fermion with momentum $\mathbf{k}$ and one incoming and one outgoing fermion with momentum $\mathbf{p}$, and its B_{1g} component is proportional to $\cos 2\theta_k \cos 2\theta_p$, where $\tan\theta_k = k_y/k_x$). In the approximation when only ladder and bubble diagrams are kept [often called random-phase approximation (RPA)], the Raman response in the

B_{1g} channel is given by (see, e.g., Ref. [97]),

$$\chi_R(\Omega) = \frac{\Pi_{B_{1g}}(\Omega)}{1 + \lambda \Pi_{B_{1g}}(\Omega)}, \tag{3.2}$$

where $\chi_R(\Omega) = \chi_R(p \to 0, \Omega)$, λ is the proper combination of interactions in B_{1g} channel, and $\Pi_{B_{1g}}(\Omega)$ is the particle-hole polarization function at zero momentum transfer, summed over all bands with the B_{1g} form factor. [We define $\Pi_{B_{1g}}(\Omega)$ as $i \int \mathrm{d}^2 k \mathrm{d}\nu/(2\pi)^3 \times G(k,\nu)G(k,\nu+\Omega)$. With this sign convention, Re $\Pi_{B_{1g}}(\Omega)$ in a superconductor is positive at $\Omega < 2\Delta$, where Δ is the superconducting gap]. In the language of Fermi-liquid theory, $\lambda \Pi_{B_{1g}}(\Omega = 0)$ is the B_{1g} component of the quasiparticle interaction function, and $\lambda \Pi_{B_{1g}}(\Omega = 0) = -1$ would correspond to a B_{1g} Pomeranchuk instability.

Because free-fermion $\Pi_{B_{1g}}(\Omega)$ vanishes in the normal state (the poles of both Green's functions are in the same frequency half plane), Eq. (3.2) cannot explain the normal state behavior of the Raman response. However, $\chi_R(\Omega)$ from Eq. (3.2) is nonzero in a superconductor, because $\Pi_{B_{1g}}(\Omega)$ becomes nonzero, and for negative λ it displays a resonance peak. The resonance develops by the same reason as the excitonic spin resonance in a d-wave superconductor [98]: the imaginary part of the polarization function $\Pi(\Omega)$ vanishes for $\Omega < 2\Delta$, while the real part of $\Pi(\Omega)$ is positive and diverges at $\Omega = 2\Delta$. As the result, for negative λ, the denominator in (3.2) is guaranteed to pass through zero at some frequency below 2Δ, and a sharp resonance in $\chi_R(\Omega)$ appears at this frequency [97].

This would be the most natural explanation of the Raman resonance. The problem, however, is how to justify that λ is negative, i.e., that there is an attraction in the B_{1g} (d-wave) charge Pomeranchuk channel. If intra-orbital Hubbard repulsion is the dominant interaction term, λ is definitely positive and orbital fluctuations do not give rise to the resonance in the Raman intensity (we show this in section 3.6). The coupling λ does become negative when inter-orbital interaction U' and exchange Hund interaction J are included and U' is set to be about equal to U and larger than J [99]. However, the relation $U' \approx U$ gets broken once one starts integrating out high-energy fermionic excitations [77, 100] or includes lattice effects [75]. In a generic case it is natural to expect that the intra-orbital Hubbard interaction is the strongest interaction between Fe d-orbitals. If so, the coupling λ is positive and there is no resonance in $\chi_R(\Omega)$ within

RPA.

In this chapter we analyze whether the increase of $\chi_R(\Omega)$ in the B_{1g} channel in the normal state and the sharp peak in the Raman response in this channel below T_c can be due to Ising-nematic spin fluctuations associated with stripe magnetism. The advantage of the magnetic scenario is that Ising-nematic fluctuations are enhanced even when intra-orbital Hubbard interaction is the dominant interaction between fermions. The only requirement is that the magnetic order should be stripe rather than checkerboard [101].

The coupling of the Raman vertex to a pair of spin fluctuations with momenta near $\mathbf{Q} = (0, \pi)$ [or $(\pi, 0)$] occurs via the Aslamazov-Larkin (AL) process. The corresponding diagram is presented in Fig. 3.2. AL diagrams for Raman scattering have been earlier discussed in Ref. [102, 103], but in a different context. The lowest-order AL type diagram (the one shown in Fig. 3.2) contains two triangular vertices made out of fermionic Green's functions from hole and electron bands, and two spin-fluctuation propagators. The vertex between fermions and spin fluctuations can be obtained by decomposing the antisymmetrized interaction into spin and charge parts, by focusing on spin-spin part, and by using the Hubbard-Stratonovich method to transform the interaction between fermionic spins into spin-spin interaction between a fermion and a collective bosonic variable in the spin channel [101].

We show that in the normal state, above a certain temperature, each triangular vertex Γ_{tr} scales as $1/T$, while the convolution of the two spin propagators at equal frequencies (i.e., $T\sum_{\nu_n}\int d^2\mathbf{q}/(2\pi)^2 \times [\chi^s(\mathbf{Q}+\mathbf{q}, \nu_n)]^2$) scales as T. As the consequence, the Raman susceptibility from Fig. 3.2 scales as $1/T$. This holds in both A_{1g} and B_{1g} channels. Higher-order processes, shown in Fig. 3.3 and in more detail in Fig. 3.6 below, however, distinguish between A_{1g} and B_{1g} Raman responses. Namely, an attractive interaction between magnetic fluctuations in the B_{1g} channel increases B_{1g} Raman response and changes $1/T$ dependence into $1/(T - T_0)$ (see Refs. [104], [105] and Sec.III below), while the (much stronger) repulsive interaction in the A_{1g} channel almost completely eliminates the temperature dependence of A_{1g} Raman response. This behavior fully agrees with the data.

In the superconducting state, the $1/T$ behavior of Γ_{tr} is cut by the gap opening, while $\chi^2(\Omega) = \int d\nu d^2\mathbf{q}/(2\pi)^3 \times \chi^s(\mathbf{q}+\mathbf{Q}, \nu)\chi^s(\mathbf{q}+\mathbf{Q}, \nu+\Omega)$ becomes singular. The

real part of $\chi^2(\Omega)$ diverges at $\Omega = 2\Omega_{mag}$, where Ω_{mag} is the minimal frequency of the magnetic resonance in the superconducting state, and its imaginary part jumps at this frequency from zero to a finite value. Higher-order terms change $\chi^2(\Omega)$ into $\chi_{I-nem}(\Omega) = \chi^2(\Omega)/[1 + 2g\chi^2(\Omega)]$ (see Sec. III), where g is negative (attractive) when magnetic order is of stripe type [101]. Approximating the triangular vertex Γ_{tr} by a constant we then obtain

$$\chi_R(\Omega) = \Gamma_{tr}^2 \chi_{I-nem}(\Omega) = \Gamma_{tr}^2 \; \frac{\chi^2(\Omega)}{1 + 2g\chi^2(\Omega)}. \tag{3.3}$$

The combination of $g < 0$ and the fact that the real part of $\chi^2(\Omega)$ is positive and diverges at $\Omega = 2\Omega_{mag}$ guarantees that $1 + 2g\chi^2(\Omega)$ passes through zero at some $\Omega = \Omega_{res,1} < 2\Omega_{mag}$. At this frequency the Raman intensity Im $\chi_R(\Omega)$ displays a δ-functional peak.

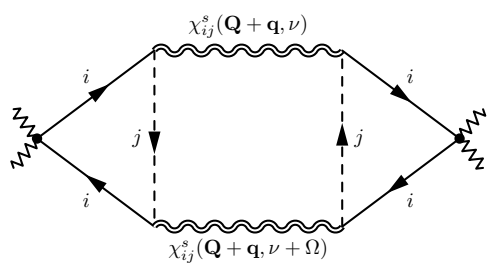

Figure 3.2: The lowest order (two-loop) AL diagram for the Raman intensity. The momenta $\mathbf{Q}_1 = (\pi, 0)$ and $\mathbf{Q}_2 = (0, \pi)$. The solid and dashed lines represent fermions from different bands with band indices i and j. The sinuous lines represent spin fluctuations and the external jagged lines are the coupling to photons.

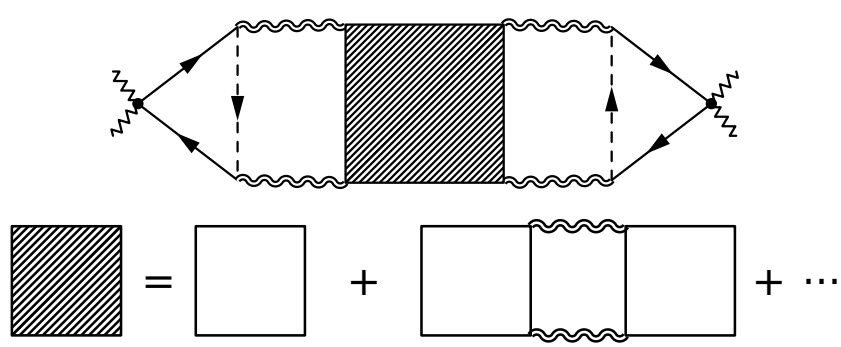

Figure 3.3: Schematic representation of higher-order contributions to the Raman response. We show higher-order terms in more detail in Fig. 3.6.

We show that approximating Γ_{tr} by a constant is justified if typical fermionic frequencies in the triangular diagram for Γ_{tr} are larger than Ω_{mag}. These relevant frequencies are of order Δ, hence the analysis is justified when $\Omega_{mag} \ll \Delta$. This holds if the inverse magnetic correlation length m_s is small enough because $\Omega_{mag} \propto m_s$ [106]. In the Fe-based materials, in which B_{1g} resonance has been observed, the situation is, however, somewhat different: neutron scattering data for $NaFe_{1-x}Co_xAs$ with $x = 0.045$ show [107] that $\Omega_{mag} \approx 7$ meV, while $\Delta = 5 - 5.5$ meV [108], i.e., Δ is somewhat smaller than Ω_{mag}. Similarly, for $Ba(Fe_{1-x}Co_x)_2As_2$ with x=0.075, $\Omega_{mag} \approx 9.5$ meV [35], while $\Delta = 4.5 - 5$meV on the electron pocket and 7 meV on the hole pocket [109], so again $\Delta < \Omega_{mag}$. In this situation, there is no good reason to treat Γ_{tr} as a constant, independent on Ω_{mag}, because two fermionic frequencies in the triangular loop differ by Ω_{mag}.

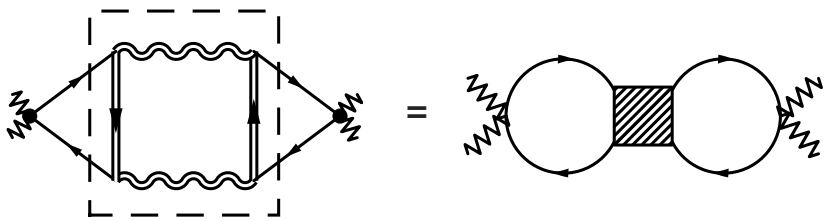

Figure 3.4: Interpretation of the two-loop AL diagram as consisting of two particle-hole bubbles with zero momentum transfer (unshaded circles), separated by the magnetically-mediated four-fermion interaction. The notations are the same as in Fig. 3.2. Higher-order terms are shown in Fig. 3.8.

In view of this complication, we also analyze another scenario for the B_{1g} resonance below T_c, namely, that the resonance originates from the 2Δ singularity of the particle-hole polarization $\Pi_{B_{1g}}(\Omega)$ in an s-wave superconductor, like in the pure orbital fluctuation scenario, while spin fluctuations renormalize the original, likely repulsive, coupling λ in Eq. (3.2) into the effective coupling λ_{eff} (see Figs. 3.4). This scenario is justified in the opposite limit when Ω_{mag} is assumed to be much larger than Δ. The strong inequality never holds because $\Omega_{mag} < 2\Delta$, but the weak inequality may be already enough number-wise. We show that λ_{eff} turns out to be negative (i.e., attractive) near a nematic instability. For negative λ_{eff}, $1 + \lambda_{eff}\Pi_{B_{1g}}(\Omega)$ necessary vanishes at some frequency $\Omega_{res,2}$ below 2Δ, where $\mathrm{Im}\Pi_{B_{1g}}(\Omega)$ is zero, and this leads

to an excitonic-type resonance in the B_{1g} Raman response.

Such a scenario has been proposed in earlier works [16, 97] based on the phenomenological argument that Ising-nematic and orbital order parameters break the same C_4 symmetry and hence are linearly coupled in the Landau functional (see e.g., Ref. [110, 111]). A bilinear term with a constant prefactor A was argued to give rise to the renormalization of λ into $\lambda_{eff} = \lambda - A^2\chi_{I-nem}$. The latter is obviously negative when χ_{I-nem} is large. We compute the renormalization of λ within our microscopic model. We show that λ_{eff} does become negative and scales as χ_{I-nem}. However, the prefactor is not A^2 and is nonzero only if one includes the non-analytic dynamical Landau damping term into the spin propagator. If spin-fluctuation propagator is approximated by its static part, $\lambda_{eff} = 0$. We explain the difference between the coupling between Pomeranchuk order parameter and two spin fluctuations (= A) and between Ising-nematic and orbital (Pomeranchuk) order parameters, which actually gives rise to the renormalization of λ.

The outcome of this study is that the resonance in B_{1g} Raman intensity is of purely magnetic origin at $\Omega_{mag} \ll \Delta$—it is due to the pole in $\chi_{I-nem}(\Omega)$ at $\Omega_{res,1}$. At $\Omega_{mag} > \Delta$ the resonance of fermionic origin—it develops by the same reason as in purely orbital scenario, due to the emergence of the excitonic pole in the ladder series of particle-hole bubbles with B_{1g} vertices. However, the attraction between fermions in the B_{1g} channel comes from magnetically mediated interaction.

In FeSCs, Ω_{mag} and Δ are comparable, in which case the actual resonance is likely the mixture of the nematic and the excitonic resonances. In $NaFe_{1-x}Co_xAs$ with $x = 0.045$, the B_{1g} peak is seen at 7.1 meV [12], which is below both 2Δ and $2\Omega_{mag}$. Similarly, in $Ba(Fe_{1-x}Co_x)_2As_2$ with x=0.061, the B1g peak is seen at 8.7 meV [15] , which is also below both 2Δ and $2\Omega_{mag}$.

The chapter is organized as follows: In Sec. 3.2 we evaluate analytically the two-loop AL-type diagram for B_{1g} Raman scattering. In Sec. 3.3 we show that in the normal state this contribution to $\chi_R(\Omega)$ is strongly temperature dependent. The temperature dependence is roughly $1/T$. We argue that higher-order terms, which include interactions between pairs of spin fluctuations, replace $1/T$ dependence into more singular $1/(T - T_0)$. In Sec. 3.4 we extend the analysis to the superconducting state. In Sec. 3.4.1 we argue that spin excitations with momenta near $(0, \pi)$ and $(\pi, 0)$ evolve below

T_c and become magnon-like, with minimal energy Ω_{mag}. We compute the two-loop AL diagram assuming that the vertices that couple light to spin fluctuations saturate below T_c, and show that this contribution to Raman intensity becomes logarithmically singular at $\Omega = 2\Omega_{mag}$. We further show that higher-order terms, which include interactions between spin fluctuations, convert logarithmical singularity at $2\Omega_{mag}$ into a true resonance peak at an energy $\Omega_{res,1} < 2\Omega_{mag}$. In Sec. 3.4.2 we re-interpret the two-loop AL diagram for B_{1g} Raman scattering differently, as the contribution from two particle-hole polarization bubbles with an effective interaction mediated by spin fluctuations. We compute the magnetically mediated four-fermion interaction λ_{mag} and show that it is attractive. We argue that higher-order terms give rise to an excitonic peak in $\chi_R(\Omega)$ at $\Omega_{res,1}$ below 2Δ. In Sec. 3.4.3 we discuss the interplay between this peak and the one coming from fully renormalized nematic susceptibility. In Sec. 3.4.4 we present the results of numerical computation of spin-fluctuation contribution to Raman intensity at two-loop and higher orders. In Sec. 3.5 we compare AL vertices for the coupling to spin fluctuations in different symmetry channels and show that in the B_{2g} channel (in the 1-Fe zone) the vertex for the coupling of light to spin fluctuations vanishes by symmetry. The vertex in A_{1g} channel does not vanish and is of the same order as the vertex in B_{1g} channel. We show, however, that there is no resonance in A_{1g} because the interaction between spin fluctuations in this channel is strongly repulsive instead of attractive. We present our conclusions in Sec. 3.7.

Throughout the chapter we will be using band formalism and will be working in the 1-Fe Brillouin zone (BZ).

3.2 Raman response from spin fluctuations

We consider the four-band model of $NaFe_{1-x}Co_xAs$ and $Ba(Fe_{1-x}Co_x)_2As_2$ with two hole pockets centered at $k_x = k_y = 0$ and two electron pockets centered at $(0, \pi)$ and $(\pi, 0)$ in the 1 Fe Brillouin zone (BZ), see Refs. [112, 113, 114, 115]. Excitations near the hole pockets are composed out of d_{xz} and d_{yz} orbitals and there is 90° rotation of the orbital content near one Fermi surface compared to the other. Excitations near electron pockets are predominantly composed out of d_{xy} and d_{xz} orbitals for the $(0, \pi)$ pocket and out of d_{xy} and d_{yz} orbitals for the $(\pi, 0)$ pocket [59]. We do not include into

consideration the third hole pocket, centered at (π, π) in the 1Fe zone, as it is made out of C_4-symmetric d_{xy} orbital and does not play any significant role in the analysis of Raman scattering, particularly in B_{1g} geometry.

The Raman response function can be calculated as a time-ordered average of density operators weighted with Raman form factors:

$$\chi_R(\mathbf{p}, \Omega) = -i \int \mathrm{d}t e^{i\Omega t} \left\langle T \rho_{\mathbf{p}}(t) \rho_{-\mathbf{p}}(0) \right\rangle, \tag{3.4}$$

where

$$\rho_{\mathbf{p}} \equiv \sum_{i,\mathbf{k},\sigma} \gamma_i(\mathbf{k}) c^{\dagger}_{i,\mathbf{k}+\mathbf{p},\sigma} c_{i,\mathbf{k},\sigma}. \tag{3.5}$$

Here i represents a band index, σ represents a spin projection of a fermion, and $\gamma(\mathbf{k})$ is the Raman form factor, which keeps track of the polarizations of the incoming and the outgoing light. The use of light of different polarizations allows the probing of different symmetry channels: A_{1g}, A_{2g}, B_{1g}, and B_{2g}. Note that the B_{1g} and B_{2g} channels are interchanged when going from the 1-Fe BZ to the 2-Fe BZ, because the coordinate system is rotated 45° to make the k_x and k_y axes coincide with the sides of the square cell. Because the wavelength of light used in the experiments is a few orders of magnitude greater than the lattice constant, the typical values of $v_F p$ are smaller than typical Ω, and it suffices to calculate the susceptibility at $p \to 0$, i.e., compute $\chi_R(\Omega) \equiv \chi_R(p \to 0, \Omega)$.

Without the final state interaction, the Raman response involving a pair of spin fluctuations with momenta near $(0, \pi)$ and $(\pi, 0)$ (the difference between the centers of electron and hole pockets) is given by the diagram shown in Fig. 3.2. Since light can couple to each hole and electron band, there are several diagrams of this kind with two fermionic lines from one of hole pockets or from one of electron pockets (see Fig. 3.16 below). The combined contribution from these diagrams takes the form

$$\begin{aligned}\chi_R(\Omega) = &- i \int \frac{\mathrm{d}^2\mathbf{q}\mathrm{d}\nu}{(2\pi)^3} \Gamma^2_{tr,l}(\mathbf{q}, \nu) f_l \chi^{\mathrm{s}}(\mathbf{Q}_l + \mathbf{q}, \nu) \\ &\times \chi^{\mathrm{s}}(\mathbf{Q}_l + \mathbf{q}, \nu + \Omega),\end{aligned} \tag{3.6}$$

where $\Gamma_{tr,l}$ defines the vertex for the coupling between light and spin fluctuations (see Fig. 3.5), χ^{s} is the propagator of spin fluctuations, $l = 1, 2$ with $\mathbf{Q}_1 = (\pi, 0)$, $\mathbf{Q}_2 = (0, \pi)$, and f_l is the symmetry factor, e.g., $f_l = \sigma^z_{ll}$ for B_{1g} geometry.

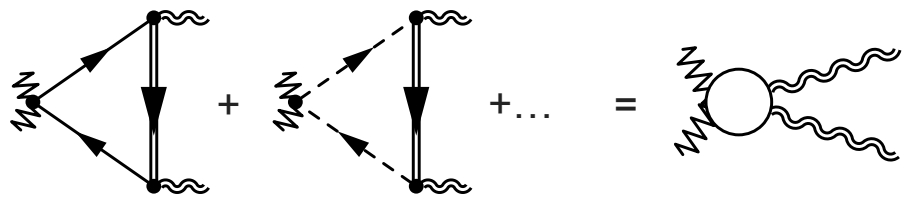

Figure 3.5: The AL vertex Γ_{tr} for the coupling of light to spin fluctuations. Single solid and dashed lines represent excitations from one of the two hole bands and the double solid line represents excitations from one of the two electron bands. When typical internal frequencies in the triangle made out of fermionic Green's functions are larger than typical frequencies of spin fluctuations, Γ_{tr} can be approximated by a constant (a circle on the right-hand side of the figure).

The vertex $\Gamma_{tr,l}(\mathbf{q},\nu)$ is composed out of three fermionic Green's functions, the Raman factor $\gamma(\mathbf{k})$, and two vertices for the coupling between fermions and spin-fluctuations: $g_{sf}\gamma_{ij}(\mathbf{k},\mathbf{k}+\mathbf{Q}_l-\mathbf{q})$, where g_{sf} is the spin-fermion coupling (or order of the intra-orbital Hubbard U) and $\gamma_{ij}(\mathbf{k},\mathbf{k}+\mathbf{Q}_l-\mathbf{q})$ are coherence factors associated with the transformation from orbital to band basis for fermions from bands i and j $(i,j=1,2)$. In a superconducting state one must include diagrams containing anomalous Green's functions, which create or destroy particles in pairs, and sum over all allowed combinations of normal and anomalous functions. For any particular combination of normal and anomalous functions, the triangular vertex takes the form

$$\begin{aligned}\Gamma_{tr,l}(\mathbf{q},\nu) =& g_{sf}^2\int\frac{\mathrm{d}^2\mathbf{k}\mathrm{d}\omega}{(2\pi)^3}\gamma_i(\mathbf{k})\gamma_{ij}^2(\mathbf{k}+\mathbf{Q}_l-\mathbf{q})\\ &\times\tilde{G}_i(\mathbf{k},\omega)\tilde{G}_i(\mathbf{k},\omega+\Omega)\tilde{G}_j(\mathbf{k}+\mathbf{Q}_l-\mathbf{q},\omega-\nu),\end{aligned}\tag{3.7}$$

where $\tilde{G}_{i,j}$ are either normal (G) or anomalous (F) Green's functions with i from a hole pocket and j from an electron pocket or vice versa. The index of the electron band is equal to l.

3.3 The vertex function in the normal state and the temperature dependence of the B_{1g} susceptibility above T_c

In this section we compute the Raman vertex function in the normal state and obtain the temperature dependence of the real part of the Raman susceptibility in the static limit. Here and in Sec. 3.4 we focus on B_{1g} scattering geometry with $\gamma(\mathbf{k}) \propto \cos \mathbf{k_x} - \cos \mathbf{k_y}$ and do not explicitly write symmetry factors in the Raman vertex and in the vertices relating fermions with spin fluctuations. We will discuss these symmetry factors and different geometries in Sec. 3.5. We also neglect for simplicity the eccentricity of the electron pockets and set all Fermi surfaces to be circles of the same size. This approximation simplifies calculations, but does not qualitatively affect the temperature dependence compared to a generic case in which the pockets are different. In the static limit Eq. (3.7) in the normal state reduces to

$$\Gamma_{tr}(\mathbf{q}, \nu_n) = -AT \sum_{\omega_m} \int \frac{\mathrm{d}^2\mathbf{k}}{(2\pi)^2} \frac{1}{(i\omega_m - \xi^i_{\mathbf{k}})^2} \frac{1}{i(\omega_m - \nu_n) - \xi^j_{\mathbf{k}-\mathbf{q}}}, \tag{3.8}$$

where $A \sim g_{sf}^2$. For concreteness we assume that i is a hole band and j is an electron band. The hole and electron dispersions are given by $\xi^i_{\mathbf{k}} = \mu - \frac{k^2}{2m} = -\xi^j_{\mathbf{k}}$, where μ is the chemical potential. At $\mathbf{q} = 0$ and $\nu_m = 0$, Γ_{tr} is given by

$$\Gamma_{tr} = \frac{Am}{16\pi T} f\left(\frac{\mu}{2T}\right).$$

The scaling function $f(x) = \tanh(x)/x$ is close to 1 for $x < 1$, i.e., for $T > \mu/2$. In this temperature range $\Gamma_{tr} \approx Am/(16\pi T)$ scales as $1/T$. This has been noticed before [116]. At larger x (smaller T), Γ_{tr} tends to a constant [105]. At a nonzero $\mathbf{q}$ and ν_m the expression for Γ_{tr} becomes more complex, but as long as $\nu_m = O(T)$ and $|\mathbf{q}| \leq k_F$, the functional form remains the same.

We next compute the convolution of two spin fluctuations in the normal state. There is no controllable way to obtain the spin-fluctuation propagator starting from the fermion-fermion interaction. The RPA procedure is often used, but it selects particular series of ladder and bubble diagrams in the particle-hole channel and neglects contributions from the particle-particle channel. The latter are, however, not small, even

at perfect nesting [8, 117]. Besides, in a general case of hole and electron pockets of different sizes and geometry, the static propagator of spin fluctuations comes from fermions with energies of order bandwidth, for which the low-energy expansion is not applicable. In view of this complication, we adopt the same approach as in earlier works on the spin-fermion model [118] and assume phenomenologically that the static part of the spin-fluctuation propagator has a regular Ornstein-Zernike form $\chi^s_{ij}(\mathbf{q}+\mathbf{Q},0) = 1/(q^2+m_s^2)$, where m_s is the inverse magnetic correlation length (the overall factor in χ^s is incorporated into the spin-fermion coupling). The dynamical part of χ^s, however, comes from low-energy fermions and can be obtained by computing the dynamical part of particle-hole polarization bubble made of fermions near a hole and an electron pocket, separated by $\mathbf{Q}$. Then

$$\chi^s(\mathbf{Q}+\mathbf{q},\nu_m) = \frac{1}{m_s^2+q^2+\gamma\Pi_Q(\nu_m)}, \tag{3.9}$$

where $\gamma = mg_{sf}/(2\pi)$, g_{sf} is the spin-fermion coupling [118], and $\Pi_Q(\nu_m) = \Pi(\mathbf{Q},\nu_m) - \Pi(\mathbf{Q},0)$, where $\Pi(\mathbf{Q},\nu_m)$ is the dynamical polarization bubble at momentum transfer $\mathbf{Q}$. The polarization bubble $\Pi_Q(\nu_m)$ is logarithmic in ν_m because it is the convolution of fermions from hole and electron bands with opposite sign of the dispersion [119]. We computed $\Pi_Q(\nu_m)$ numerically and found that it can be well approximated by

$$\Pi_Q(\nu_m) = \log\left(3.57\frac{|\nu_m|}{2\pi T}\right) \tag{3.10}$$

starting already from the lowest nonzero Matsubara frequency. Substituting this into (3.9) and evaluating the convolution of the two dynamical spin susceptibilities with the same momentum and frequency we obtain

$$\begin{aligned} &T\sum_{\nu_m}\int\frac{\mathrm{d}^2\mathbf{q}}{(2\pi)^2}\chi^s(\mathbf{q}+\mathbf{Q},\nu_m)\chi^s(\mathbf{q}+\mathbf{Q},\nu_m) \\ &\propto T(m_s)^{-2}\left(1+\sum_{m\neq 0}\frac{1}{1+\gamma(m_s)^{-2}\log\left(3.57|m|\right)}\right) \end{aligned} \tag{3.11}$$

The coupling constant γ cannot be calculated within the theory, but is generally of order 1. Assuming that this is the case, we find that the dominant contribution to the sum over bosonic Matsubara frequencies comes from the term with $\nu_n = 0$, at least when the inverse magnetic correlation length $m_s < 1$. The convolution of the two χ^s then

gives, up to a constant prefactor, T/m_s^2 [94, 95]. Combining this with $\Gamma_{tr}^2 \propto 1/T$, we obtain that the contribution to the static B_{1g} Raman susceptibility from the processes involving a pair of spin fluctuations with momenta near $(0, \pi)$ and $(\pi, 0)$ and two triple vertices (i.e., from the diagram in Fig. 3.2) is given by

$$\chi_R(\Omega = 0) \propto \frac{1}{T m_s^2} \tag{3.12}$$

Outside the T range near a magnetic transition, the temperature dependence of m_s is weak, and $\chi_R(\Omega = 0)$ scales roughly as $1/T$.

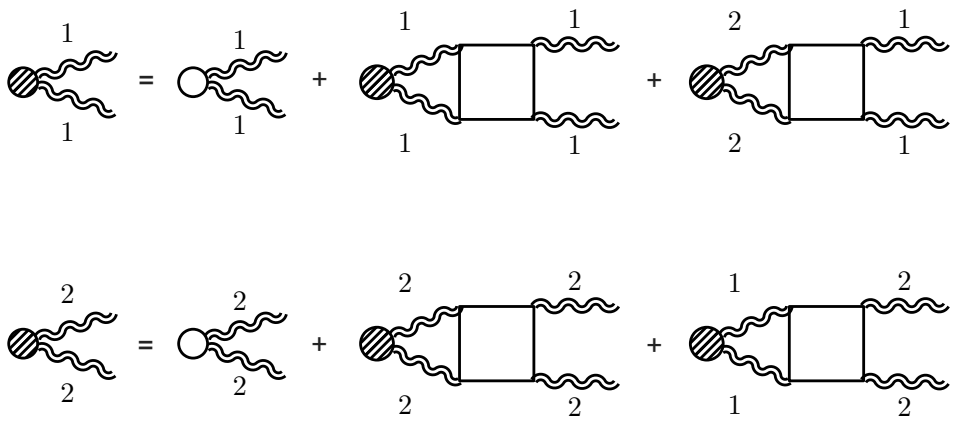

Figure 3.6: Ladder series of renormalizations of the interaction of light with spin fluctuations with momenta near $\mathbf{Q}_1 = (\pi, 0)$ (labeled as 1) and near $\mathbf{Q}_2 = (0, \pi)$ (labeled as 2). The interaction vertices are made out of fermions from different bands (see Fig. 3.7).

3.3.1 Higher-order contributions to Raman susceptibility

We next consider how Eq. (3.12) changes once we include the interactions between pairs of spin fluctuations. These interactions either leave bosonic momenta near a particular $\mathbf{Q}_1 = (\pi, 0)$ or $\mathbf{Q}_2 = (0, \pi)$, or transfer both momenta from $\mathbf{Q}_1$ to $\mathbf{Q}_2$ or vice versa. In the latter case, the process belongs to the umklapp category and is allowed because $2\mathbf{Q}_1 = 2\mathbf{Q}_2$ up to reciprocal lattice vector. We show the corresponding diagrams in Fig. 3.6. Each interaction vertex is given by the convolution of four fermionic propagators (see Fig. 3.7). These vertices have been computed in Ref. [101] in the limit when

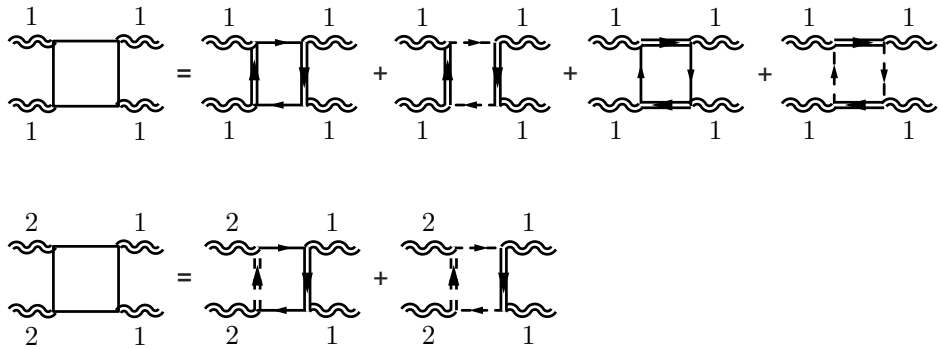

Figure 3.7: The structure of the vertices for the interaction between spin fluctuations with near $\mathbf{Q}_1 = (\pi, 0)$ (labeled as 1) and near $\mathbf{Q}_2 = (0, \pi)$ (labeled as 2). The single solid and dashed lines represent excitations from one of the two hole bands and the double solid and dashed lines represent excitations from one of the two electron bands.

bosonic frequencies are set to zero. We argued above that this approximation is justified for the two-loop diagram, and we now assume that this also holds for higher-order processes. We then borrow the results from Ref. [101], which demonstrated that the effective interaction in the B_{1g} channel is a negative (attractive) $2g$, which scales with temperature as $1/T^4$.

We show explicitly how to solve the coupled set of ladder equations for the fully renormalized AL vertices with momenta $\mathbf{Q}_1$ and $\mathbf{Q}_2$ later in Sec. 3.5 (where we compare A_{1g} and B_{1g} channels), because the set involves both A_{1g} and B_{1g} components. Here we just present the result: at small Ω, interactions between spin-fluctuations change the two-loop AL Raman vertex in B_{1g} geometry into

$$\chi_R(\Omega) = \Gamma_{tr}^2 \frac{\chi^2(\Omega)}{1 + 2g\chi^2(\Omega)} = \Gamma_{tr}^2 \ \chi_{I-nem}(\Omega), \tag{3.13}$$

where $\chi^2(\Omega)$ is the short notation for the convolution of two spin-fluctuation propagators with relative frequency Ω and we defined

$$\chi_{I-nem}(\Omega) = \frac{\chi^2(\Omega)}{1 + 2g\chi^2(\Omega)}. \tag{3.14}$$

Using $g \sim 1/T^4$, $\chi^2 \propto T$, $\Gamma_{tr} \propto 1/T$, and introducing T_0 as a temperature at which

$2g\chi^2 = 1$, we obtain

$$\chi_R(0,T) \sim \frac{(m_s)^{-2}}{T-T_0}\left(\frac{T^2}{T^2+TT_0+T_0^2}\right), \tag{3.15}$$

which for $T > T_0$ is rather well approximated by

$$\chi_R \sim \frac{1}{T-T_0}. \tag{3.16}$$

In Sec. 3.5 we show that singular $1/(T-T_0)$ dependence only holds for the B_{1g} Raman vertex. In other channels, Raman intensity from the coupling to spin fluctuations either vanishes by symmetry of is substantially reduced by interaction between spin fluctuations.

The $1/(T-T_0)$ behavior of the B_{1g} Raman vertex is quite consistent with the experimental observations for $NaFe_{1-x}Co_xAs$, $EuFe_2As_2$, and $Ba(Fe_{1-x}Co_x)_2As_2$ [12, 13, 15, 16]. In these materials T_0 is positive at doping below a certain x_0. This T_0 would be the temperature of Ising-nematic instability in the absence of (i) superconductivity and (ii) coupling to phonons. Superconductivity obviously cuts $1/(T-T_0)$ behavior at T_c, if T_c is larger than T_0. The coupling to static phonons shifts the the coupling g to $g_{eff} = g + (\Gamma_{tr}\lambda_{ph}/C_{ph})^2/2$ [see Eq. (3.1)] and hence shifts the temperature of the Ising-nematic instability to $T_{nem} > T_0$. We remind that this shift is not present in the "static" χ_R, extracted from the measured Im $\chi_R(\Omega)$ by Kramers-Kronig transformation, because the contribution from phonons rapidly drops at nonzero Ω and is negligibly small for frequencies at which Im $\chi_R(\Omega)$ has been measured. As a result, "static" B_{1g} susceptibility extracted from the Raman data increases upon decreasing T but does not diverge even at T_{nem}.

Note also that T_0 is positive as long as magnetic order is a stripe, otherwise $g > 0$ and the final state interaction reduces rather than enhances the Raman intensity. Recent studies have shown [120, 121, 122, 123] that g does change sign as doping increases, hence one should expect that T_0 will change sign from positive to negative above a certain doping. This is fully consistent with the data [12].

3.4 The resonance in B_{1g} channel below T_c

We now turn to the superconducting state. We first argue in Sec. 3.4.1 that under certain conditions the resonance in B_{1g} Raman response is due to the development of

the pole in $\chi_{I-nem}(\Omega)$, given by (3.14). In Sec. 3.4.2 we consider another scenario for the resonance. Namely, we re-interpret the two-loop diagram as containing two dynamical particle-hole polarization bubbles with zero momentum transfer, $\Pi_{B_{1g}}(\Omega)$, coupled by an effective interaction mediated by spin fluctuations (see Figs. 3.4, 3.8). This effective interaction renormalizes λ in Eq. 3.2 into λ_{eff}, and we show that λ_{eff} becomes negative. As we said in the Introduction, for negative coupling the system develops an excitonic resonance in the superconducting state, at a frequency below twice the superconducting gap.

3.4.1 Resonance due to the pole in χ_{I-nem}

To analyze the form of χ_{I-nem} at $T = 0$ in a superconductor we need to know the form of $\chi^s(\mathbf{Q}+\mathbf{q},\nu)$ along the real frequency axis. As in earlier works, we assume that the symmetry of the superconducting order parameter is s^{+-}. Superconductivity does not affect the static form of χ^s as it generally comes from high-energy fermions, but changes the form of the dynamical term $\Pi_Q(\nu) = \Pi_s(\mathbf{Q},\nu) - \Pi_s(\mathbf{Q},0)$ in Eq. (3.9) (converted to real frequencies), as this term now contains the sum of G_sG_s and F_sF_s terms. Approximating fermionic dispersion in the same way as before we obtain

$$\Pi_s(\mathbf{Q},\nu) = \frac{1}{2}\int \frac{\mathrm{d}^2\mathbf{k}}{(2\pi)^2}\left[\frac{1}{\nu+2E_{\mathbf{k}}-i\eta} - \frac{1}{\nu-2E_{\mathbf{k}}+i\eta}\right], \tag{3.17}$$

where $E_{\mathbf{k}}^2 = \xi_{\mathbf{k}}^2 + \Delta^2$ and $\xi_{\mathbf{k}} = \mu - \frac{k^2}{2m}$ (note that we define Π without a spin factor of 2). In principle, in evaluating $\Pi_s(\mathbf{Q},\nu)$ one has to include also G_sF_s terms and combine renormalizations in the particle-hole and the particle-particle channels because in the superconducting state particles and holes are mixed as was argued in Chapter 2. The work in the Chapter, however, showed that as long as all the interactions are repulsive, the effect of inclusion of these extra terms is minimal in the case of Fe pnictides and merely shifts the resonance frequency (see below) down by a few percentage points.

The straightforward analysis shows that $\mathrm{Im}\,\Pi_Q(\nu)$ vanishes for $|\nu| < 2\Delta$ because the excitations are gapped. At $|\nu| = 2\Delta$, $\mathrm{Im}\,\Pi_Q(\nu)$ undergoes a discontinuous jump to a finite value and $\mathrm{Re}\,\Pi_Q(\mu)$ diverges logarithmically. The divergence of the real part of $\Pi_Q(\nu)$ at $\nu = 2\Delta$ implies that the denominator in (3.9) must vanish at some frequency below 2Δ, thus creating a pole in $\chi^s(\mathbf{Q}+\mathbf{q},\nu)$. Specifically, for a given $\mathbf{q}$, $\mathrm{Im}\,\chi^s(\mathbf{Q}+\mathbf{q},\nu)$ has sharp peak at frequency $\nu_{res}(\mathbf{q})$ and $\mathrm{Re}\,\chi^s(\mathbf{Q}+\mathbf{q},\nu)$ diverges. This

is indeed nothing but the spin resonance in an s^{+-} superconductor [53, 124]. Because time-ordered $\Pi_Q(\nu)$ is an even function of ν, it follows that for a given $\mathbf{q}$, time-ordered $\chi^s(\mathbf{Q}+\mathbf{q},\nu)$ has two simple poles at $\nu = \pm\nu_{res}(\mathbf{q})$. Then χ^s can be written as

$$\chi^s(\mathbf{Q}+\mathbf{q},\nu) = \frac{a(\mathbf{q},\nu)}{[\nu+\nu_{res}(\mathbf{q})][\nu-\nu_{res}(\mathbf{q})]}, \tag{3.18}$$

where $a(\mathbf{q},\nu)$ is some analytic function, which is also even in ν.

We now turn to the Raman susceptibility from the two-loop diagram, Eq. (3.6). We assume and then verify that the triangular Raman vertex Γ_{tr} can be approximated by a constant and taken out of the integral for χ_R. The $1/T$ temperature dependence of Γ_{tr} is obviously cut by T_c, i.e., it remains finite at $T=0$. Whether it can be taken out of the integral over the bosonic frequency is a more subtle issue and we discuss it at the end of this section.

With Γ_{tr} approximated by a constant, the expression for the Raman susceptibility takes the form

$$\chi_R(\Omega) = \Gamma_{tr}^2\chi^2(\Omega), \tag{3.19}$$

where

$$\chi^2(\Omega) = -i\int \frac{\mathrm{d}^2\mathbf{q}\mathrm{d}\nu}{(2\pi)^3}\sigma_{ii}^z\chi^{\mathrm{s}}(\mathbf{Q}_i+\mathbf{q},\nu)\chi^{\mathrm{s}}(\mathbf{Q}_i+\mathbf{q},\nu+\Omega). \tag{3.20}$$

where we remind that $i=1,2$, $\mathbf{Q}_1=(\pi,0), \mathbf{Q}_2=(0,\pi)$, and σ_{ii}^z is present because we consider B_{1g} geometry.

Substituting χ_s from (3.18) into Eq. (3.20) and evaluating the frequency integral, we obtain, neglecting symmetry factors,

$$\chi^2(\Omega) = -\int \frac{\mathrm{d}^2\mathbf{q}}{(2\pi)^2}\frac{a[\mathbf{q},\nu_{res}(\mathbf{q})]}{2\nu_{res}(\mathbf{q})\Omega} \tag{3.21}$$

$$\times\left[\frac{a[\mathbf{q},\Omega-\nu_{res}(\mathbf{q})]}{\Omega-2\nu_{res}(\mathbf{q})}+\frac{a[\mathbf{q},\Omega+\nu_{res}(\mathbf{q})]}{\Omega+2\nu_{res}(\mathbf{q})}\right]. \tag{3.22}$$

This formula shows that for each momentum $\mathbf{q}$ there is an enhancement of the response at twice the frequency $\nu_{res}(\mathbf{q})$. We define the minimum value of $\nu_{res}(\mathbf{q})$ as Ω_{mag}. A simple experimentation with the momentum integral shows that Im χ^2 is small at $\Omega < 2\Omega_{mag}$, but enhances sharply at $\Omega \geq 2\Omega_{mag}$. In order to illustrate this effect more concretely, we adopt a simple model for the dispersion of the pole. Namely,

we set $\nu_{res}(\mathbf{q}) = \Omega_{mag} + \alpha q^2$. Integrating in Eq. (3.21) over q and substituting the result into (3.19) we obtain

$$\chi_R(\Omega) = \frac{\Gamma_{tr}^2 a^2}{8\pi\alpha\Omega^2} \log \frac{4\Omega_{mag}^2}{4\Omega_{mag}^2 - \Omega^2}. \tag{3.23}$$

We see that in the two-loop approximation, $\mathrm{Im}\,\chi_R(\Omega)$ undergoes a jump from zero to a finite value at $\Omega = 2\Omega_{mag}$. The real part of the Raman susceptibility $\mathrm{Re}\,\chi_R(\Omega)$ diverges logarithmically at this frequency. Below we verify this result by evaluating (3.20) numerically.

We next follow the same path as in the normal state and include higher-order diagrams (Fig. 3.3) with the interactions between the two spin fluctuations, i.e., replace the two-loop result $\chi_R = \Gamma_{tr}^2 \chi^2(\Omega)$ by

$$\chi_R(\Omega) = \Gamma_{tr}^2 \chi_{I-nem}(\Omega) = \Gamma_{tr}^2 \frac{\chi^2(\Omega)}{1 + 2g\chi^2(\Omega)}. \tag{3.24}$$

Because Re χ^2 diverges upon approaching $2\Omega_{mag}$ from below, Im χ^2 vanishes below $2\Omega_{mag}$, and $g < 0$, the full $\mathrm{Im}\chi_R(\Omega)$ has a true pole at some frequency $\Omega = \Omega_{res,1} < 2\Omega_{mag}$.

We now verify the approximation that Γ_{tr} can be taken out of the integral over the bosonic frequency ν. The triangular vertex contains one internal frequency ω and two external ones: Ω, at which we probe the Raman response, and the bosonic frequency μ. For Ω we take the resonance frequency $\Omega_{res,1} < 2\Omega_{mag}$. Typical bosonic frequency $\nu \sim \Omega_{mag}$ and typical ω is Δ. Obviously then, the AL vertex Γ_{tr} is independent on ν if Ω_{mag} is much smaller than Δ, i.e., when internal energy in the AL diagram made out of three fermionic Green's functions is much larger than both external frequencies.

The condition $\Omega_{mag} \ll \Delta$ is satisfied when the inverse magnetic correlation length m_s is small enough because $\Omega_{mag} \propto m_s$ [106]. As we said in the Introduction, in Fe-based materials, where B_{1g} resonance has been observed, the situation is somewhat different: neutron scattering data for $NaFe_{1-x}Co_xAs$ with $x = 0.045$ show [107] that $\Omega_{mag} \approx 7$ meV, while $\Delta = 5 - 5.5$ meV [108], i.e. Δ is somewhat smaller. In this situation, there is no good reason to treat Γ_{tr} as a constant.

In the next section we analyze another scenario, which is justified in the opposite limit when Ω_{mag} is much larger than Δ.

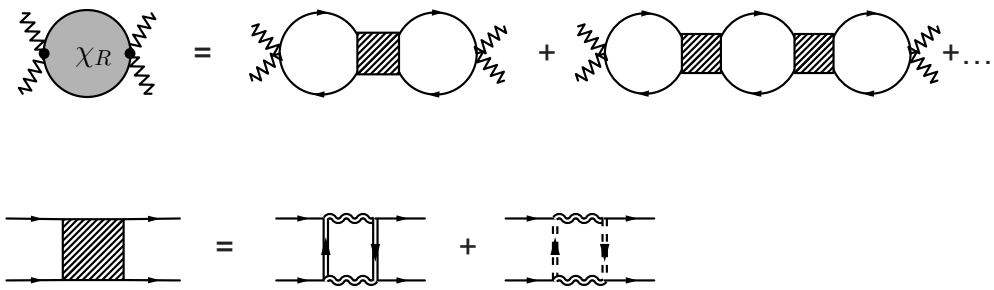

Figure 3.8: Reinterpretation of series of AL diagrams for χ_R with interactions between spin fluctuations as series consisting of multiple particle-hole bubbles with zero momentum and finite frequency transfer (unshaded circles), separated by effective interactions mediated by spin-fluctuations. Each interaction vertex (shaded rectangle) is the convolution of two fermionic and two bosonic propagators. A particular subset of diagrams is shown, with fermions from one of the hole band (solid lines). Double solid and double dashed lines describe fermions from two electron bands.

3.4.2 Another interpretation of AL contribution to the B_{1g} Raman response below T_c.

In this section we look at the second-order AL diagram from Fig. 3.2 through different lenses. Namely, we abandon the approximation in which Γ_{tr} is treated as a constant and instead use the fact that on both ends incoming and outgoing fermionic momenta are identical (either $\mathbf{k}$ or $\mathbf{p}$), while frequencies differ by Ω, and re-interpret this diagram as consisting of the product of two particle-hole polarization operators at zero transferred momentum and finite frequency, $\Pi_{B_{1g}}(\Omega)$ [the same as in Eq. (3.2)], separated by magnetically mediated effective interaction λ_{mag} (see Fig. 3.8). The latter is the convolution of two fermionic and two bosonic propagators. Viewed this way, the two-loop AL diagram has the same structure as the two-loop diagram from RPA series in Eq. (3.2). Accordingly, λ_{mag} and the bare λ are combined into $\lambda_{eff} = \lambda + \lambda_{mag}$. If the combined λ_{eff} is negative, $1+\lambda_{eff}\Pi_{B_{1g}}(\Omega)$ necessary vanishes at some frequency below 2Δ because Im $\Pi_{B_{1g}}(\Omega)$ vanishes below 2Δ and Re $\Pi_{B_{1g}}(\Omega)$ diverges as $1/\sqrt{4\Delta^2 - \Omega^2}$ when $|\Omega|$ approaches 2Δ from below. The vanishing of $1 + \lambda_{eff}\Pi_{B_{1g}}(\Omega)$ implies that Raman intensity has an excitonic resonance at $\Omega = \Omega_{res,2}$.

The representation of the two-loop AL diagram from Fig. 3.2 as $\lambda_{mag}\Pi^2_{B_{1g}}(\Omega)$ with

a constant λ_{mag} is again an approximation because the result for the convolution of two fermionic and two bosonic propagators generally depends on external momentum in frequency. The singular behavior of the particle-hole polarization bubble $\Pi_{B_{1g}}(\Omega)$ at $\Omega \approx 2\Delta$ comes from internal frequencies near $\pm\Delta$. Internal frequencies in the fermionic-bosonic loop for λ_{mag} are of order Ω_{mag}. If Ω_{mag} is much larger than Δ, a typical internal frequency is much larger than a typical external frequency. The latter can then be sent to zero, in which case λ_{mag} becomes a constant. The frequency $\Omega_{mag} < 2\Delta$ and hence it can be at most twice Δ. But number-wise this may be sufficient to treat λ_{mag} as a constant. The same distinction holds for internal/external momenta, and the result is that, to the same accuracy, λ_{eff} can be evaluated by placing external momenta on the Fermi surface.

We compute λ_{eff} first in the normal state and then in a superconductor, assuming formally that $\Omega_{mag} \gg \Delta$. To simplify calculations, we set $\mu = 0$, i.e., assume that the size of hole/electron pockets is infinitesimally small. The argument is that, if λ_{eff} has a definite sign in this limit, then, by continuity, the sign should remain the same at a small but finite μ.

In the normal state, the coupling λ_{mag} is given by

$$\lambda_{mag} = -g_{sf}^2 \int \frac{\mathrm{d}^2\mathbf{q}\mathrm{d}\nu}{(2\pi)^3} G^2(\mathbf{q},\nu)\left(\chi^s(\mathbf{q},\nu)\right)^2, \tag{3.25}$$

where ν is the Matsubara frequency. For definiteness, we take fermions from one of the electron bands, i.e., use $G(\mathbf{q},\nu) = 1/(i\nu - q^2/(2m))$. We verified that λ_{mag} does not change if we instead take fermions from the hole band. For the dynamical spin susceptibility we use Landau-overdamped form extended to Matsubara frequencies: $\chi(\mathrm{q},\nu) = 1/(q^2 + m_s^2 + |\nu|/\nu_0)$, where ν_0 is a positive constant.

Substituting the forms of bosonic and fermionic propagators into (3.25) we obtain

$$\begin{aligned}\lambda_{mag} &= -g_{sf}^2 \int \frac{\mathrm{d}^2\mathbf{q}\mathrm{d}\nu}{(2\pi)^3} \frac{1}{[i\nu - \mathbf{q}^2/(2m)]^2} \frac{1}{(\mathbf{q}^2 + m_s^2 + |\nu|/\nu_0)^2} \\ &= \frac{\nu_0^2 m}{(2\pi)^2} \int_0^\infty \mathrm{d}x \int_{-\infty}^\infty \mathrm{d}\nu \frac{1}{(\nu + ix)^2} \frac{1}{(|\nu| + \nu_0 m_s^2 + \nu_0 m x)^2}.\end{aligned} \tag{3.26}$$

The double pole in the fermionic Green's function is located at $\nu = -ix$. It is then convenient to evaluate the frequency integral by closing the integration contour over the upper half plane of complex ν (see Fig. 3.9). The integrand vanishes at $|\nu| \to \infty$,

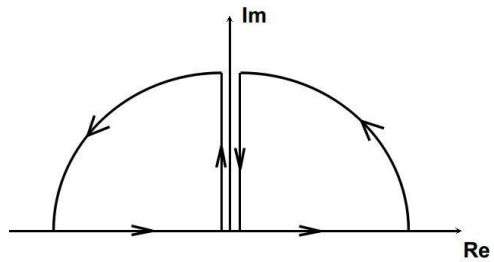

Figure 3.9: Contour of integration over frequency ν in Eq. 3.26.

and if χ^s was an analytic function of ν, λ_{mag} would be zero. But this is not the case because the Landau damping term contains $|\nu| = \sqrt{\nu^2}$, which is non-analytic function of ν along imaginary axis in both half planes. Choosing the integration contour as shown in Fig. 3.9 and using $|iz + \epsilon| = iz \operatorname{sgn} \epsilon$, we obtain after a simple algebra

$$\begin{aligned}\lambda_{mag} =& - ig_{sf}^2 \frac{\nu_0^2 m}{(2\pi)^2} \int_0^\infty \mathrm{d}x \int_0^\infty \mathrm{d}z \frac{1}{(z+x)^2} \\ & \times \left[\frac{1}{(iz + \nu_0 m_s^2 + \nu_0 m x)^2} - \frac{1}{(-iz + \nu_0 m_s^2 + \nu_0 m x)^2} \right] \\ =& - \frac{4 g_{sf}^2 \nu_0^2 m}{(2\pi)^2} \times \int_0^\infty \mathrm{d}x \int_0^\infty \mathrm{d}z \frac{z(\nu_0 m_s^2 + \nu_0 m x)}{(z+x)^2 [z^2 + \nu_0^2 (m_s^2 + mx)^2]^2}. \end{aligned} \tag{3.27}$$

The integrand is positive, hence $\lambda_{mag} < 0$. Estimating the integral, we obtain $\lambda_{mag} \propto 1/m_s^4$, i.e., λ_{mag} strongly increases near the magnetic instability.

In the superconducting state, we represent spin-fluctuation propagator by Eq. (3.18), i.e., by $\chi(\mathrm{q}, \nu) = a/[\nu^2 + \nu_{res}^2(\mathbf{q})]$, and use $\nu_{res}(\mathbf{q}) = \Omega_{mag} + \alpha q^2$. We assume and then verify that typical ν in the integral for λ_{mag} are of order Ω_{mag}. Because we assume $\Omega_{mag} \gg \Delta$, we can still use normal state Green's functions for fermions Substituting into (3.25) we obtain

$$\begin{aligned}\lambda_{mag} &= -g_{sf}^2 \int \frac{\mathrm{d}^2\mathbf{q}\mathrm{d}\nu}{(2\pi)^3} \frac{1}{[i\nu - \mathbf{q}^2/(2m)]^2} \frac{a}{[\nu^2 + (\Omega_{mag} + \alpha q^2)^2]^2} \\ &= \frac{g_{sf}^2}{4\pi^2} \frac{ma}{\Omega_{mag}^4} \int_0^\infty \mathrm{d}x \int_{-\infty}^\infty \mathrm{d}\nu \frac{1}{(\nu + ix)^2} \frac{1}{[\nu^2 + (1+\beta x)^2]^2}. \end{aligned} \tag{3.28}$$

where $\beta = 2m\alpha$ is a dimensionless parameter. The integrand, viewed as a function of ν, contains two double poles in the lower-half plane, at $\nu = -ix$ and at $\nu = -i(1+\beta x)$, and the double pole in the upper half-plane, at $\nu = i(1+\beta x)$. The last two double poles

come from χ^2. Evaluating the frequency integral by standard means, we obtain after simple algebra that

$$\lambda_{mag} = -\frac{g_{sf}^2}{8\pi}\frac{ma}{\Omega_{mag}^4}\int_0^\infty \mathrm{d}x \frac{3+x(1+3\beta)}{(1+\beta x)^3[1+(1+\beta)x]^3}. \tag{3.29}$$

The integrand is positive for all $x > 0$, hence $\lambda_{mag} < 0$, like in the normal state. Furthermore, because $\Omega_{mag} \propto m_s$, we still have $\lambda_{mag} \propto 1/m_s^4$.

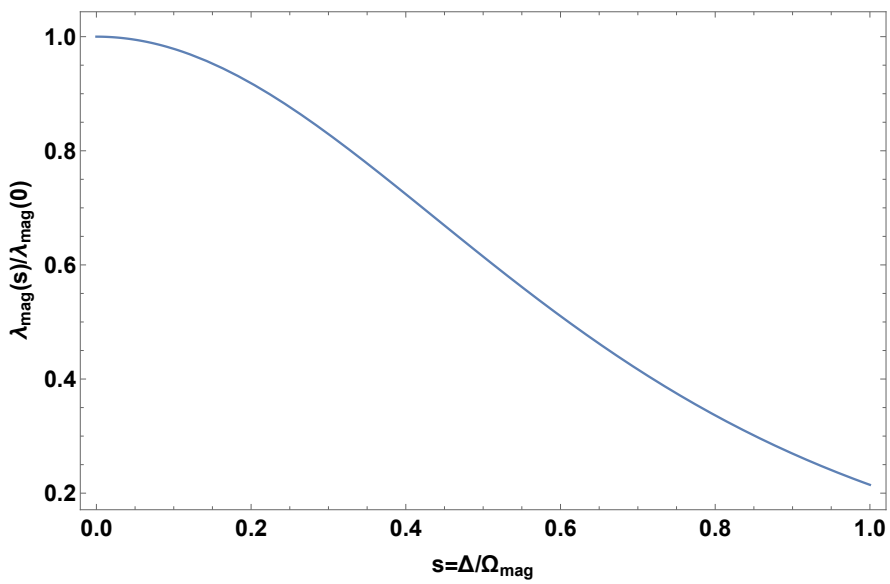

Figure 3.10: The dependence of the effective spin-mediated four-fermion interaction $\lambda_{mag}(s)$ on $s = \Delta/\Omega_{mag}$, see Eq. (3.30). We set $\beta = 1$ for definiteness.

Like we said, the condition $\Omega_{mag} \gg \Delta$ is not realized because $\Omega_{mag} \leq 2\Delta$. To estimate how λ_{mag} changes when Ω_{mag} and Δ become comparable, we use the fact that 2Δ singularity in the particle-hole bubble comes from fermions with frequencies near $\pm\Delta$ and evaluate λ_{mag} in the superconducting state for the case when the frequencies of the two bosonic propagators differ by $\Omega_m = 2\Delta$. The calculation is straightforward, and the result is that λ_{mag} becomes a function of $s = \Delta/\Omega_{mag}$. The dependence on s is given by

$$\begin{aligned}\lambda_{mag}(s) = &-\frac{g_{sf}^2}{8\pi}\frac{ma}{\Omega_{mag}^4} \\ &\times \int_0^\infty \mathrm{d}x \frac{[(1+(1+\beta)x][3+x(1+3\beta)] - s^2}{(1+\beta x)[(1+\beta x)^2+s^2]\{[1+(1+\beta)x]^2+s^2\}^2}\end{aligned} \tag{3.30}$$

We plot $\lambda_{mag}(s)$ in Fig. 3.10. We see that $\lambda_{mag}(s)$ drops when $s = \Delta/\Omega_{mag}$ increases, but the ratio $\lambda_{mag}(s)/\lambda_{mag}(0)$ remains of order one when Δ and Ω_{mag} become comparable.

Combining this last observation with the fact that $\lambda_{mag}(0) \propto 1/m_s^4$, we conclude that for small enough m_s, $|\lambda_{mag}|$ is definitely larger than the bare interaction λ, hence $\lambda_{eff} = \lambda + \lambda_{mag}$ is negative, no matter what is the sign of λ.

One can go a step further and add to the interaction vertex in Fig. 3.8 (the shaded rectangle) the renormalizations coming from fermions with energies higher than Ω_{mag}. These terms renormalize the convolution of two spin-fluctuation propagators $\chi^2(\Omega)$ into $\chi_{I-nem} = \chi^2/[1 + 2g\chi^2(\Omega)]$ and hence add the same denominator to λ_{mag}. As the consequence, λ_{mag} diverges already at the Ising-nematic instability, before m_s vanishes.

By continuity, we assume that λ_{mag} remains negative also for finite hole and electron pockets. Using further RPA form for the Raman intensity, Eq. (3.2), we obtain that $\chi_R(\Omega)$ has the singularity at $\Omega = \Omega_{res,2} < 2\Delta$, at which $1 + \lambda_{eff}\Pi_{B_{1g}}(\Omega) = 0$.

Finally, we briefly comment on the difference between our analysis and earlier phenomenological consideration of the bi-linear coupling between B_{1g} orbital order parameter $\Delta_{oo} = \sum_k < c_k^\dagger c_k \cos 2\theta_k >$ and $\Delta_1^2 - \Delta_2^2$, where Δ_1 and Δ_2 are spin-fluctuation fields with momenta near $\mathbf{Q}_1$ and $\mathbf{Q}_2$ [16, 97]. In the microscopic calculation [101] such term appears in the Landau free energy once we introduce $\Delta_{1,2}$ and Δ_{oo} as order parameter fields, bi-linear in fermions, and perform Hubbard-Stratonovich transformation from fermions to bosonic collective variables. The prefactor A for $\Delta_{oo}(\Delta_1^2 - \Delta_2^2)$ term in the Landau functional is given by the same triangular diagram as AL vertex, and has a finite value (i.e., $A \sim \Gamma_{tr}$). At the first glance, we can identify $\Delta_1^2 - \Delta_2^2$ with the propagator of an Ising-nematic field and obtain the correction to the prefactor for Δ_{oo}^2 in the form $-A^2\chi_{I-nem}$. Because the bare prefactor is $\Pi_{B_{1g}}^{-1} + \lambda$, $\lambda_{eff} = \lambda - A^2\chi_{I-nem}$. At the second glance, however, we note that the Landau functional in terms of Δ_1 and Δ_2 is not the same as Landau functional expressed in terms of the Ising-nematic field. To obtain the latter one has to do a second Hubbard-Stratonovich transformation to the composite Ising-nematic bosonic field Δ_{I-nem} and integrate over the primary fields Δ_1 and Δ_2. Only then one can extract the bi-linear coupling between orbital and Ising-nematic order parameters. Another way to see that $A^2\chi_{I-nem}$ with $A \sim \Gamma_{tr}$ is not the correction to λ is to notice that this expression is the full result for the Raman bubble

rather than for the effective interaction between fermions from the two particle-hole bubbles.

3.4.3 Comparative analysis of the two scenarios

Combining the results of the last two sections, we see that the resonance in $\chi_R(\Omega)$ holds independent of whether Ω_{mag} is larger or smaller than Δ, but the physics is different in the two cases. When Ω_{mag} is smaller than Δ, the resonance has purely magnetic origin and comes from the pole in χ_{I-nem} at $\Omega = \Omega_{res,1} \leq 2\Omega_{mag}$. For this resonance, the role of fermions is to provide some regular coupling, Γ_{tr}, between incoming and outgoing light and a pair of spin fluctuations with momenta near $\mathbf{Q}_1$ or $\mathbf{Q}_2$. When $\Omega_{mag} > \Delta$, the resonance comes from fermions and is due to singular behavior of particle-hole polarization bubble $\Pi_{B_{1g}}(\Omega)$ at $\Omega = 2\Delta$. The resonance occurs at a frequency $\Omega = \Omega_{res,2} \leq 2\Delta$. Spin fluctuations are again crucial, but now their role is to provide strong attractive interaction between fermions which make particle-hole bubbles.

We treated the two singularities in $\chi_R(\Omega)$ independent of each other chiefly to demonstrate that they come from two different pieces of physics. Such a treatment, however, is justified only if $\Omega_{res,1}$ and $\Omega_{res,2}$ are well separated. In our case, $\Omega_{res,1} \leq 2\Omega_{mag} < 4\Delta$, while $\Omega_{res,2} \leq 2\Delta$. How well $\Omega_{res,1}$ and $\Omega_{res,2}$ are separated then depends on the strength of various interactions and on the value of magnetic correlation length. Like we said, in FeSCs that we analyze, Ω_{mag} and Δ are not far from each other. In this case the resonance likely has a dual origin. In $NaFe_{1-x}Co_xAs$ with $x = 0.045$, the B_{1g} peak is seen at 7.1 meV, which is below both 2Δ and $2\Omega_{mag}$. This is consistent with the dual origin of the resonance.

3.4.4 Numerical evaluation of the AL diagrams

In this section we present the results of numerical evaluation of AL contributions to B_{1g} Raman intensity below T_c first in the two-loop approximation and then including the interaction between spin fluctuations. We first compute the AL vertex assuming that Γ_{tr} can be approximated by a constant and then present the results of the explicit calculation of the two-loop AL diagram for $\chi_R(\Omega)$.

The first step for numerical evaluation of χ_R is to calculate the time-ordered polarization function $\Pi_{s,ij}$ with fermions lines from bands i and j. The bare spin response can be obtained as a time-ordered average of spin operators over a non-interacting ground state. In the FeSCs, the response is largest near the nesting momenta $\mathbf{Q}_1 = (\pi, 0)$ or $\mathbf{Q}_2 = (0, \pi)$, which connect one hole pocket and one electron pocket. Since we are solely interested in evaluating the function near those momenta we will only consider band combinations of one hole and one electron pocket and drop the band indices from here on. We evaluate the function at momentum $\mathbf{Q} + \mathbf{q}$, where $\mathbf{Q}$ is either $\mathbf{Q}_1$ or $\mathbf{Q}_2$, whichever is appropriate.

For concreteness, we assume parabolic dispersions for the hole and electron pockets of the form $\xi_{\mathbf{k}} = \mu - \frac{k^2}{2m_h}$ and $\xi_{\mathbf{k}+\mathbf{Q}} = -\mu + \frac{k_x^2}{2m_x} + \frac{k_y^2}{2m_y}$, respectively. We evaluate all quantities in units of the gap Δ and for numerical parameters we choose $\mu = 2\Delta$, $m_h \approx 0.056\Delta^{-1}$ ($k_F = 0.15\pi/a$), $m_x = m_h/1.27$, and $m_y = m_x/0.3787$. These values approximately fit the bands and Fermi surfaces reported in ARPES measurements [115] of $NaFe_{1-x}Co_xAs$ for $x = 0.05$ (of the two hole bands, we fitted the one with the largest Fermi surface). For numerical convergence we included a finite broadening $\eta = \Delta/100$.

The general behavior of Π_s can be seen in Figs. 3.11 and 3.12. The first one shows a frequency sweep of the real part at $\mathbf{q} = 0$ and the divergence at 2Δ is clearly seen. The imaginary part (not shown) vanishes as $\eta \to 0$. This behavior holds unless $\mathbf{q}$ is so large that the normal-state FSs no longer intersect due to the shift. The second plot shows an example of the $\mathbf{q}$ dependence at $\nu = 0$. Although the function is anisotropic due to the eccentricity of the electron Fermi surface, the qualitative behavior is the same regardless of the polar angle. It is particularly important to emphasize that the function decreases monotonically with increasing $|\mathbf{q}|$.

In the numerical analysis, it is easier to deal with the effective interaction in the spin channel U_{eff} rather than the spin susceptibility. In the RPA

$$U_{eff}(\mathbf{Q} + \mathbf{q}, \nu) = \frac{u}{2} \frac{1}{1 - u\Pi_s(\mathbf{Q} + \mathbf{q}, \nu)}, \tag{3.31}$$

where $u > 0$ is the bare fermion-fermion interaction ($= U$ in the Hubbard model). The effective interaction is related to the spin susceptibility by $U_{eff}(\mathbf{Q} + \mathbf{q}, \nu) = [u + u^2\chi^s(\mathbf{Q} + \mathbf{q}, \nu)]/2$, so the two functions have the same pole structure and differ only by a constant shift u, which near a magnetic instability is small compared to the second

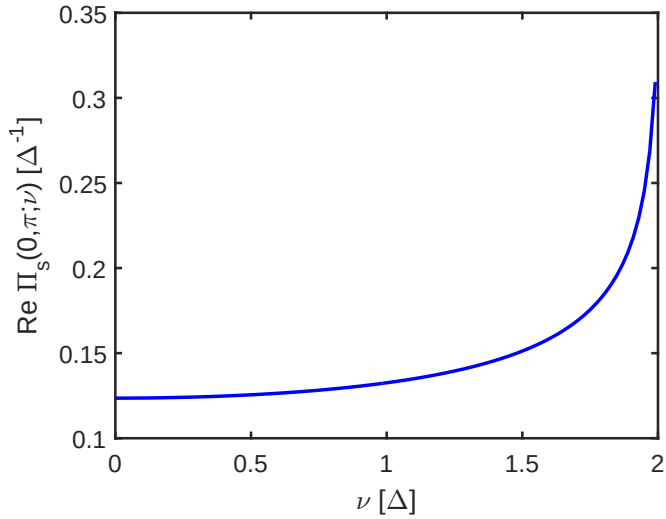

Figure 3.11: Frequency dependence of the bare spin polarization operator with momentum $(0, \pi)$.

term. The $u^2/2$ factor in front of χ^s is the same factor as in (3.9).

Figure 3.13 shows U_{eff} at $\mathbf{q} = 0$ as a function of ν. The real part diverges at the resonance frequency while the imaginary part has a sharp peak which in the limit of $\eta \to 0$ becomes a δ function. For the numerical calculations we have set $u \approx 7.9\Delta$, which determines $\Omega_{mag} \approx 0.6\Delta$.

Now we are ready to evaluate the Raman response (3.20). By using the spectral representation, the imaginary part of the response function can be equivalently calculated as

$$\begin{aligned} \operatorname{Im} \chi_R(\Omega) \propto \int \frac{\mathrm{d}^2\mathbf{q}}{(2\pi)^2} \int_0^\Omega \frac{\mathrm{d}\nu}{\pi} \operatorname{Im} U_{eff}(\mathbf{Q}+\mathbf{q}, \nu) \\ \times \operatorname{Im} U_{eff}(\mathbf{Q}+\mathbf{q}, \nu - \Omega). \end{aligned} \tag{3.32}$$

The advantage of this form is that it only requires knowledge of the function in a finite range of ν. The real part can then be calculated by using the Kramers-Kronig transformation.

Because $\operatorname{Im} U_{eff}(\mathbf{Q}+\mathbf{q}, \nu)$ is peaked at the resonant frequencies corresponding to each momentum $\mathbf{q}$, $\operatorname{Im} \chi_R(\Omega)$ can be seen as a convolution of many of these peaks. The result of the computation is shown in Fig. 3.14. We see that the imaginary part starts

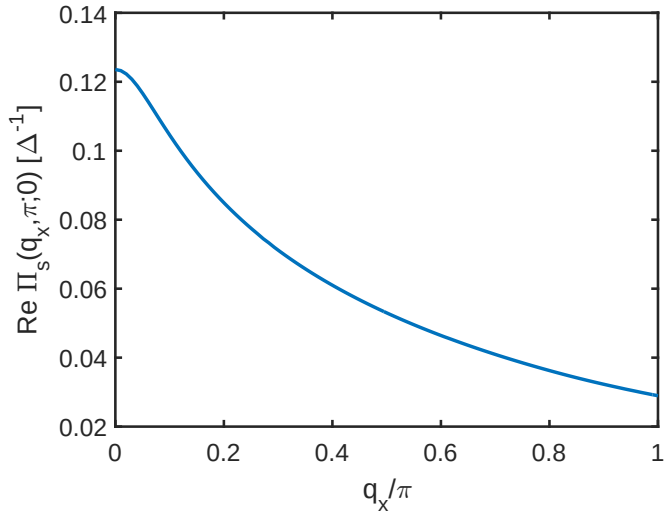

Figure 3.12: Momentum dependence of the static spin polarization operator with momentum near $(0, \pi)$. We have chosen momenta to be $\mathbf{q} + (0, \pi)$. The dependence on q_x is shown. The dependence on the polar angle of $\mathbf{q}$ is nonzero but rather weak.

small and undergoes a jump at $\nu \approx 1.2\Delta = 2\Omega_{mag}$, (compare to Fig. 3.13). Its value at higher frequencies comes from contributions from $\mathbf{q} \neq 0$, corresponding to excitons of higher energies. This jump is not sharp in the numerical calculations because of the finite value of η in (3.17).

We next consider the effect of the finite state interaction, i.e., include higher order diagrams (Fig. 3.3) with the interactions between the two spin fluctuations. In the approximation where the interactions between pairs of spin fluctuations with momenta near $\mathbf{Q}_1$ and/or $\mathbf{Q}_2$ can be treated as constants, we use Eq. (3.24) We plot the RPA form of $\chi_R(\Omega)$ in Fig. 3.15. We clearly see that $\mathrm{Im}\,\chi_R^0(\Omega)$ has a sharp peak at a frequency $\Omega < 2\Omega_{mag}$, which is below 2Δ.

3.5 Triangular fermion loop and symmetry channels

So far, we have neglected the details of the Raman vertex Γ_{tr} and thus the analysis above applies equally to all symmetry channels. We remind that in the experiments the resonance has been observed in the B_{1g} channel in the 1-Fe unit cell, but no resonance has been observed in the B_{2g} or A_{1g} channels. To address the origin of the difference

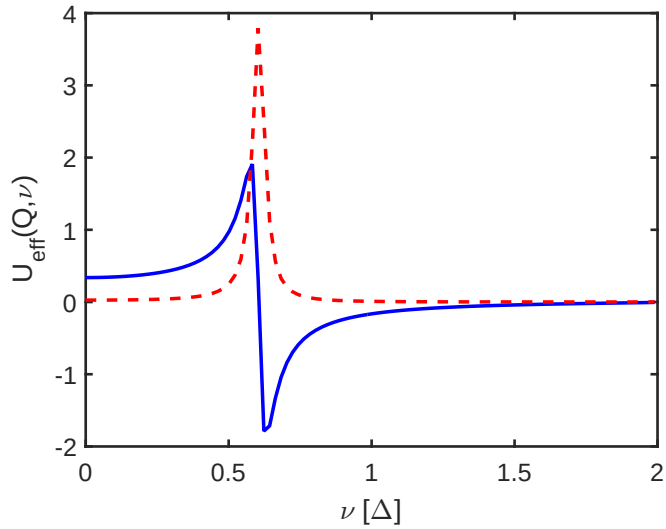

Figure 3.13: Frequency dependence of the real (solid blue line) and imaginary (dashed red line) parts of the effective interaction (in arbitrary units).

between Raman scattering in different symmetry channels, we consider the symmetry properties of the function $\Gamma_{tr}(\mathbf{q},\nu)$, defined in (3.7).

First we focus on the bare Raman vertices. The original Raman vertex $\gamma_i(\mathbf{k})$ between incoming and outgoing light and incoming and outgoing fermions from band i belongs to the irreducible representations of the point group D_{4h}. As a reminder, we point out that in the B_{1g} and B_{2g} representations, the function $\gamma_i(\mathbf{k})$ transforms under the point group operations as $k_x^2 - k_y^2$ and $k_x k_y$, respectively, while in the A_{1g} representation $\gamma_i(\mathbf{k})$ is invariant under the point group operations. We will consider each of these channels separately.

In the B_{1g} channel, the Raman response is directly coupled to nematic orbital fluctuations and in the orbital basis we can define it as

$$\chi_R(\Omega) = -i \int \mathrm{d}t e^{i\Omega t} \langle T \rho_n(t) \rho_n(0) \rangle, \tag{3.33}$$

where the nematic "density" operator is defined as $\rho_n = \frac{1}{\sqrt{N}} \sum_{\mathbf{k},\sigma} \left[a^\dagger_{\mathbf{k}\sigma} a_{\mathbf{k}\sigma} - b^\dagger_{\mathbf{k}\sigma} b_{\mathbf{k}\sigma} \right]$. In this notation, the fermion operators a and b correspond to the d_{xz} and d_{yz} orbitals, respectively.

The transformation from the orbital to the band basis in the case of the hole pockets

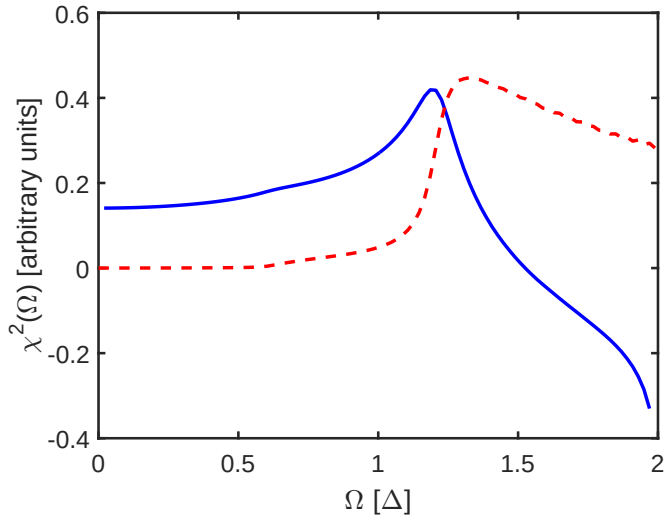

Figure 3.14: Contribution to Raman response from spin fluctuations. The solid blue and dashed red lines indicate the real and imaginary parts, respectively.

can be approximated by [125]

$$\begin{aligned}\alpha_{\mathbf{k}\sigma} &= \cos\theta_{\mathbf{k}} a_{\mathbf{k}\sigma} - \sin\theta_{\mathbf{k}} b_{\mathbf{k}\sigma},\\ \beta_{\mathbf{k}\sigma} &= \sin\theta_{\mathbf{k}} a_{\mathbf{k}\sigma} + \cos\theta_{\mathbf{k}} b_{\mathbf{k}\sigma},\end{aligned} \tag{3.34}$$

where α and β are denote the hole bands and θ is the angle along the Fermi surface.

The contribution to the nematic density operator from fermions from the hole bands then becomes

$$\begin{aligned}\rho_n = &\sum_{\mathbf{k}} (\alpha^\dagger_{\mathbf{k}\sigma}\alpha_{\mathbf{k}\sigma} - \beta^\dagger_{\mathbf{k}\sigma}\beta_{\mathbf{k}\sigma}) \cos 2\theta_{\mathbf{k}}\\ &+ \sum_{\mathbf{k}} (\alpha^\dagger_{\mathbf{k}\sigma}\beta_{\mathbf{k}\sigma} + \beta^\dagger_{\mathbf{k}\sigma}\alpha_{\mathbf{k}\sigma}) \sin 2\theta_{\mathbf{k}}.\end{aligned} \tag{3.35}$$

The second term can be neglected at low energies because it couples fermions from different Fermi surfaces, which do not cross. Substituting into (3.33) we find that the vertex function for holes $\gamma_i(\mathbf{k})$ in the B_{1g} channel is $\cos(2\theta_{\mathbf{k}})$ and has opposite signs for the two hole bands. For electron pockets, the situation is more simple since each electron pocket only has contributions from the d_{zx} or d_{yz} orbital, but not from both. The transformation from the orbital to the band basis is trivial and we find that

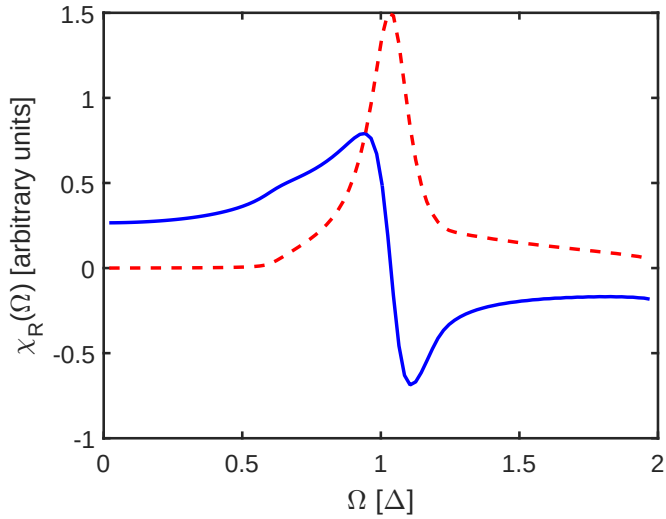

Figure 3.15: The full Raman susceptibility, which includes interactions between spin fluctuations. The solid blue line indicates the real part and the dashed red line the imaginary part of the function. We set $g = 1.66$.

$\gamma_i(\mathbf{k}) = \pm 1$, where the plus sign is for the electrons from the pocket near $\mathbf{Q}_1 = (\pi, 0)$ and the minus sign for electrons near $\mathbf{Q}_2 = (0, \pi)$.

For the B_{2g} channel one can define a different density operator

$$\rho_{B2g} = \frac{1}{\sqrt{N}} \sum_{\mathbf{k},\sigma} \left[a^\dagger_{\mathbf{k}\sigma} b_{\mathbf{k}\sigma} + b^\dagger_{\mathbf{k}\sigma} a_{\mathbf{k}\sigma} \right]. \tag{3.36}$$

Then using again the transformation (3.34) one finds that for hole bands the appropriate B_{2g} symmetry factor is $\gamma_i(\mathbf{k}) = \pm \sin(2\theta_{\mathbf{k}})$. For electron bands the symmetry factor is instead $\gamma_i(\mathbf{k}) = 0$ since the electron bands do not cross.

Finally, the Raman vertex in the A_{1g} channel is a constant along hole or electron pockets. In general, there are two possibilities: The symmetry factor can have the same sign for the coupling of light to electrons and holes, or change sign when switching between electrons and holes. In order to consider both possibilities we define two separate functions γ^{++}_{A1g} and γ^{+-}_{A1g}, referring to the cases with equal and opposite signs, respectively.

An additional effect of the orbital to band transformation (3.34) is that the factors of sine and cosine contribute extra angular dependence to the momentum integration in

Diagram	γ_{B1g}	γ_{B2g}	γ^{++}_{A1g}	γ^{+-}_{A1g}
Fig. 3.16(a)	$\cos 2\theta$	$\sin 2\theta$	1	1
Fig. 3.16(b)	$-\cos 2\theta$	$-\sin 2\theta$	1	1
Fig. 3.16(c)	1	0	1	-1
Fig. 3.16(d)	1	0	1	-1
Fig. 3.16(e)	$\cos 2\theta$	$\sin 2\theta$	1	1
Fig. 3.16(f)	$-\cos 2\theta$	$-\sin 2\theta$	1	1
Fig. 3.16(g)	-1	0	1	-1
Fig. 3.16(h)	-1	0	1	-1

Table 3.1: Symmetry factors for Raman vertices in different symmetry channels. We include two different representations of A_{1g} symmetry: One where the sign changes between hole and electron pockets, and one in which it does not (see text).

Λ. This is summarized graphically in Fig. 3.16, where we list the different band combinations with the appropriate signs and angular dependences. The symmetry factor $\gamma(\mathbf{k})$ for each diagram in different symmetry channels is given in Table 3.1. The first four diagrams [Figs. 3.16(a)-(d)]are for the interaction between light and spin fluctuations with momentum near $\mathbf{Q}_1$ and the other four are for momentum near $\mathbf{Q}_2$. The total contribution to Λ in each case is given by the sum of the four diagrams. The angular dependencies listed in the figure are for a model with only intra-orbital Hubbard interaction.

The result of the momentum integration is different depending on the symmetry channel. For simplicity in the evaluation of the integral, we consider identical circular Fermi surfaces in all bands and evaluate the bare triangular vertices $\Gamma^0_{tr}(\mathbf{q},\nu)$ in various geometries at $\mathbf{q}=0$. This particular value of $\mathbf{q}$ is important because the enhancement in $\chi^2(\Omega)$ at $\Omega=\Omega_{mag}$ comes primarily from momenta near $\mathbf{q}=0$. Considering only the angular part of the integration, we find that

$$\Gamma^{0,B_{1g}}_{tr} \propto \int \mathrm{d}\theta_{\mathbf{k}}(\cos 2\theta_{\mathbf{k}}\cos 2\theta_{\mathbf{k}} - 1) \neq 0 \tag{3.37}$$

$$\Gamma^{0,B_{2g}}_{tr} \propto \int \mathrm{d}\theta_{\mathbf{k}}\sin 2\theta_{\mathbf{k}}\cos 2\theta_{\mathbf{k}} = 0 \tag{3.38}$$

$$\Gamma^{0,++}_{tr} \propto \int \mathrm{d}\theta_{\mathbf{k}}(1-1) = 0 \tag{3.39}$$

$$\Gamma^{0,+-}_{tr} \propto \int \mathrm{d}\theta_{\mathbf{k}}(1+1) \neq 0 \tag{3.40}$$

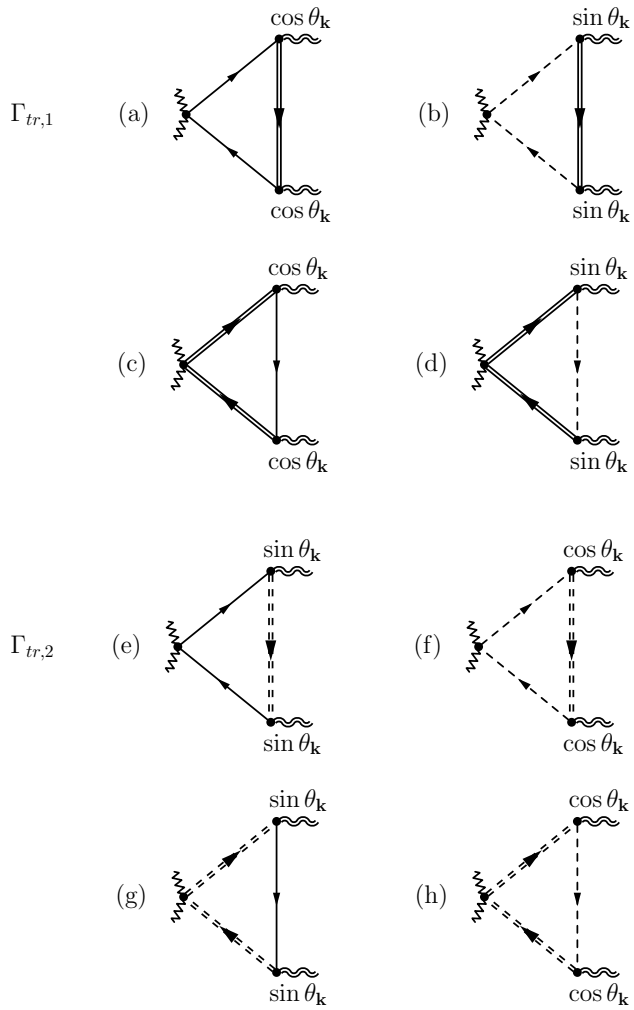

Figure 3.16: Contributions to the triangular fermion loop from different bands. The single solid and dashed lines represent the hole bands α and β, respectively, while the double solid and dashed lines represent electron bands centered at momentum $\mathbf{Q}_1$ and $\mathbf{Q}_2$, respectively. The factors of $\cos\theta$ and $\sin\theta$ arise from the transformation from the orbital to the band basis (see text).

where, we remind, $\Gamma_{tr}^{0,++}$ and $\Gamma_{tr}^{0,+-}$ are two different triangular vertices in A_{1g} channel. We see that $\Gamma_{tr}^{0,B_{2g}}$ and $\Gamma_{tr}^{0,++}$ vanish, i.e., there is no enhancement of the Raman intensity in the B_{2g} or A_{1g}^{++} channels, in agreement with the data.

One fine point in the calculation is that the contribution from diagrams with electron bands at the vertex has an additional minus sign compared to diagrams with hole bands at the vertex [for example, compare diagrams Figs. 3.16(c) and (d) with Figs. 3.16(a) and (b)]. This is not a symmetry factor but instead comes from the opposite signs between the hole and electron band dispersions and can be obtained after performing the frequency integration in the fermion loop. In the sign-preserving A_{1g} channel this leads to a complete cancellation while in the B_{1g} channel it is only partial since, e.g., Figs. 3.16(a) and (b) contribute a factor of $\cos 2\theta$ while Figs. 3.16(c) and (d) contribute a factor of $-\frac{1}{2}\cos 2\theta$.

To summarize, we have shown so far that the bare vertices for the B_{2g} and sign-preserving A_{1g} channels vanish and thus cannot lead to resonances. The bare vertices in B_{1g} and sign-changing A_{1g} channels are nonzero. Note that the Raman response in the sign-changing A_{1g} channel is not screened out by long-range component of Coulomb interaction [80, 81]. The response in the sign-preserving A_{1g} channel is screened [87, 88, 89], but in our case it vanishes anyway.

The next step is to include interactions between the spin fluctuations and calculate the renormalized vertices $\Gamma_{tr}^{B_{1g}}$ and Γ_{tr}^{+-}.

For this we first introduce vertices $\Gamma_{tr,1}$ and $\Gamma_{tr,2}$, which couple light to spin fluctuations with momentum near $\mathbf{Q}_1$ and $\mathbf{Q}_2$, respectively. The vertices in B_{1g} and A_{1g} channels are related to $\Gamma_{tr,1}$ and $\Gamma_{tr,2}$ as

$$\Gamma_{tr,1} = \Gamma_{tr}^{B_{1g}} + \Gamma_{tr}^{+-}, \quad \Gamma_{tr,2} = \Gamma_{tr}^{+-} - \Gamma_{tr}^{B_{1g}} \tag{3.41}$$

We then follow Ref. [101] and model the interaction between spin fluctuations as given by the effective action

$$\begin{aligned} S_{eff} = r_0(\Delta_1^2 + \Delta_2^2) + \frac{\kappa}{2}(\Delta_1^2 + \Delta_2^2)^2 \\ + \frac{g}{2}(\Delta_1^2 - \Delta_2^2)^2, \end{aligned} \tag{3.42}$$

where Δ_1 and Δ_2 are three-component spin fluctuation fields, respectively, in which each component corresponds to a direction in real space. The 1 and 2 subscripts distinguish

between fluctuations near $\mathbf{Q}_1$ and $\mathbf{Q}_2$. This effective action can obtained by introducing Hubbard-Stratonovich fields and then integrating out fermions. The result is [101] that $\kappa > 0$, but g is negative, at least at small dopings.

The bare vertices $\Gamma^0_{tr,1}$ and $\Gamma^0_{tr,2}$ are given by the sum of diagrams Figs. 3.16(a)-(d) and Figs. 3.16(e)-(h), respectively. In the ladder approximation, the coupled equations for the renormalized vertices $\Gamma_{tr,1}$ and $\Gamma_{tr,2}$ are given by

$$\Gamma_{tr,1} = \Gamma^0_{tr,1} - (\kappa + g)\Gamma_{tr,1}\chi^2 - (\kappa - g)\Gamma_{tr,2}\chi^2, \tag{3.43}$$

$$\Gamma_{tr,2} = \Gamma^0_{tr,2} - (\kappa + g)\Gamma_{tr,2}\chi^2 - (\kappa - g)\Gamma_{tr,1}\chi^2, \tag{3.44}$$

where we remind that χ^2 is the shorthand notation for $\int \frac{\mathrm{d}^2\mathbf{q}\mathrm{d}\nu}{(2\pi)^3}\chi^{\mathrm{s}}(\mathbf{Q}+\mathbf{q},\nu)\chi^{\mathrm{s}}(\mathbf{Q}+\mathbf{q},\nu+\Omega)$. In this expression we do not distinguish between $\mathbf{Q}_1$ and $\mathbf{Q}_2$ because by symmetry the result of the integration is the same.

These coupled equations can be solved in terms of $\Gamma^{B_{1g}}_{tr}$ and Γ^{+-}_{tr}:

$$\Gamma^{+-}_{tr} = \frac{\Gamma^{0,+-}_{tr}}{1 + 2\kappa\chi^2}, \tag{3.45}$$

$$\Gamma^{B_{1g}}_{tr} = \frac{\Gamma^{0,B_{1g}}_{tr}}{1 + 2g\chi^2}. \tag{3.46}$$

The renormalized Raman susceptibility is then given by

$$\chi^{B_{1g}}_R = \frac{(\Gamma^{0,B_{1g}}_{tr})^2\chi^2}{1 + 2g\chi^2}, \tag{3.47}$$

$$\chi^{A1g,+-}_R = \frac{(\Gamma^{0,+-}_{tr})^2\chi^2}{1 + 2\kappa\chi^2}. \tag{3.48}$$

Since $\kappa > 0$ and $g < 0$, only the B_{1g} channel has a resonance, which is consistent with the data. There is no resonance-type enhancement from the coupling to spin fluctuations, regardless of whether the sign-preserving or sign-changing representation is involved. We note in passing that there is a different enhancement of the Raman intensity in the A_{1g} channel in s^{+-} superconductors due to a direct process in which a light generates a ladder series of particle-hole pairs [80].

We also note that the downward renormalization of Γ^{+-}_{tr} by $1/(1+2\kappa\chi^2)$ also strongly reduces the temperature dependence of the A_{1g} Raman intensity in the normal state.

Indeed, explicit calculation shows [101] that $\kappa \sim 1/T^2$. Following the considerations of Sec. 3.3, we find that in the normal state

$$\chi_R^{A1g}(T) \sim \frac{(m_s)^{-2}}{T + T_1}, \tag{3.49}$$

where $T_1 \gg T_0$ because $\kappa \gg |g|$. This implies that at $T \geq T_0$, $\chi_R^{A1g}(T)$ is nearly flat.

3.6 Orbital fluctuations

In this section we consider the coupling of the Raman response to orbital fluctuations in detail and show that the interaction in the d-wave channel is repulsive and cannot lead to the observed resonance.

As explained in the Introduction, the electronic structure of $NaFe_{1-x}Co_xAs$ and $Ba(Fe_{1-x}Co_x)_2As_2$ consists of four bands that cross the Fermi energy. We will refer to the two hole bands centered at $(0,0)$ as α and β and to the electron bands centered at $(\pi,0)$ and $(0,\pi)$ as η and δ, respectively. We organize our analysis in the language of vertex renormalization. We start with a set of bare Raman vertices $\gamma_i(\mathbf{k})$ with both external fermion lines belonging to the i-th band, then dress each vertex with interactions to obtain the full vertex $\Gamma_i(\mathbf{k})$. Here the index runs over the set of bands $\{\alpha, \beta, \eta, \delta\}$. Since we are interested in computing the Raman response in the limit of vanishingly small external momentum, we do not consider vertices with external fermion lines from two different bands since in the absence of band crossings there will be no low-energy contribution from these vertices.

For simplicity we study a model consisting of only d_{xz} and d_{yz} orbitals. Since the remaining d_{xy} orbital has A_{1g} symmetry it cannot directly contribute to the Raman response in the B_{1g} channel. The transformation between the band and orbital basis for the hole pockets was given in (3.34). For the electron pockets we will simply set $\eta_{\mathbf{k}+\mathbf{Q}_1} = a_{\mathbf{k}+\mathbf{Q}_1}$ and $\delta_{\mathbf{k}+\mathbf{Q}_2} = b_{\mathbf{k}+\mathbf{Q}_2}$. Following the reasoning in Sec. 3.5, the bare B_{1g} Raman vertex is given by $\gamma_i(\mathbf{k}) = \{\cos 2\theta_{\mathbf{k}}, -\cos 2\theta_{\mathbf{k}}, 1, -1\}_i$. The alternating signs reflect the difference between d_{xz} and d_{yz} contributions.

For our perturbative analysis, we assume that the short-range intra-orbital repulsion is the dominant interaction. Thus, the interaction Hamiltonian in the orbital basis is

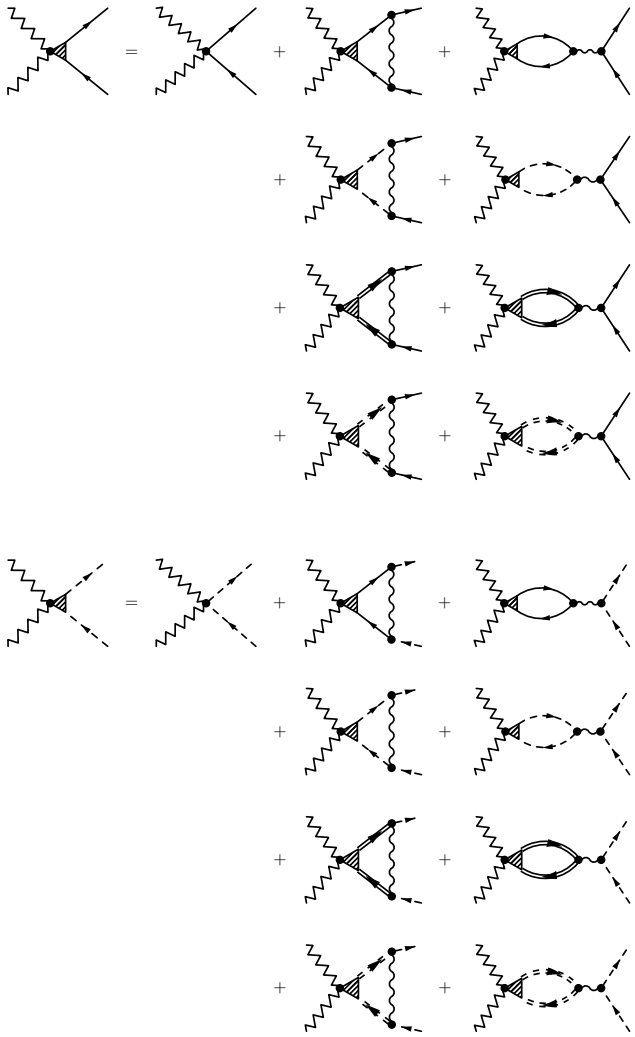

Figure 3.17: Vertex renormalization for hole bands α and β. The single solid and dashed lines represent excitations from hole bands α and β, respectively, and the double solid and dashed lines from electron bands η and δ, respectively.

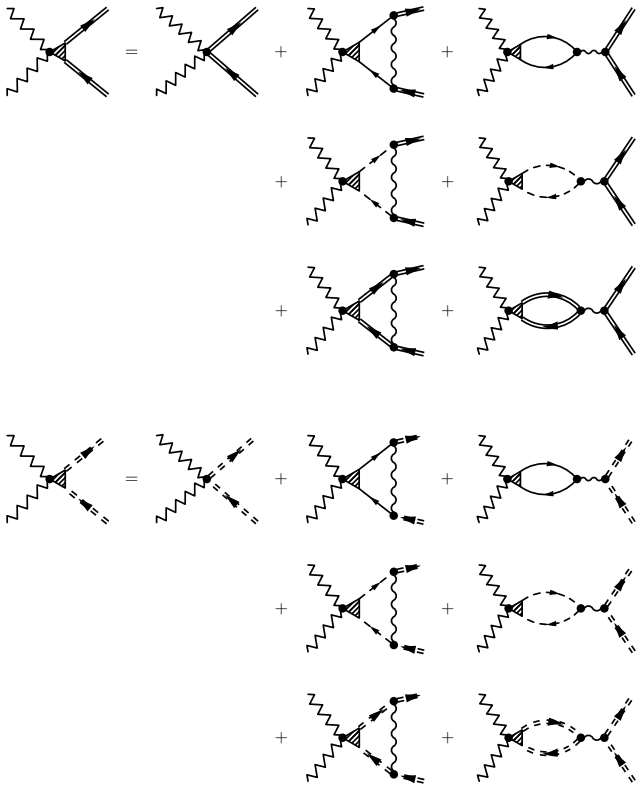

Figure 3.18: Vertex renormalization for electron bands η and δ. The notations are the same as in Fig. 3.17.

given by

$$\mathcal{H}_I = U \sum_{\mathbf{q}} \left[\rho_{xz}(\mathbf{q})\rho_{xz}(-\mathbf{q}) + \rho_{yz}(\mathbf{q})\rho_{yz}(-\mathbf{q})\right], \tag{3.50}$$

where $\rho_{xz}(\mathbf{q}) = \frac{1}{\sqrt{N}} \sum_{\mathbf{k},\sigma} a^\dagger_{\mathbf{k}+\mathbf{q}\sigma} a_{\mathbf{k}\sigma}$ and $\rho_{yz}(\mathbf{q}) = \frac{1}{\sqrt{N}} \sum_{\mathbf{k},\sigma} b^\dagger_{\mathbf{k}+\mathbf{q}\sigma} b_{\mathbf{k}\sigma}$ are the density operators of the d_{xz} and d_{yz} orbitals, respectively.

Our diagrammatic analysis is summarized in Figs. 3.17 and 3.18. For notational convenience we define auxiliary functions $\tilde{\Gamma}_i(\mathbf{k})$ and $\tilde{\gamma}_i(\mathbf{k})$ such that

$$\Gamma_i = \left(\tilde{\Gamma}_\alpha \cos 2\theta_{\mathbf{k}}, \tilde{\Gamma}_\beta \cos 2\theta_{\mathbf{k}}, \tilde{\Gamma}_\eta, \tilde{\Gamma}_\delta\right)_i \tag{3.51}$$

and a similar expression for γ_i. The set of coupled equations for the Raman vertices can be written in matrix form as

$$\tilde{\mathbf{\Gamma}} = \tilde{\gamma} - \mathbf{V}\mathbf{\Pi}\tilde{\gamma}, \tag{3.52}$$

where $\mathbf{V}$ and $\mathbf{\Pi}$ are interaction and polarization matrices, respectively, given by

$$\mathbf{V} = \frac{U}{2} \begin{pmatrix} 1 & -1 & 1 & -1 \\ -1 & 1 & -1 & 1 \\ 1 & -1 & 2 & 0 \\ -1 & 1 & 0 & 2 \end{pmatrix} \tag{3.53}$$

$$\mathbf{\Pi} = \begin{pmatrix} \Pi_\alpha(0,\Omega) & 0 & 0 & 0 \\ 0 & \Pi_\beta(0,\Omega) & 0 & 0 \\ 0 & 0 & \Pi_\eta(0,\Omega) & 0 \\ 0 & 0 & 0 & \Pi_\delta(0,\Omega) \end{pmatrix} \tag{3.54}$$

In this notation, the polarization functions are defined as

$$\begin{aligned} \Pi_i(0,\Omega) =& i \int \frac{\mathrm{d}^2 k \mathrm{d}\nu}{(2\pi)^3} s_i(\mathbf{k}) \left[G_i(\mathbf{k},\nu+\Omega)G_i(\mathbf{k},\nu)\right. \\ & \left. - F_i(\mathbf{k},\nu+\Omega)F_i(\mathbf{k},\nu)\right], \end{aligned} \tag{3.55}$$

where G_i and F_i are normal and anomalous Green's functions for band i, respectively, and $s_i(\mathbf{k}) = \{\cos^2(2\theta_{\mathbf{k}}), \cos^2(2\theta_{\mathbf{k}}), 1, 1\}_i$. We note that by symmetry $\Pi_\eta(0,\Omega) = \Pi_\delta(0,\Omega)$. In this definition, the real part of each function is positive.

The solution to (3.52) is easily obtained as $\tilde{\mathbf{\Gamma}} = (\mathbb{I} + \mathbf{V\Pi})^{-1}\tilde{\gamma}$, where $\mathbb{I}$ is the identity matrix. After evaluation of the matrix multiplication we find that the full vertex is given by

$$\Gamma_i = \left[1 + \frac{U}{2}\sum_j \Pi_j(0,\Omega)\right]^{-1} \gamma_i \tag{3.56}$$

and the full response function takes the simple form

$$\chi_R(\Omega) = \frac{2\sum_i \Pi_i(0,\Omega)}{1 + \lambda \sum_j \Pi_j(0,\Omega)}, \tag{3.57}$$

where $\lambda = U/2 > 0$. This is the same formula as Eq. (2) [with $\Pi_{B_{1g}}(\Omega) = \sum_j \Pi_j(0,\Omega)$]. Obviously, for $\lambda > 0$ the Raman susceptibility $\chi_R(\Omega)$ contains no poles and thus orbital fluctuations alone cannot explain the observed resonance in $\chi_R(\Omega)$.

3.7 Summary

In this work we argued that the coupling of the Raman vertex to pairs of magnetic fluctuations via the AL process can explain the $1/(T - T_0)$ behavior of the B_{1g} Raman intensity in the normal state of $NaFe_{1-x}Co_xAs$, $Ba(Fe_{1-x}Co_x)_2As_2$, $EuFe_2As_2$, and $SrFe_2As_2$, and the development of the resonance below T_c, observed in the first two.

We considered the AL process in which light couples to a particle-hole pair, which then gets converted into a pair of spin fluctuations with momenta near $\mathbf{Q}_1 = (\pi, 0)$ and $\mathbf{Q}_2 = (0, \pi)$. We analyzed magnetically mediated Raman intensity both analytically and numerically, first at the leading two-loop order and then included interactions between pairs of magnetic fluctuations. We demonstrated explicitly that the full Raman intensity in the B_{1g} channel can be viewed as the result of the coupling of light to Ising-nematic susceptibility via Aslamazov-Larkin process. We argued that the $1/(T - T_0)$ temperature dependence in the normal state is the combination of the temperature dependencies of the Aslamazov-Larkin vertex and of Ising-nematic susceptibility. We further argued that the resonance in the B_{1g} channel below T_c emerges because of two effects. One is the development of a pole in the fully renormalized Ising-nematic susceptibility. The pole occurs at a frequency $\Omega_{res,1} < 2\Omega_{mag}$, where Ω_{mag} is the minimal frequency of a dispersing spin resonance at momenta near $Q_{1,2}$ in an s^{+-} superconductor. Another effect is that spin fluctuations generate attractive interactions between

low-energy fermions, which constitute particle-hole bubbles with zero momentum transfer. An attractive interaction between such fermions combined with the fact that in an s-wave superconductor a particle-hole bubble at zero momentum transfer is singular at 2Δ gives rise to an excitonic resonance at $\Omega_{res,2} < 2\Delta$. In FeSCs $\Omega_{res,1}$ and $\Omega_{res,2}$ are not far from each other, and the observed strong peak in B_{1g} Raman intensity below T_c is likely the mixture of both effects.

Chapter 4

Time-Reversal Symmetry Breaking Superconductivity in the Coexistence Phase with Magnetism

4.1 Introduction

As mentioned in Chapter 1, the rich phase diagram of the FeSCs (Fig. 1.2) includes the regions of superconductivity (SC), spin density wave (SDW), nematic order, and a region where SDW, SC, and nematic order coexist [92, 126, 127, 128]. Outside the SDW/nematic region, SC develops in the spin-singlet channel and in most of Fe-based superconductors it has $s-$wave symmetry with a π phase shift between the SC order parameters on hole and on electron pockets (s^{+-} gap structure) [129, 77, 130, 131, 132, 75, 133, 8].

It has been argued by several groups that the multiband structure of FeSCs allows for superconducting states with more exotic properties [134, 135, 136, 137, 138, 139, 140, 141, 142, 143, 144, 145, 146, 147, 148]. Of particular interest are SC states that break time-reversal symmetry (TRS), as such states have a plethora of interesting properties like, e.g., novel collective modes [147, 142, 149, 150, 151]. TRS-broken states emerge

when the phase differences ψ_i between SC order parameters on different Fermi surfaces (FS) are not multiples of π.

The two current proposals for TRS breaking in FeSCs are $s + id$ [134, 138, 139, 140, 146] and $s + is$ states [135, 147, 142, 148]. The first emerges when attractions in the $d-$wave and $s-$wave channels are of near-equal strength. The second emerges when there is a competition between different s^{+-} states favored by inter-pocket and intra-pocket interactions. Both of these proposals were, however, argued to be applicable only to strongly hole or electron-doped FeSCc. For weakly/moderately doped FeSCs the common belief is that s^{+-} superconductivity is robust.

In this communication we argue that an exotic state which breaks TRS can emerge already at low doping, in a range where SC is known [128, 152, 153, 154, 155, 156, 157, 158, 159] to emerge from a pre-existing SDW state. We show that SDW order induces attraction in another pairing channel, for which the order parameter is an admixture of spin-singlet and spin-triplet components (the two are mixed in the SDW state since spin rotational symmetry is broken). Because a triplet component is involved, we call this a t-state. In the absence of nesting, s^{+-} and $t-$ components are linearly coupled, and the development of s^{+-} SC order at T_c triggers an immediate appearance of $t-$order component with the same phase ($s + t$ state or $s - t$ state, depending the sign of the bilinear coupling). Such a state has been discussed in the SDW/SC coexistence region of the cuprates, organic and heavy fermion materials [160, 161, 162, 163, 164, 165, 166] and the Fe-pnictides, in the context of nodeless superconductivity immediately below $T_c < T_{sdw}$ (Refs. [167, 168, 169, 170, 171, 172, 173, 174, 175, 176]).

In this letter we show that the $s \pm t$ state exists only near T_c, while at a lower T there is a phase transition into a state where a relative phase between the two SC components is different from 0 or π, i.e., the order parameter has a $s + \mathrm{e}^{i\theta} t$ form. This order parameter does not transform into itself under TRS, unlike $s + t$ order. As a result, the order parameter manifold contains an additional Z_2 Ising degree of freedom, which gets broken by selection of $+\theta$ or $-\theta$. The TRS broken state emerges via a phase transition inside a superconductor, which should have experimental manifestations. We note in this regard that, although the TRS of the system is formally broken already at the SDW transition temperature $T_N > T_c$, the TR operation transforms one magnetic state into another state from the same $O(3)$ manifold, i.e., there is no additional Z_2

degree of freedom which one could associate with TRS. Only when θ becomes different from 0 or π, does the order parameter manifold acquire an additional Z_2 degree of freedom associated with TRS.

We show that the $s + \mathrm{e}^{i\theta} t$ state emerges already in the minimal three-band model of one circular hole pocket and two symmetry-related elliptical electron pockets [177, 169, 170, 171, 172]. The presence of the other hole pockets complicates the analysis but does not lead to new physics. We argue that, when the original 4-fermion interactions are rewritten in terms of a and b fermions, which describe states near the two reconstructed FSs (Fig. 4.2) and projected onto the particle-particle subset, the two different pairing channels emerge. One is the usual spin-singlet s^{+-} channel, for which the SC order parameter is $\Delta_1 \propto \sum_{\mathbf{k}} i\sigma^y_{\alpha\beta} [\langle a_{\mathbf{k}\alpha} a_{-\mathbf{k}\beta}\rangle - \langle b_{\mathbf{k}\alpha} b_{-\mathbf{k}\beta}\rangle]$. The second pairing channel, with order parameter Δ_2, has two contributions. One is a spin-triplet inter-pocket term $\sum_{\mathbf{k}} \sigma^x_{\alpha\beta} \langle a_{\mathbf{k}\alpha} b_{-\mathbf{k}\beta}\rangle)$ (hence the name $t-$state), and the other is a spin-singlet s^{++} type term $\sum_{\mathbf{k}} i\sigma^y_{\alpha\beta} [\langle a_{\mathbf{k}\alpha} a_{-\mathbf{k}\beta}\rangle + \langle b_{\mathbf{k}\alpha} b_{-\mathbf{k}\beta}\rangle]$. The presence of the s^{++} component in Δ_2 is crucial as with it the kernel in the gap equation for Δ_2 is logarithmic (as it is for Δ_1), implying that even a weak attraction gives rise to superconductivity. We emphasize that the triplet component of Δ_2, $\langle a_{\mathbf{k}\alpha} b_{-\mathbf{k}\beta}\rangle$, would not spontaneously emerge by itself because the FSs for a and b fermions are disconnected and appears only because it couples linearly to the s^{++} component $\langle a_{\mathbf{k}\alpha} a_{-\mathbf{k}\beta}\rangle + \langle b_{\mathbf{k}\alpha} b_{-\mathbf{k}\beta}\rangle$. A similar situation emerges in Fe-pnictides with only electron pockets [140].

The structure of Δ_1 and Δ_2 is shown in Figs. 4.1a and 4.1b. Our analysis of the non-linear gap equations for Δ_1 and Δ_2 shows that the two SC orders coexist in some parameter range, and the relative phase between the two is different from 0 or π in the general case when the two orders are linearly coupled in the Ginzburg-Landau (GL) functional, and equals to $\pm\pi/2$ for the special case when linear coupling is absent (Fig. 4.3).

4.2 The model

We consider a three band model with c fermions with momenta near the hole pocket at $(0, 0)$ and f fermions with momenta near the electron pockets centered at $(0, \pi)$ and $(\pi, 0)$ in the 1-Fe Brillouin zone (Fig. 4.2a) [177, 178]. The c and f fermions form

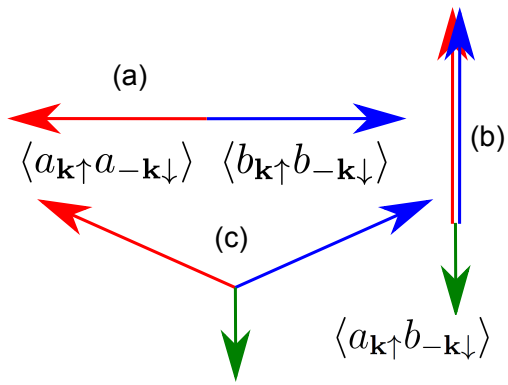

Figure 4.1: The structure of gap functions in different SC states: (a) pure s^{+-} state, (b) pure $t-$ state, (c) $s + it$ state with $\pm\pi/2$ phase difference between s^{+-} and $t-$ components. Operators a and b describe fermions near the reconstructed FSs.

circular and elliptical FSs, respectively, with dispersions given by $\xi^c_{\mathbf{k}} = \mu_c - \frac{\mathbf{k}^2}{2m_c}$ and $\xi^f_{\mathbf{k}} = -\mu_f + \frac{k_x^2}{2m_x} + \frac{k_y^2}{2m_y}$. Since the SDW state picks an ordering vector $\mathbf{Q}$, which is either $(0, \pi)$ or $(\pi, 0)$, one of the electron pockets does not participate in this order. We choose $\mathbf{Q} = (0, \pi)$ without loss of generality and effectively reduce the model to two bands. We follow earlier works [100, 179] and consider five possible repulsive interactions in the band basis: inter-pocket, density-density, exchange, pair hopping, and intra-pocket interactions. The corresponding couplings are U_1, U_2, U_3, and $U_4 = U_5$, respectively. We present the interaction Hamiltonian in the Supplementary material (SM). All couplings are assumed to be already renormalized from their bare values by fermions with energies larger than the upper energy cutoff Λ. Without SDW, SC in this model arises only in the s^{+-} channel. The corresponding coupling is $U_3 - U_4$, and we assume that it is positive (attractive). The couplings U_1 and U_2 do not participate in SC pairing, but U_1 contributes to the coupling in the SDW channel $U_1 + U_3 > 0$, which for $U_i > 0$ is larger than in SC channels. RG studies found that the SC interaction gets larger as energy decreases in the RG flow [100, 179, 180, 143]. Yet, at low doping, the SDW order comes first and SC develops in the coexistence region with magnetism.

We approximate the interactions U_i as angle independent although in general they do contain symmetry-imposed angular dependencies along the FSs, associated with the orbital content of the FSs. These angular dependencies give rise to angular variations of the s^{+-} gaps in the absence of SDW and in some cases lead to accidental gap nodes,

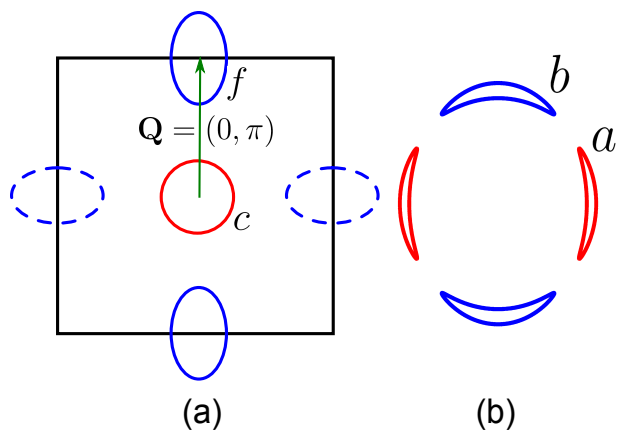

Figure 4.2: Fermi surfaces in (a) the paramagnetic state, (b) the SDW state.

e.g., in P-doped materials [133, 8, 181]. In the coexistence regime, there is an additional angular variation of the pairing interactions, imposed by the angle dependence of the SDW coherence factors which dress the bare interactions U_i [167, 168, 171, 172, 174]. Because the orbital content and the SDW coherence factors lead to similar angular dependence of the pairing interactions, we treat the original vertices as constants but keep the SDW-induced angular dependencies. The momentum dependence of the original interactions also leads to angular dependence of the SDW gap which actually vanishes along particular directions, at least in a three-pocket model [182]. This angular dependence is important at strong coupling, where it preserves a small but finite FS, but not at moderate coupling because even a constant SDW gap does not completely gap the FS [183].

The self-consistent equation for the SDW order parameter M and the reconstructed fermionic dispersions in the SDW state have been obtained before [177]. The quadratic Hamiltonian in terms of the quasiparticles a and b is

$$\mathcal{H}_0 = \sum_{\mathbf{k}} \left[\xi^a_{\mathbf{k}} a^\dagger_{\mathbf{k}\alpha} a_{\mathbf{k}\alpha} + \xi^b_{\mathbf{k}} b^\dagger_{\mathbf{k}\alpha} b_{\mathbf{k}\alpha} \right], \tag{4.1}$$

where $\xi^{a,b}_{\mathbf{k}} = \delta_{\mathbf{k}} \mp \sqrt{\xi^2_{\mathbf{k}} + M^2}$ and we have expressed the original dispersions in terms of the linear combinations $\delta_{\mathbf{k}} = \frac{\xi^f_{\mathbf{k}} + \xi^c_{\mathbf{k}}}{2}$ and $\xi_{\mathbf{k}} = \frac{\xi^f_{\mathbf{k}} - \xi^c_{\mathbf{k}}}{2}$. In general $\delta_{\mathbf{k}} = \delta_0 + \delta_2 \cos 2\theta$, where the first term measures the doping level ($\delta_0 = 0.5 v_F (k^c_F - k^f_F)$) and the second one accounts for the (weak) ellipticity of the electron pocket (Ref. [169, 170]).

The coherence factors $u_{\mathbf{k}}$ and $v_{\mathbf{k}}$ are expressed in terms of these parameters as $u_{\mathbf{k}} = \sqrt{\frac{1}{2}\left(1+\frac{\xi_{\mathbf{k}}}{\sqrt{\xi_{\mathbf{k}}^2+M^2}}\right)}$, $v_{\mathbf{k}} = \operatorname{sgn} M\sqrt{\frac{1}{2}\left(1-\frac{\xi_{\mathbf{k}}}{\sqrt{\xi_{\mathbf{k}}^2+M^2}}\right)}$ (see SM). The FSs for a and b fermions are shown in Fig. 4.2b.

4.3 Superconductivity

Re-writing the pairing interactions in terms of the new fermions, we find conventional pairing terms like $a^\dagger_{\mathbf{k}\uparrow}a^\dagger_{-\mathbf{k}\downarrow}a_{-\mathbf{p}\downarrow}a_{\mathbf{p}\uparrow}$ or $a^\dagger_{\mathbf{k}\uparrow}a^\dagger_{-\mathbf{k}\downarrow}b_{-\mathbf{p}\downarrow}b_{\mathbf{p}\uparrow}$, and anomalous terms like $a^\dagger_{\mathbf{k}\uparrow}a^\dagger_{-\mathbf{k}\downarrow}(a_{-\mathbf{p}\downarrow}b_{\mathbf{p}\uparrow}+a_{-\mathbf{p}\uparrow}b_{\mathbf{p}\downarrow})$. To solve for the SC order parameter, we then need to introduce both spin-singlet pairings $i\sigma^y_{\alpha\beta}\langle a_{\mathbf{k}\alpha}a_{-\mathbf{k}\beta}\rangle$ and $i\sigma^y_{\alpha\beta}\langle b_{\mathbf{k}\alpha}b_{-\mathbf{k}\beta}\rangle$ between fermions belonging to the same pocket, and spin triplet pairing $\sigma^x_{\alpha\beta}\langle a_{\mathbf{k}\alpha}b_{-\mathbf{k}\beta}\rangle$ between fermions belonging to different pockets.

The full pairing Hamiltonian in the BCS approximation has the form

$$\begin{aligned}\mathcal{H}_\Delta &= \frac{1}{2}i\sigma^y_{\alpha\beta}\sum_{\mathbf{p}}\left[\Delta_{aa}(\mathbf{p})a^\dagger_{\mathbf{p}\alpha}a^\dagger_{-\mathbf{p}\beta}+\Delta_{bb}(\mathbf{p})b^\dagger_{\mathbf{p}\alpha}b^\dagger_{-\mathbf{p}\beta}\right]\\ &+\frac{1}{2}\sum_{\mathbf{p}}\Delta_{ab}(\mathbf{p})\sigma^x_{\alpha\beta}[a^\dagger_{\mathbf{p}\alpha}b^\dagger_{-\mathbf{p}\beta}-b^\dagger_{\mathbf{p}\alpha}a^\dagger_{-\mathbf{p}\beta}]+\text{H.c.}\end{aligned} \tag{4.2}$$

Because there are three different anomalous terms, the diagonalization of the pairing Hamiltonian leads to a set of three coupled equations for Δ_{aa}, Δ_{bb}, and Δ_{ab}. Parameterizing Δ_{ij} as

$$\Delta_{aa,bb}(\mathbf{p}) = \pm\Delta_1+\Delta_2(2u_{\mathbf{p}}v_{\mathbf{p}})+\Delta_3(u^2_{\mathbf{p}}-v^2_{\mathbf{p}}), \tag{4.3}$$

$$\Delta_{ab}(\mathbf{p}) = \Delta_2(u^2_{\mathbf{p}}-v^2_{\mathbf{p}})-\Delta_3(2u_{\mathbf{p}}v_{\mathbf{p}}), \tag{4.4}$$

we express the equations for SC order parameters as

$$\Delta_1 = \frac{U_3-U_4}{2}\sum_{\mathbf{k}}\left[\langle aa\rangle-\langle bb\rangle\right], \tag{4.5}$$

$$\Delta_2 = (U_2-U_1)\sum_{\mathbf{k}}\left[u_{\mathbf{k}}v_{\mathbf{k}}(\langle aa\rangle+\langle bb\rangle)+(u^2_{\mathbf{k}}-v^2_{\mathbf{k}})\langle ab\rangle\right]$$

$$\Delta_3 = -\frac{U_3+U_4}{2}\sum_{\mathbf{k}}\left[(u^2_{\mathbf{k}}-v^2_{\mathbf{k}})(\langle aa\rangle+\langle bb\rangle)-4u_{\mathbf{k}}v_{\mathbf{k}}\langle ab\rangle\right]$$

where $\langle aa\rangle \equiv i\sigma^y_{\alpha\beta}\langle a_{-\mathbf{k}\beta}a_{\mathbf{k}\alpha}\rangle$, $\langle bb\rangle \equiv i\sigma^y_{\alpha\beta}\langle b_{-\mathbf{k}\beta}b_{\mathbf{k}\alpha}\rangle$, $\langle ab\rangle \equiv \sigma^x_{\alpha\beta}\langle b_{-\mathbf{k}\beta}a_{\mathbf{k}\alpha}\rangle$. Each average is in turn expressed in terms of Δ_i $(i = 1, 2, 3)$, i.e. Eqs. (4.5) represent the set of three coupled non-linear equations for the SC order parameters in the presence of SDW order.

We see from (4.5) that three combinations of the interactions U_i appear in the pairing channel. Two have familiar forms [100]: $U_3 - U_4$ and $-(U_3 + U_4)$ are the couplings in the s^{+-} and s^{++} channels, respectively, in the absence of SDW order. A non-zero M couples the s^{+-} and s^{++} channels, but since the coupling in the s^{++} channel is strongly repulsive, the SDW-induced mixing of s^{+-} and s^{++} channels should not lead to any new physics. The third coupling $U_2 - U_1$, on the other hand, does not contribute to SC in the absence of SDW order. Its presence in Eq. (4.5) implies that SDW order not only modifies the two existing pairing channels, but also generates a new channel of fermionic pairing.

We present the full expressions for $\langle ij\rangle_{\mathbf{k}}$ in the SM and here focus on the linearized gap equations, valid at the corresponding $T_{c,i}$. Expanding the r.h.s. of (4.5) to first order in Δ_{ij} we obtain

$$\begin{aligned}\langle aa\rangle_{\mathbf{k}} \pm \langle bb\rangle_{\mathbf{k}} &= \frac{\Delta_{aa}(k)}{2\xi^a_k}\tanh\frac{\xi^a_k}{2T} \pm \frac{\Delta_{bb}(k)}{2\xi^b_k}\tanh\frac{\xi^b_k}{2T}\\ \langle ab\rangle_{\mathbf{k}} &= \frac{\Delta_{ab}(k)}{2(\xi^a_k + \xi^b_k)}\left(\tanh\frac{\xi^a_k}{2T} + \tanh\frac{\xi^b_k}{2T}\right)\end{aligned} \tag{4.6}$$

where Δ_{ij} are expressed via Δ_i by Eq. (4.4). Substituting (4.6) into the r.h.s. of (4.5) we obtain the set of three coupled linearized Eqs. on Δ_i which can be easily solved.

To understand the physics, we first focus on the case of "maximally-nested" FSs, where $\delta_0 = 0$ but $\delta_2 \neq 0$, i.e. $\xi^b_{\mathbf{k}}$ becomes $-\xi^a_{\mathbf{k}}$ under a rotation by 90 degrees. We found that this symmetry decouples the three linearized gap equations for Δ_i, which become

$$\begin{aligned}&\Delta_1\left[1 - \frac{U_3 - U_4}{2}N_F\int X_{\mathbf{k}}\right] = 0\\ &\Delta_2\left[1 - (U_2 - U_1)N_F\int\left(u^2_{\mathbf{k}}v^2_{\mathbf{k}}X_{\mathbf{k}} + (u^2_{\mathbf{k}} - v^2_{\mathbf{k}})^2 Y_{\mathbf{k}}\right)\right] = 0\\ &\Delta_3\left[1 + \frac{U_3 + U_4}{2}N_F\int\left((u^2_{\mathbf{k}} - v^2_{\mathbf{k}})^2 X_{\mathbf{k}} + 8u^2_{\mathbf{k}}v^2_{\mathbf{k}}Y_{\mathbf{k}}\right)\right] = 0\end{aligned} \tag{4.7}$$

where N_F is the density of states at the FS, $\int = \int d\xi\frac{d\phi}{2\pi}$, $u_{\mathbf{k}}v_{\mathbf{k}} = M/(2\sqrt{M^2 + \xi^2_{\mathbf{k}}})$,

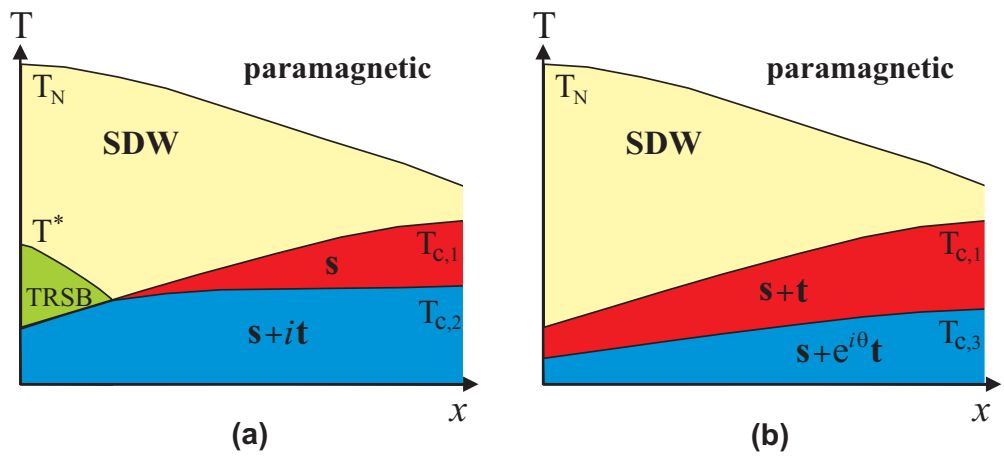

Figure 4.3: Schematic phase diagram of a superconductor in coexistence with SDW. (a) The special case when s and t order parameters do not couple linearly (nested FSs). (b) The generic case when s and t superconducting components couple linearly (non-nested FSs). In the $s + e^{i\theta}t$ and $s + it$ phases ($\theta = \pi/2$), the relative phase between the s and t components is frozen at $0 < \theta < \pi$ and TRS is broken, together with the $U(1)$ symmetry of the global phase. In the TRSB phase, only TRS is broken. This phase is likely present in the generic case but its boundaries are not known and we do not show it.

$u_{\mathbf{k}}^2 - v_{\mathbf{k}}^2 = \xi_{\mathbf{k}}/\sqrt{M^2 + \xi_{\mathbf{k}}^2}$, and

$$X_{\mathbf{k}} = \frac{\tanh \frac{\xi_{\mathbf{k}}^a}{2T_c}}{\xi_{\mathbf{k}}^a}, \quad Y_{\mathbf{k}} = \frac{\tanh \frac{\xi_{\mathbf{k}}^a}{2T_c} + \tanh \frac{\xi_{\mathbf{k}}^b}{2T_c}}{2(\xi_{\mathbf{k}}^a + \xi_{\mathbf{k}}^b)} \tag{4.8}$$

The first and the last Eqs. (4.7) have familiar forms for s^{+-} and s^{++} superconductivity. For positive U_i, the s^{++} channel is repulsive, but s^{+-} superconductivity develops at $T = T_{c,1}$ if $U_3 - U_4$ is positive. The momentum integral $\int X_{\mathbf{k}}$ is logarithmically singular, as expected in BCS theory, hence $T_{c,1}$ is non-zero already at weak coupling. The second Eq. in (4.7) is the gap equation in the new pairing channel. In the presence of SDW the kernel in this channel is also logarithmically singular due to the contribution from $\langle aa \rangle_{\mathbf{k}} + \langle bb \rangle_{\mathbf{k}}$. Hence, if $U_2 - U_1$ is positive, the $t-$channel becomes unstable towards pairing at a non-zero $T_{c,2}$. Once Δ_2 becomes non-zero, it induces a non-zero inter-pocket pairing component $\langle ab \rangle_{\mathbf{k}}$.

4.4 $s + it$ state with broken time-reversal symmetry

As it is customary for competing SC orders, the order which develops first tends to suppress the competitor by providing negative feedback to the gap equation for the competing order [147]. Yet, if the repulsion between the competing SC orders is not too strong, the two orders coexist at low enough temperatures. The issue then is what is the relative phase between the two $U(1)$ order parameters Δ_1 and Δ_2. To address this issue we derived by standard means [178, 184] the GL Free energy, $\mathcal{F}(\Delta_1, \Delta_2)$ (see SM). To fourth order in $\Delta_{1,2}$ we obtained

$$\begin{aligned}\mathcal{F}(\Delta_1, \Delta_2) = \alpha_1|\Delta_1|^2 + \alpha_2|\Delta_2|^2 + \beta_1|\Delta_1|^4 + \beta_2|\Delta_2|^4 \\ + 2\gamma_1|\Delta_1|^2|\Delta_2|^2 + \gamma_2\left(\Delta_1^2(\Delta_2^*)^2 + (\Delta_1^*)^2\Delta_2^2\right)\end{aligned} \tag{4.9}$$

where β_1 and β_2 are positive. The two orders coexist when $\beta_1\beta_2 > (\gamma_1 - |\gamma_2|)^2$. This condition can be satisfied in the presence of disorder [185, 186, 187]. The relative phase θ between $\Delta_1 = |\Delta_1|e^{i\psi+\theta/2}$ and $\Delta_2 = |\Delta_2|e^{i\psi-\theta/2}$ is determined by the sign of the γ_2 term in (4.9). We found that γ_2 is positive:

$$\gamma_2 = \sum_{\mathbf{k}}(2u_{\mathbf{k}}v_{\mathbf{k}})^2\left[\frac{1}{|\xi_{\mathbf{k}}^a|^3} + \frac{1}{|\xi_{\mathbf{k}}^b|^3}\right]. \tag{4.10}$$

Minimization of Eq. (4.9) then shows that $\theta = \pm\pi/2$. Because $\theta = \pi/2$ and $\theta = -\pi/2$ are different states, the system spontaneously breaks the Z_2 TRS. In the TRS-broken state, the phases of the order parameters $\langle aa\rangle_{\mathbf{k}}$ and $\langle bb\rangle_{\mathbf{k}}$ are ϕ and $\pi - \phi$, where $0 < \phi < \pi/2$. The third gap, which is generally required to satisfy the set of complex gap equations in the TRS-broken state is provided by $\langle ab\rangle_{\mathbf{k}}$, whose phase in this situation is $-\pi/2$. We show the gap structure schematically in Fig. 4.1 where we associated $\langle ij\rangle_{\mathbf{k}}$ with vectors, whose directions are set by the phases. We also performed Hubbard-Stratonovich analysis beyond mean-field level [178], by allowing the phases of $\Delta_{1,2}$ to fluctuate, and found (see SM) that when $T_{c,2} \approx T_{c,1} \equiv T_c$, the system breaks TRS and sets the relative phase $\theta = \pm\pi/2$ at a temperature $T^* > T_c$. In between T^* and T_c, TRS is broken, but the $U(1)$ symmetry associated with the global phase of Δ_1 and Δ_2 remains intact. Such a state is typical for systems whose order parameter manifold contains both continuous and discrete symmetries [92, 151, 188, 189]. At T_c, the global phase is broken and both SC orders develop simultaneously. A schematic phase diagram is shown in Fig. 4.3a.

4.5 $s + \mathrm{e}^{i\theta} t$ state

So far we considered the "maximally-nested" case, with $\delta_0 = 0$. For the more generic case $\delta_0 \neq 0$ we find that the GL functional (4.9) contains a bilinear coupling between the two SC states, i.e. a term $\alpha_3 \left(\Delta_1 \Delta_2^* + \Delta_1^* \Delta_2\right)$ with $\alpha_3 < 0$ (details in the SM). In this situation, the onset of the s^{+-} state at $T_{c,1}$ necessarily triggers the emergence of a t state. The relative phase between the two order parameters at $T \leq T_{c,1}$ is $\theta = 0$, i.e., the state is $s + t$. Yet, the SC state still breaks TRS at a lower temperature $T_{c,3} < T_{c,1}$. Indeed, comparing the $\alpha_3 \left(\Delta_1 \Delta_2^* + \Delta_1^* \Delta_2\right)$ and $\gamma_2 \left(\Delta_1^2 (\Delta_2^*)^2 + (\Delta_1^*)^2 \Delta_2^2\right)$ terms in the GL functional we immediately see that $\theta = 0$ only as long as $\Delta_1 \Delta_2 < \alpha_3 / 4\gamma_2$. Once the temperature is reduced and $\Delta_{1,2}$ grow, this condition breaks down at $T = T_{c,3}$, and at lower T the minimum of the GL functional shifts to $\theta \neq 0$. At a lower T, the SC state becomes $s + \mathrm{e}^{i\theta} t$ and TRS gets broken (see Fig. 4.3b). This GL analysis attests the generality of our results. In particular, the momentum dependence of the interactions, introduced by the orbital content of the FS (which we neglected), would only change the GL parameters, but not the GL form and hence would not invalidate our conclusion that an $s + \mathrm{e}^{i\theta} t$ state emerges at low T.

4.6 Technical details

In this section we discuss some technical details of the analysis presented in the main body of the chapter. These details were omitted to improve the clarity of the presentation and they are discussed here for completeness.

4.6.1 Interaction Hamiltonian

We include all five possible repulsive interactions in the band basis

$$\begin{aligned}
\mathcal{H}_{int} &= U_1 \sum c^\dagger_{\mathbf{p}_3\sigma} f^\dagger_{\mathbf{p}_4\sigma'} f_{\mathbf{p}_2\sigma'} c_{\mathbf{p}_1\sigma}, \\
&+ U_2 \sum f^\dagger_{\mathbf{p}_3\sigma} c^\dagger_{\mathbf{p}_4\sigma'} f_{\mathbf{p}_2\sigma'} c_{\mathbf{p}_1\sigma}, \\
&+ \frac{U_3}{2} \sum \left[f^\dagger_{\mathbf{p}_3\sigma} f^\dagger_{\mathbf{p}_4\sigma'} c_{\mathbf{p}_2\sigma'} c_{\mathbf{p}_1\sigma} + \mathrm{H.c.} \right], \\
&+ \frac{U_4}{2} \sum f^\dagger_{\mathbf{p}_3\sigma} f^\dagger_{\mathbf{p}_4\sigma'} f_{\mathbf{p}_2\sigma'} f_{\mathbf{p}_1\sigma} + \frac{U_5}{2} \sum c^\dagger_{\mathbf{p}_3\sigma} c^\dagger_{\mathbf{p}_4\sigma'} c_{\mathbf{p}_2\sigma'} c_{\mathbf{p}_1\sigma}.
\end{aligned} \tag{4.11}$$

The momentum conservation is implicit and $\sigma \neq \sigma'$ in all sums. The first three are inter-pocket density-density, exchange, and pair hopping, interactions, respectively (all positive), while the last two are intra-pocket repulsions. For simplicity, we set $U_4 = U_5$ below. All couplings are assumed to be already renormalized from their bare values by fermions with energies larger than the upper energy cutoff Λ.

4.6.2 SDW state

In order to introduce the SDW order starting from the paramagnetic state we first write the quadratic part of the Hamiltonian in the mean-field approximation, where the order parameter M is defined as

$$\begin{aligned} M &= -\frac{U_1 + U_3}{2} \sum_{\mathbf{p}} \sigma^z_{\alpha\beta} \left\langle c^\dagger_{\mathbf{p}\alpha} f_{\mathbf{p}\beta} \right\rangle, \\ &= -\frac{U_1 + U_3}{2} \sum_{\mathbf{p}} \sigma^z_{\alpha\beta} \left\langle f^\dagger_{\mathbf{p}\alpha} c_{\mathbf{p}\beta} \right\rangle. \end{aligned} \tag{4.12}$$

Then we perform the following Bogoliubov transformation to bring it to diagonal form:

$$c_{\mathbf{k}\alpha} = u_{\mathbf{k}} a_{\mathbf{k}\alpha} + v_{\mathbf{k}} \sigma^z_{\alpha\beta} b_{\mathbf{k}\beta}, , \tag{4.13}$$

$$f_{\mathbf{k}\alpha} = u_{\mathbf{k}} b_{\mathbf{k}\alpha} - v_{\mathbf{k}} \sigma^z_{\alpha\beta} a_{\mathbf{k}\beta}.. \tag{4.14}$$

4.6.3 Gap equations

In order to carry out the diagonalization of the mean-field Hamiltonian (4.2) we apply the following Bogoliubov transformation, introducing new quasiparticle operators α and β:

$$a_{k\mu} = u^\alpha_{\mathbf{k}} \alpha_{\mathbf{k}\mu} + v^\alpha_{\mathbf{k}} i\sigma^y_{\mu\nu} \alpha^\dagger_{-\mathbf{k}\nu} + g^\beta_{\mathbf{k}} \sigma^z_{\mu\nu} \beta_{\mathbf{k}\nu} + h^\beta_{\mathbf{k}} \sigma^x_{\mu\nu} \beta^\dagger_{-\mathbf{k}\nu}, \tag{4.15}$$

$$b_{k\mu} = u^\beta_{\mathbf{k}} \beta_{\mathbf{k}\mu} + v^\beta_{\mathbf{k}} i\sigma^y_{\mu\nu} \beta^\dagger_{-\mathbf{k}\nu} + g^\alpha_{\mathbf{k}} \sigma^z_{\mu\nu} \alpha_{\mathbf{k}\nu} + h^\alpha_{\mathbf{k}} \sigma^x_{\mu\nu} \alpha^\dagger_{-\mathbf{k}\nu}. \tag{4.16}$$

As a result, we obtain a quadratic Hamiltonian

$$\mathcal{H} = \sum_{\mathbf{k},\mu} \left[E^\alpha_{\mathbf{k}} \alpha^\dagger_{\mathbf{k}\mu} \alpha_{\mathbf{k}\mu} + E^\beta_{\mathbf{k}} \beta^\dagger_{\mathbf{k}\mu} \beta_{\mathbf{k}\mu} \right] \tag{4.17}$$

and new quasiparticle dispersions

$$E^{\alpha,\beta}_{\mathbf{k}} = \sqrt{A_{\mathbf{k}} \pm \sqrt{B_{\mathbf{k}}}}, \tag{4.18}$$

where

$$A_{\mathbf{k}} = \frac{(\xi_{\mathbf{k}}^{\alpha})^2 + (\xi_{\mathbf{k}}^{\beta})^2}{2} + |\Delta_1|^2 + |\Delta_2|^2 + |\Delta_3|^2, \tag{4.19}$$

$$\begin{aligned} B_{\mathbf{k}} = & \left(\frac{(\xi_{\mathbf{k}}^{\alpha})^2 - (\xi_{\mathbf{k}}^{\beta})^2}{2} \right)^2 \\ & + \left[(\xi_{\mathbf{k}}^{\alpha})^2 - (\xi_{\mathbf{k}}^{\beta})^2 \right] \left[t(\Delta_1 \Delta_3^* + \Delta_1^* \Delta_3) + s(\Delta_1 \Delta_2^* + \Delta_1^* \Delta_2) \right] \\ & + \left[\xi_{\mathbf{k}}^{\alpha} - \xi_{\mathbf{k}}^{\beta} \right]^2 (t\Delta_2 - s\Delta_3)(t\Delta_2^* - s\Delta_3^*) \\ & + (\Delta_1 \Delta_2^* + \Delta_1^* \Delta_2)^2 + (\Delta_1 \Delta_3^* + \Delta_1^* \Delta_3)^2 \\ & - (\Delta_2 \Delta_3^* - \Delta_2^* \Delta_3)^2, \end{aligned} \tag{4.20}$$

and we have defined $s \equiv \frac{M}{\sqrt{M^2+\xi_{\mathbf{k}}^2}}$ and $t \equiv \frac{\xi_{\mathbf{k}}}{\sqrt{M^2+\xi_{\mathbf{k}}^2}}$.

The gap equations can be found by starting with the expressions for the order parameters,

$$\Delta_1 = \frac{U_3 - U_4}{2} \sum_{\mathbf{k}} \left[\langle aa \rangle_{\mathbf{k}} - \langle bb \rangle_{\mathbf{k}} \right], \tag{4.21}$$

$$\Delta_2 = (U_2 - U_1) \sum_{\mathbf{k}} \left[u_{\mathbf{k}} v_{\mathbf{k}} (\langle aa \rangle_{\mathbf{k}} + \langle bb \rangle_{\mathbf{k}}) + (u_{\mathbf{k}}^2 - v_{\mathbf{k}}^2) \langle ab \rangle_{\mathbf{k}} \right], \tag{4.22}$$

$$\Delta_3 = -\frac{U_3 + U_4}{2} \sum_{\mathbf{k}} \left[(u_{\mathbf{k}}^2 - v_{\mathbf{k}}^2)(\langle aa \rangle_{\mathbf{k}} + \langle bb \rangle_{\mathbf{k}}) - 4 u_{\mathbf{k}} v_{\mathbf{k}} \langle ab \rangle_{\mathbf{k}} \right], \tag{4.23}$$

and substituting the following expressions for the averages $\langle ij \rangle$:

$$\begin{aligned} \langle aa \rangle_{\mathbf{k}} - \langle bb \rangle_{\mathbf{k}} = & -(u_{\mathbf{k}}^{\alpha} v_{\mathbf{k}}^{\alpha} + g_{\mathbf{k}}^{\alpha} h_{\mathbf{k}}^{\alpha})(1 - 2n_F(E_{\mathbf{k}}^{\alpha})) \\ & + (u_{\mathbf{k}}^{\beta} v_{\mathbf{k}}^{\beta} + g_{\mathbf{k}}^{\beta} h_{\mathbf{k}}^{\beta})(1 - 2n_F(E_{\mathbf{k}}^{\beta})), \end{aligned} \tag{4.24}$$

$$\begin{aligned} \langle aa \rangle_{\mathbf{k}} + \langle bb \rangle_{\mathbf{k}} = & (-u_{\mathbf{k}}^{\alpha} v_{\mathbf{k}}^{\alpha} + g_{\mathbf{k}}^{\alpha} h_{\mathbf{k}}^{\alpha})(1 - 2n_F(E_{\mathbf{k}}^{\alpha})) \\ & + (-u_{\mathbf{k}}^{\beta} v_{\mathbf{k}}^{\beta} + g_{\mathbf{k}}^{\beta} h_{\mathbf{k}}^{\beta})(1 - 2n_F(E_{\mathbf{k}}^{\beta})), \end{aligned} \tag{4.25}$$

$$\begin{aligned} \langle ab \rangle_{\mathbf{k}} = & u_{\mathbf{k}}^{\alpha} h_{\mathbf{k}}^{\alpha} (1 - n_F(E_{\mathbf{k}}^{\alpha})) - v_{\mathbf{k}}^{\alpha} g_{\mathbf{k}}^{\alpha} n_F(E_{\mathbf{k}}^{\alpha}) \\ & + u_{\mathbf{k}}^{\beta} h_{\mathbf{k}}^{\beta} n_F(E_{\mathbf{k}}^{\beta}) - v_{\mathbf{k}}^{\beta} g_{\mathbf{k}}^{\beta} (1 - n_F(E_{\mathbf{k}}^{\beta})), \end{aligned} \tag{4.26}$$

where n_F is the Fermi distribution function.

The coherence factors are given by

$$(u^\alpha_{\mathbf{k}}, v^\alpha_{\mathbf{k}}, g^\alpha_{\mathbf{k}}, h^\alpha_{\mathbf{k}}) = \frac{(U^\alpha_{\mathbf{k}}, V^\alpha_{\mathbf{k}}, G^\alpha_{\mathbf{k}}, H^\alpha_{\mathbf{k}})}{\sqrt{|U^\alpha_{\mathbf{k}}|^2 + |V^\alpha_{\mathbf{k}}|^2 + |G^\alpha_{\mathbf{k}}|^2 + |H^\alpha_{\mathbf{k}}|^2}} \tag{4.27}$$

$$\left(u^\beta_{\mathbf{k}}, v^\beta_{\mathbf{k}}, g^\beta_{\mathbf{k}}, h^\beta_{\mathbf{k}}\right) = \frac{\left(U^\beta_{\mathbf{k}}, V^\beta_{\mathbf{k}}, G^\beta_{\mathbf{k}}, H^\beta_{\mathbf{k}}\right)}{\sqrt{|U^\beta_{\mathbf{k}}|^2 + |V^\beta_{\mathbf{k}}|^2 + |G^\beta_{\mathbf{k}}|^2 + |H^\beta_{\mathbf{k}}|^2}}, \tag{4.28}$$

where

$$\begin{aligned} U^\alpha_{\mathbf{k}} = {} & [E^\alpha_{\mathbf{k}} + \xi^a_{\mathbf{k}}][-|\Delta_1|^2 - |\Delta_2|^2 + s(\Delta_1\Delta_2^* + \Delta_1^*\Delta_2) \\ & \quad + t(\Delta_1\Delta_3^* + \Delta_1^*\Delta_3)] \\ & + t[\xi^a_{\mathbf{k}} - \xi^b_{\mathbf{k}}][t|\Delta_2|^2 - t|\Delta_3|^2 + s(\Delta_2\Delta_3^* + \Delta_2^*\Delta_3)] \\ & + [E^\alpha_{\mathbf{k}} + \xi^b_{\mathbf{k}}][(E^\alpha_{\mathbf{k}} + \xi^a_{\mathbf{k}})(E^\alpha_{\mathbf{k}} - \xi^b_{\mathbf{k}}) - |\Delta_3|^2] \end{aligned} \tag{4.29}$$

$$\begin{aligned} U^\beta_{\mathbf{k}} = {} & [E^\beta_{\mathbf{k}} + \xi^b_{\mathbf{k}}][-|\Delta_1|^2 - |\Delta_2|^2 - s(\Delta_1\Delta_2^* + \Delta_1^*\Delta_2) \\ & \quad - t(\Delta_1\Delta_3^* + \Delta_1^*\Delta_3)] \\ & + t[\xi^b_{\mathbf{k}} - \xi^a_{\mathbf{k}}][t|\Delta_2|^2 - t|\Delta_3|^2 + s(\Delta_2\Delta_3^* + \Delta_2^*\Delta_3)] \\ & + [E^\beta_{\mathbf{k}} + \xi^a_{\mathbf{k}}][(E^\beta_{\mathbf{k}} + \xi^b_{\mathbf{k}})(E^\beta_{\mathbf{k}} - \xi^a_{\mathbf{k}}) - |\Delta_3|^2] \end{aligned} \tag{4.30}$$

$$\begin{aligned} V^\alpha_{\mathbf{k}} = {} & [-(E^\alpha_{\mathbf{k}})^2 + (\xi^b_{\mathbf{k}})^2][\Delta_1 + s\Delta_2 + t\Delta_3] \\ & + [\Delta_1^2 - \Delta_2^2 - \Delta_3^2][\Delta_1^* - s\Delta_2^* - t\Delta_3^*] \end{aligned} \tag{4.31}$$

$$\begin{aligned} V^\beta_{\mathbf{k}} = {} & [-(E^\beta_{\mathbf{k}})^2 + (\xi^a_{\mathbf{k}})^2][-\Delta_1 + s\Delta_2 + t\Delta_3] \\ & + [\Delta_1^2 - \Delta_2^2 - \Delta_3^2][-\Delta_1^* - s\Delta_2^* - t\Delta_3^*] \end{aligned} \tag{4.32}$$

$$\begin{aligned} G^\alpha_{\mathbf{k}} = {} & [E^\alpha_{\mathbf{k}} + \xi^a_{\mathbf{k}}][t\Delta_1\Delta_2^* - s\Delta_1\Delta_3^* + \Delta_2\Delta_3^*] \\ & + [E^\alpha_{\mathbf{k}} + \xi^b_{\mathbf{k}}][t\Delta_1^*\Delta_2 - s\Delta_1^*\Delta_3 - \Delta_2^*\Delta_3] \\ & + t[\xi^a_{\mathbf{k}} - \xi^b_{\mathbf{k}}][s(-|\Delta_2|^2 + |\Delta_3|^2) - t(\Delta_2\Delta_3^* + \Delta_2^*\Delta_3)] \end{aligned} \tag{4.33}$$

$$
\begin{aligned}
G^{\beta}_{\mathbf{k}} = & [E^{\beta}_{\mathbf{k}} + \xi^{b}_{\mathbf{k}}][t\Delta_1\Delta_2^* - s\Delta_1\Delta_3^* - \Delta_2\Delta_3^*] \\
& + [E^{\beta}_{\mathbf{k}} + \xi^{a}_{\mathbf{k}}][t\Delta_1^*\Delta_2 - s\Delta_1^*\Delta_3 + \Delta_2^*\Delta_3] \\
& + t[\xi^{a}_{\mathbf{k}} - \xi^{b}_{\mathbf{k}}][s(-|\Delta_2|^2 + |\Delta_3|^2) - t(\Delta_2\Delta_3^* + \Delta_2^*\Delta_3)]
\end{aligned} \tag{4.34}
$$

$$
\begin{aligned}
H^{\alpha}_{\mathbf{k}} = & [E^{\alpha}_{\mathbf{k}} + \xi^{a}_{\mathbf{k}}][E^{\alpha}_{\mathbf{k}} - \xi^{b}_{\mathbf{k}}][t\Delta_2 - s\Delta_3] \\
& + [\Delta_1^2 - \Delta_2^2 - \Delta_3^2][t\Delta_2^* - s\Delta_3^*]
\end{aligned} \tag{4.35}
$$

$$
\begin{aligned}
H^{\beta}_{\mathbf{k}} = & [E^{\beta}_{\mathbf{k}} + \xi^{b}_{\mathbf{k}}][E^{\beta}_{\mathbf{k}} - \xi^{a}_{\mathbf{k}}][-t\Delta_2 + s\Delta_3] \\
& + [\Delta_1^2 - \Delta_2^2 - \Delta_3^2][-t\Delta_2^* + s\Delta_3^*]
\end{aligned} \tag{4.36}
$$

The expansion of the gap equations to linear order in Δ_i yields

$$
\begin{aligned}
\Delta_1 = & \frac{U_3 - U_4}{2} \sum_{\mathbf{k}} \left\{ \Delta_1 \left[\frac{\tanh(\xi^{a}_{\mathbf{k}}/(2T))}{2\xi^{a}_{\mathbf{k}}} + (a \to b) \right] \right. \\
& \left. + \Delta_2 s \left[\frac{\tanh(\xi^{a}_{\mathbf{k}}/(2T))}{2\xi^{a}_{\mathbf{k}}} - (a \to b) \right] \right\}
\end{aligned} \tag{4.37}
$$

$$
\begin{aligned}
\Delta_2 = & (U_2 - U_1) \sum_{\mathbf{k}} \left\{ \Delta_2 \frac{s^2}{2} \left[\frac{\tanh(\xi^{a}_{\mathbf{k}}/(2T))}{2\xi^{a}_{\mathbf{k}}} + (a \to b) \right] \right. \\
& + \Delta_2 t^2 \left[\frac{\tanh(\xi^{a}_{\mathbf{k}}/(2T)) + \tanh(\xi^{b}_{\mathbf{k}}/(2T))}{2(\xi^{a}_{\mathbf{k}} + \xi^{b}_{\mathbf{k}})} \right] \\
& \left. + \Delta_1 \frac{s}{2} \left[\frac{\tanh(\xi^{a}_{\mathbf{k}}/(2T))}{2\xi^{a}_{\mathbf{k}}} - (a \to b) \right] \right\}
\end{aligned} \tag{4.38}
$$

$$
\begin{aligned}
\Delta_3 = & -\frac{U_3 + U_4}{2} \Delta_3 \sum_{\mathbf{k}} \left\{ t^2 \left[\frac{\tanh(\xi^{a}_{\mathbf{k}}/(2T))}{2\xi^{a}_{\mathbf{k}}} + (a \to b) \right] \right. \\
& \left. + 2s^2 \left[\frac{\tanh(\xi^{a}_{\mathbf{k}}/(2T)) + \tanh(\xi^{b}_{\mathbf{k}}/(2T))}{2(\xi^{a}_{\mathbf{k}} + \xi^{b}_{\mathbf{k}})} \right] \right\}
\end{aligned} \tag{4.39}
$$

Note that Δ_3 is decoupled from Δ_1 and Δ_2 in linear order even if $\delta_0 \neq 0$

4.6.4 Coexistence of superconducting orders

We present the conditions that are necessary for the coexistence of the Δ_1 and Δ_2 orders. We begin by listing the full expressions for all the coefficients of the free energy.

$$\begin{aligned}\mathcal{F}(\Delta_1,\Delta_2) = \alpha_1|\Delta_1|^2 + \alpha_2|\Delta_2|^2 + \alpha_3(\Delta_1\Delta_2^* + \Delta_1^*\Delta_2) \\ + \beta_1|\Delta_1|^4 + \beta_2|\Delta_2|^4 + 2\gamma_1|\Delta_1|^2|\Delta_2|^2 \\ + \gamma_2\left(\Delta_1^2(\Delta_2^*)^2 + (\Delta_1^*)^2\Delta_2^2\right)\end{aligned} \tag{4.40}$$

$$\alpha_1 = -\frac{1}{2}\sum_{\mathbf{k}}\left[\frac{1}{|\xi_{\mathbf{k}}^a|} + \frac{1}{|\xi_{\mathbf{k}}^b|}\right] + \frac{2}{U_3 - U_4}, \tag{4.41}$$

$$\begin{aligned}\alpha_2 = -\frac{1}{2}\sum_{\mathbf{k}} s^2\left[\frac{1}{|\xi_{\mathbf{k}}^a|} + \frac{1}{|\xi_{\mathbf{k}}^b|}\right] \\ - \sum_{\mathbf{k}} t^2\frac{\operatorname{sgn}\xi_{\mathbf{k}}^a + \operatorname{sgn}\xi_{\mathbf{k}}^b}{\xi_{\mathbf{k}}^a + \xi_{\mathbf{k}}^b} + \frac{2}{U_2 - U_1},\end{aligned} \tag{4.42}$$

$$\alpha_3 = -\frac{1}{2}\sum_{\mathbf{k}} s\left[\frac{1}{|\xi_{\mathbf{k}}^a|} - \frac{1}{|\xi_{\mathbf{k}}^b|}\right], \tag{4.43}$$

$$\beta_1 = \frac{1}{8}\sum_{\mathbf{k}}\left[\frac{1}{|\xi_{\mathbf{k}}^a|^3} + \frac{1}{|\xi_{\mathbf{k}}^b|^3}\right], \tag{4.44}$$

$$\begin{aligned}\beta_2 = \frac{1}{8}\sum_{\mathbf{k}} s^4\left[\frac{1}{|\xi_{\mathbf{k}}^a|^3} + \frac{1}{|\xi_{\mathbf{k}}^b|^3}\right] \\ + \sum_{\mathbf{k}} t^4\left[\frac{\operatorname{sgn}\xi_{\mathbf{k}}^a + \operatorname{sgn}\xi_{\mathbf{k}}^b}{(\xi_{\mathbf{k}}^a + \xi_{\mathbf{k}}^b)^3}\right]\end{aligned} \tag{4.45}$$

$$\begin{aligned}\gamma_1 = \gamma_2 + \frac{1}{8}\sum_{\mathbf{k}} s^2\left[\frac{1}{|\xi_{\mathbf{k}}^a|^3} + \frac{1}{|\xi_{\mathbf{k}}^b|^3}\right] \\ + \frac{1}{4}\sum_{\mathbf{k}} t^2\left[\frac{\operatorname{sgn}\xi_{\mathbf{k}}^a}{(\xi_{\mathbf{k}}^a)^2(\xi_{\mathbf{k}}^a + \xi_{\mathbf{k}}^b)} + \frac{\operatorname{sgn}\xi_{\mathbf{k}}^b}{(\xi_{\mathbf{k}}^b)^2(\xi_{\mathbf{k}}^a + \xi_{\mathbf{k}}^b)}\right],\end{aligned} \tag{4.46}$$

$$\begin{aligned}\gamma_2 = \frac{1}{8}\sum_{\mathbf{k}} s^2\left[\frac{1}{|\xi_{\mathbf{k}}^a|^3} + \frac{1}{|\xi_{\mathbf{k}}^b|^3}\right] \\ + \frac{1}{4}\sum_{\mathbf{k}}\frac{t^2}{(\xi_{\mathbf{k}}^a)^2 - (\xi_{\mathbf{k}}^b)^2}\left[-\frac{1}{|\xi_{\mathbf{k}}^a|} + \frac{1}{|\xi_{\mathbf{k}}^b|}\right].\end{aligned} \tag{4.47}$$

The largest contribution to these integrals comes from the regions around $\xi^a_{\mathbf{k}} = 0$ and $\xi^b_{\mathbf{k}} = 0$ (the SDW FSs), where the denominators become zero. This singularity is caused by calculating the coefficients at $T = 0$ and is removed by including a small cutoff at those points. One may think that the regions where $\xi^a_{\mathbf{k}} + \xi^a_{\mathbf{k}} = 0$ are also singular but in each case the integrand is actually finite. Thus the main contributions to the coefficients β_i and γ_i are the integrals with $|\xi^{a,b}_{\mathbf{k}}|^{-3}$. All of these are positive definite so $\beta_i > 0$ and $\gamma_i > 0$.

In the case of $\delta_0 = 0$ the coefficient α_3 vanishes, so the order parameters decouple at linear order. To determine whether coexistance occurs we search for minima of the free energy where both parameters are non-zero. First note that the remaining terms depend only on $|\Delta_1|^2$ and $|\Delta_2|^2$, except for the term with coefficient γ_2. Since $\gamma_2 > 0$, the minimum value of this term is $-2\gamma_2|\Delta_1|^2|\Delta_2|^2$, which corresponds to a phase difference between Δ_1 and Δ_2 of $\pm\pi/2$. After we fix this phase, partial differentiation with respect to $|\Delta_1|^2$ and $|\Delta_2|^2$ yields the following critical points:

$$|\Delta_1|^2 = \frac{\alpha_2(\gamma_1 - \gamma_2) - \alpha_1\beta_2}{2(\beta_1\beta_2 - (\gamma_1 - \gamma_2)^2)}, \tag{4.48}$$

$$|\Delta_2|^2 = \frac{\alpha_1(\gamma_1 - \gamma_2) - \alpha_2\beta_1}{2(\beta_1\beta_2 - (\gamma_1 - \gamma_2)^2)}. \tag{4.49}$$

We then perform the second partial derivative test to find a necessary condition for the existence of local minima. This condition is

$$\beta_1\beta_2 > (\gamma_1 - \gamma_2)^2. \tag{4.50}$$

In addition, we require that the expressions for $|\Delta_1|^2$ and $|\Delta_2|^2$ be positive, which implies

$$\alpha_2(\gamma_1 - \gamma_2) - \alpha_1\beta_2 > 0, \tag{4.51}$$

$$\alpha_1(\gamma_1 - \gamma_2) - \alpha_2\beta_1 > 0. \tag{4.52}$$

Coexistence will occur if and only if all three inequalities are satisfied.

4.6.5 Preemtive TRS breaking above T_c

In this section we show our Hubbard-Stratonovich analysis beyond mean-field level. We take the Ginzburg-Landau free energy as an effective action and study the case where $\delta_0 = 0$ and the critical temperatures $T_{c1} \approx T_{c2}$. We consider an action of the form

$$\begin{aligned}\mathcal{S}(\Delta_1,\Delta_2) = \alpha(|\Delta_1|^2+|\Delta_2|^2) \\ + \beta_1(|\Delta_1|^2+|\Delta_2|^2)^2 - \beta(|\Delta_1|^2-|\Delta_2|^2)^2 \\ + \gamma\left(\Delta_1\Delta_2^* - \Delta_1^*\Delta_2\right)^2 \end{aligned} \tag{4.53}$$

where $\alpha = a(T-T_c)$ and a, β_1, β, and γ are positive. Then we apply a Hubbard-Stratonovich transformation to this action by introducing collective variables $\tilde{\Phi}$, Υ, and Γ, which are conjugate to $(|\Delta_1|^2+|\Delta_2|^2)^2$, $(|\Delta_1|^2-|\Delta_2|^2)^2$, and $(\Delta_1\Delta_2^*-\Delta_1^*\Delta_2)^2$, respectively. By integrating out the fields Δ_1 and Δ_2 we obtain an effective action

$$\begin{aligned}\mathcal{S}(\Phi,\Upsilon,\Gamma) = \frac{\tilde{\Phi}^2}{4\beta_1} + \frac{\Upsilon^2}{4\beta} + \frac{\Gamma^2}{4\gamma} \\ + \int \frac{\mathrm{d}^2\mathbf{q}}{(2\pi)^2} \log\left[\left(\alpha - i\tilde{\Phi} + \mathbf{q}^2\right)^2 - \Upsilon^2 - \Gamma^2\right],\end{aligned} \tag{4.54}$$

where we included the usual $\mathbf{q}^2$ dispersion in the quadratic term by replacing α by $\alpha+\mathbf{q}^2$.

Now we seach for local minima of this action by differentiating with respect to the three fields, obtaining a set of coupled equations. The solution requires $\tilde{\Phi}$ to be purely imaginary, that is $\tilde{\Phi} = i\Phi$. The set of equations becomes

$$\Phi = 4\beta_1 \int \frac{\mathrm{d}^2\mathbf{q}}{(2\pi)^2} \frac{\alpha+\Phi+\mathbf{q}^2}{(\alpha+\Phi+\mathbf{q}^2)^2 - \Upsilon^2 - \Gamma^2}, \tag{4.55}$$

$$\Upsilon = 4\beta \int \frac{\mathrm{d}^2\mathbf{q}}{(2\pi)^2} \frac{\Upsilon}{(\alpha+\Phi+\mathbf{q}^2)^2 - \Upsilon^2 - \Gamma^2}, \tag{4.56}$$

$$\Gamma = 4\gamma \int \frac{\mathrm{d}^2\mathbf{q}}{(2\pi)^2} \frac{\Gamma}{(\alpha+\Phi+\mathbf{q}^2)^2 - \Upsilon^2 - \Gamma^2}. \tag{4.57}$$

Note that Γ and Υ cannot simultaneously be nonzero as a solution to these equations except in the special case of $\beta = \gamma$.

We first consider the solution with $\Gamma = \Upsilon = 0$, which yields

$$\Phi = \frac{\beta_1}{\pi} \log \frac{\Lambda}{|\alpha+\Phi|}, \tag{4.58}$$

where Λ is an upper cutoff for the momentum integral. By expanding the action about this solution we find that it is stable as long as $\alpha > \max(\alpha_{cr1}, \alpha_{cr2})$, where

$$\alpha_{cr1} = \frac{\gamma}{\pi} - \frac{\beta_1}{\pi} \log \frac{\pi\Lambda}{\gamma}, \tag{4.59}$$

$$\alpha_{cr2} = \frac{\beta}{\pi} - \frac{\beta_1}{\pi} \log \frac{\pi\Lambda}{\beta} \tag{4.60}$$

This condition is equivalent to $T > T^*$ where $T^* = T_c + \max(\alpha_{cr1}, \alpha_{cr2})/a$. Whichever is greater between γ and β determines this critical temperature. Then if $\gamma > \beta$ ($\gamma < \beta$) the field Γ (Υ) will develop a nonzero solution and the other one will remain zero. When we calculate β and γ in terms of the original coefficients of the Ginzburg-Landau free energy we find that indeed $\gamma > \beta$. This means that a preemtive order forms at a temperature above the critical temperature, where time-reversal symmetry is broken before the gaps acquire non-zero mean-field values.

This can be verified by solving the set of equations for $\Gamma \neq 0$. Expanding at small Γ we find that

$$\Gamma^2 \left(\frac{\beta_1}{\gamma} - 2 \right) \propto (T^* - T), \tag{4.61}$$

which means that if $\beta_1 > 2\gamma$ (which is satisfied in our case) then Γ gradually increases as T becomes smaller than T^*, as expected for a second-order transition.

4.7 Summary

In this chapter we argued that a SC state, which explicitly breaks TRS, appears when SC emerges from a pre-existing SDW-ordered state. We found that in the presence of SDW, the spin-triplet channel with inter-pocket pairing couples to spin-singlet intra-pocket pairings on the reconstructed FSs. This leads to the emergence of a new pairing channel, which we labeled as $t-$pairing to emphasize that it involves spin-triplet. We analyzed the interplay between s^{+-} and $t-$ SC orders and showed that they coexist at low T with a relative phase $0 < \theta < \pi$. As a result, the phases of the gaps on different FSs differ by less than a multiple of π. Such a state breaks time-reversal symmetry and has been long sought in the studies of FeSCs. We argued that in a generic case TRS gets broken in the SC manifold at temperatures lower than T_c. This should give rise to features in experimentally probed thermodynamic quantities.

Chapter 5

Gap structure with accidental nodes: The role of hybridization

5.1 Introduction

As mentioned in Chapter 1, the multi-band nature of Fe pnictides/chalcogenides allows for many different gap structures, but the prevailing scenario is that the pairing occurs between electrons on the same Fermi surface (FS) and the superconducting gap function has s^{+-} symmetry, i.e., the gap changes sign between hole and electron pockets. There is experimental evidence that in some members of the family, like $BaFe_2(As_{1-x}P_x)_2$,[190] LaOFeP,[191] and LiFeP,[192, 193] the gap has nodes, likely on the electron pockets.

Previous studies of the gap structure were mostly restricted to an Fe-only approach, in which a generic model of the band structure consists of two nearly circular hole pockets centered at $(0, 0)$ and two elliptical electron pockets centered at $(\pi, 0)$ and $(0, \pi)$ in the first Brillouin zone (BZ) (see Figure 5.1). In some systems there exists, at least for some k_z, a third hole pocket, centered at (π, π).

The s^{+-} superconductivity is believed to be chiefly caused by a magnetically enhanced interaction between hole and electron pockets. The nodes on the two electron pockets come about because by symmetry the s-wave gap on these pockets has the form $\Delta(1 \pm \alpha \cos 2\theta_k)$ (plus higher harmonics), and if $\alpha > 1$, the gap vanishes at $\cos 2\theta_k = \pm 1/\alpha$. [75, 74, 194].

However, this Fe-only scenario is incomplete because the electron hopping between

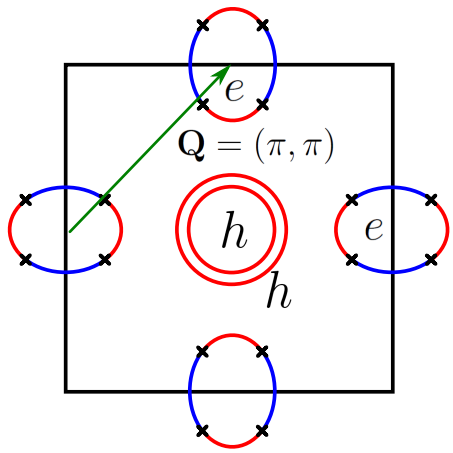

Figure 5.1: Unfolded Brillouin zone with one Fe atom per unit cell (with no hybridization). Holes and electron pockets are labeled by h and e, respectively. The crosses on the electron pockets indicate where the nodal lines of the gap function intersect the Fermi surface.

Fe atoms predominantly occurs via pnictogen or chalcogen sites, half of which are located above and half below each Fe layer in a checkerboard pattern (see Fig. 1.1) [195, 196, 197, 198, 199, 200, 201, 202]. As a result, the actual symmetry is lower than that of the Fe-only lattice, and the correct unit cell contains two Fe atoms. The non-equivalence of hopping from above and from below an iron layer causes the electron pockets to hybridize. In this chapter we will study the effect of this hybridization on the gap structure.

In order to incorporate this effect into models with one Fe atom in the unit cell, one has to include additional terms in the Hamiltonian with excess momentum $\mathbf{Q} = (\pi, \pi)$. This does not actually violate conservation of momentum because this vector folds into a reciprocal lattice vector in the actual BZ with two Fe atoms per unit cell. The momentum $\mathbf{Q}$ connects the two electron FSs and also the hole pocket centered at (π, π) with the other two hole pockets. Our primary goal will be to study how the accidental nodes on the electron pockets evolve once we include hybridization. Therefore, we focus on the effect of hybridization on the electron pockets.

The hybridization gives rise to two effects. First, hopping via a pnictogen/chalcogen sites gives rise to an additional quadratic term in the Hamiltonian for two electron

pockets

$$\mathcal{H}_\lambda = \sum_{\mathbf{k}} \left[\lambda_k c^\dagger_{\mathbf{k}\alpha} d_{\mathbf{k}+\mathbf{Q}\alpha} + \lambda^*_k d^\dagger_{\mathbf{k}\alpha} c_{\mathbf{k}+\mathbf{Q}\alpha} \right], \tag{5.1}$$

where c and d are operators for electrons near each of the two electron FSs (we discuss the form of λ_k in the next section) and the sum over repeated spin indices is implied. This cross-term mixes the two electron pockets and reconstructs the electron FSs. Second, there appear new four-fermion interaction terms in which incoming and outgoing momenta differ by $\mathbf{Q}$. In the superconducting state, in which we are interested, two out of four fermions can be put into the condensate and the four-fermion terms with excess momentum $\mathbf{Q}$ reduce to quadratic terms with prefactors proportional to the superconducting gap. These new terms describe inter-pocket pairing between fermions from two different electron pockets:

$$\mathcal{H}_\beta = \frac{1}{2} \sum_{\mathbf{k}} \beta_k \left[c^\dagger_{\mathbf{k}\alpha} d^\dagger_{-\mathbf{k}-Q\beta} + d^\dagger_{\mathbf{k}\alpha} c^\dagger_{-\mathbf{k}-Q\beta} \right] i\sigma^y_{\alpha\beta} + \text{H.c.} \tag{5.2}$$

In other words, due to hybridization, the non-zero intra-pocket pairing condensates $\langle c^\dagger_{\mathbf{k}\alpha} c^\dagger_{-\mathbf{k}\beta} \rangle$ and $\langle d^\dagger_{\mathbf{k}+\mathbf{Q}\alpha} d^\dagger_{-\mathbf{k}-\mathbf{Q}\beta} \rangle$ induce inter-pocket pairing between the two electron pockets.

In this chapter we study how the additional terms $\mathcal{H}_\lambda$ and $\mathcal{H}_\beta$ affect the gap structure when nodes are present on the electron pockets. The effect of the hopping $\lambda_{\mathbf{k}}$ term alone has been studied before[203], but not its interplay with the pairing term. We find that the hopping and inter-pocket pairing terms generally pull the nodal points in opposite direction. If the $\lambda_{\mathbf{k}}$ term dominates and reaches a certain threshold value, the nodes merge and disappear at particular symmetry points, and the gap acquires a uniform and equal phase on the two electron pockets (opposite to the phase on the hole pockets). In contrast, when β_k dominates and reaches a threshold value, the nodes merge and disappear at a different set of symmetry points and the phase of the superconducting order parameter becomes opposite on the hybridized electron pockets. This is the same gap structure that was recently found in the analysis of pairing in the orbital formalism[144] and dubbed orbital anti-phase s^{+-} state. The state with opposite signs of the gaps on the two electron pockets has also been found in the analysis of possible superconducting states in LiFeAs, albeit for a different reason [204]. As an interesting peculiarity, we found that for elliptical pockets nodes disappear in a rather non-trivial

way – first new nodes appear and the number of nodes doubles, and then the new and already existing nodes merge and disappear. Such behavior has not been found before in the studies of multi-band superconductors, as far as we know.

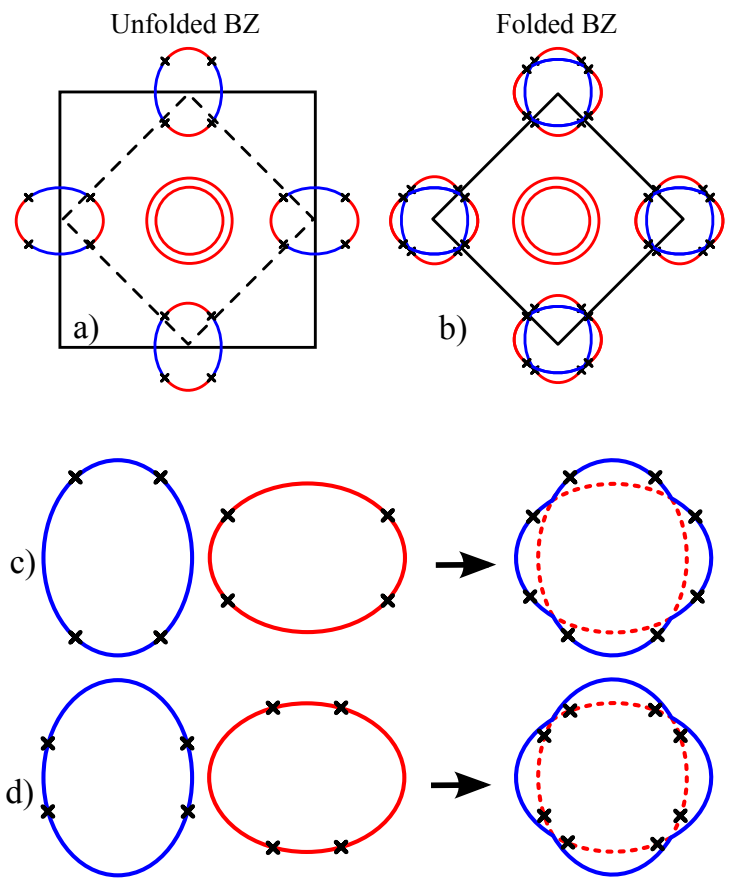

Figure 5.2: Fermi surface folding. a) Unfolded Brillouin zone corresponding to a 1Fe unit cell. b) Folded Brillouin zone corresponding to a 2Fe unit cell. The electron Fermi surfaces overlap and are reconstructed into outer and inner parts. Depending on their original location, the nodes of the gap function are either all located on the outer surface, as shown in c), or on the inner surface, as shown in d).

The hybridization between electron pockets, either due to $\mathcal{H}_\lambda$ or to $\mathcal{H}_\beta$, has to be distinguished from the effect of the folding of the 1Fe BZ into the 2Fe BZ. Upon folding, fermionic momenta transform as $\tilde{k}_x = k_x + k_y, \tilde{k}_y = k_y - k_x$, and the two electron FSs, originally centered at $(0, \pi)$ and $(\pi, 0)$, merge around (π, π) (see Fig. 5.2). The inner and outer FSs touch each other along $\tilde{k}_x = \pi$ or $\tilde{k}_y = \pi$. The merging can be

viewed as "reconstruction" of the two electron FSs into an inner FS with no nodes and an outer FS with 8 nodes, or vice versa. However, this "reconstruction" is just a rotation in momentum space and a re-branding. The k_F remains the same and the location of the nodes remains at exactly the same angles as without folding, only the reference axis rotates by 45°. The hybridization is a different phenomenon – it actually reconstructs the original FSs into an inner and an outer FSs at *new* k_F and creates a pairing component between them. As a consequence, the position of the nodal points shifts.

The chapter is organized as follows: In Section 5.2 we discuss our model. In Section 5.3, we consider, as a warm-up, the limiting case of circular electron pockets and analyze the two effects of hybridization first separately and then together and study their interplay. Section 5.4 extends the analysis to the more general case of elliptical pockets. We summarize our findings in Section 5.5.

5.2 The model

We consider a two-dimensional multi-band model with hole pockets centered at $(0,0)$ and elliptical electron pockets centered at $(0,\pi)$ and $(\pi,0)$ in the unfolded BZ. In the normal state, the Hamiltonian describing the two non-hybridized electron pockets is simply

$$\mathcal{H}_0 = \sum_{\mathbf{k}} \left[\xi^c_{\mathbf{k}} c^\dagger_{\mathbf{k}\alpha} c_{\mathbf{k}\alpha} + \xi^d_{\mathbf{k}} d^\dagger_{\mathbf{k}\alpha} d_{\mathbf{k}\alpha} \right]. \tag{5.3}$$

We assume that the dominant interaction which leads to s^{+-} superconductivity is the repulsion between electron and hole pockets, enhanced by (π,π) spin fluctuations (in the 2Fe BZ). The s-wave gap on the hole pockets is invariant under rotations by $\pi/2$, so it can be expanded in $\cos 4n\phi$ harmonics, where ϕ is the angle along the hole pocket and n is an integer. On the electron pockets the expansion of the $s-$wave gap contains $\cos 2n\theta$ terms, where θ is the angle along the electron pockets and the components with odd $n = 1, 3, \ldots$ have opposite signs on the two electron pockets, if we measure θ from the same direction for both pockets [74]. These odd multiples of 2θ are allowed because the electron pockets transform into each other under a rotation by $\pi/2$. Numerical analysis[75, 194] shows that the gap on the electron pockets can be well-approximated by the two first harmonics $n = 0$ and $n = 1$, whose magnitudes are

generally comparable to each other. Accordingly, we set $\Delta_{e1}(\theta_{\mathbf{k}}) = \Delta(1 - \alpha\cos 2\theta_{\mathbf{k}})$, $\Delta_{e2}(\theta_{\mathbf{k}+\mathbf{Q}}) = \Delta(1 + \alpha\cos 2\theta_{\mathbf{k}+\mathbf{Q}})$. The corresponding term in the Hamiltonian is thus

$$\mathcal{H}_{\Delta} = \frac{1}{2}\sum_{\mathbf{k}} \Delta \left[(1 - y_{\mathbf{k}})c^{\dagger}_{\mathbf{k}\alpha}c^{\dagger}_{-\mathbf{k}\beta} + (1 + y_{\mathbf{k}+\mathbf{Q}})d^{\dagger}_{\mathbf{k}+\mathbf{Q}\alpha}d^{\dagger}_{-\mathbf{k}-\mathbf{Q}\beta}\right] i\sigma^{y}_{\alpha\beta} + \text{H.c.}, \tag{5.4}$$

where $y_{\mathbf{k}} \equiv \alpha\cos 2\theta_{\mathbf{k}}$ and $y_{\mathbf{k}+\mathbf{Q}} \equiv \alpha\cos 2\theta_{\mathbf{k}+\mathbf{Q}}$.

Our goal is to analyze how accidental nodes on electron pockets evolve with increasing hybridization. For this we assume from the beginning that $|\alpha| > 1$ in which case the gaps on electron pockets have nodes when $y_{\mathbf{k}} = 1$ (for $c-$fermions) and $y_{\mathbf{k}+\mathbf{Q}} = -1$ for $d-$fermions.

To simplify the presentation, we fold the 1Fe BZ into the 2Fe BZ and replace the momentum $\mathbf{k}+\mathbf{Q}$ of d-fermions by $\mathbf{k}$. The momenta $\mathbf{k}$ below are defined as a deviation from $\mathbf{Q}$, which is the location of the electron pockets in the folded BZ.

In order to preserve the $\cos 2\theta_{\mathbf{k}}$ form of the gap function, we define $\theta_{\mathbf{k}}$ relative to the minor axis of the c pocket.

In the normal state, the inclusion of hopping via pnictogen/chalcogen atoms generates mixing between c and d fermions:

$$\mathcal{H}_{\lambda} = \sum_{\mathbf{k}} \left[\lambda_k c^{\dagger}_{\mathbf{k}\alpha}d_{\mathbf{k}\alpha} + \lambda^{*}_k d^{\dagger}_{\mathbf{k}\alpha}c_{\mathbf{k}\alpha}\right], \tag{5.5}$$

A microscopic derivation of $\lambda_{\mathbf{k}}$ shows [125, 205, 206, 207, 208, 203] that in 1111 systems (in which the configuration of pnictide atoms around every Fe layer is the same), $\lambda_{\mathbf{k}}$ vanishes along the lines $k_x = \pm k_y$ and has some weak k_z dependence. In 122 structures (in which the "above/below" configuration of pnictogen/chalcogen atoms is inverted from one Fe layer to the other), $\lambda_{\mathbf{k}}$ has minima but does not vanish along any direction. In the presence of a spin-orbit interaction $\lambda_{\mathbf{k}}$ does not have zeros even in 1111 systems [125, 205]. Because our goal is to understand the generic effect of the hybridization between the two bands, we will treat $\lambda_{\mathbf{k}}$ as a constant λ [205, 209, 210]. Earlier analysis of the effect of $\lambda_{\mathbf{k}}$ including its angular dependence (but without interplay with inter-pocket pairing) has shown that the results are qualitatively the same as for constant λ[203].

We next consider how hybridization affects the pairing terms. They can be subdivided into two types. Terms of the first type describe an interaction with excess

momentum $\mathbf{Q}$ between electron pockets and contain three fermionic operators from one pocket and one from the other pocket[140], e.g.,

$$\mathcal{H}_1 = \sum_{\mathbf{k},\mathbf{p},\mathbf{q}} u_1 \left[\left(c^\dagger_{\mathbf{k}\alpha} d_{\mathbf{k}-\mathbf{q},\alpha} + d^\dagger_{\mathbf{k}\alpha} c_{\mathbf{k}-\mathbf{q},\alpha} \right) \left(c^\dagger_{\mathbf{p}\beta} c_{\mathbf{p}+\mathbf{q},\beta} + d^\dagger_{\mathbf{p}\beta} d_{\mathbf{p}+\mathbf{q},\beta} \right) \right]. \tag{5.6}$$

Terms of the second type contain an interaction with excess momentum $\mathbf{Q}$ involving two fermions from a hole pocket and two from different electron pockets, e.g.,

$$\mathcal{H}_2 = \sum_{\mathbf{k},\mathbf{p},\mathbf{q},i} u_2 \left[\left(c^\dagger_{\mathbf{k}\alpha} h^i_{\mathbf{k}-\mathbf{q},\alpha} + h^{i\dagger}_{\mathbf{k}\alpha} c_{\mathbf{k}-\mathbf{q},\alpha} \right) \left(d^\dagger_{\mathbf{p}\beta} h^i_{\mathbf{p}+\mathbf{q},\beta} + h^{i\dagger}_{\mathbf{p}\beta} d_{\mathbf{p}+\mathbf{q},\beta} \right) \right], \tag{5.7}$$

where the operator $h^i_{\mathbf{p}\alpha}$ describes fermions near the i-th hole pocket. The two types of terms are different, yet their effect on the s^{+-} superconducting state is the same – both induce an additional pairing interaction between fermions belonging to different electron pockets. Indeed, in the superconducting state $\langle c^\dagger_{\mathbf{k}\alpha} c^\dagger_{-\mathbf{k}\beta} \rangle$, $\langle d^\dagger_{\mathbf{k}\alpha} d^\dagger_{-\mathbf{k}\beta} \rangle$, and $\langle h^{i\dagger}_{\mathbf{k}\alpha} h^{i\dagger}_{-\mathbf{k}\beta} \rangle$ are all non-zero. Decoupling four-fermion terms in (5.6) and (5.7) using these averages, we obtain anomalous quadratic terms involving c and d fermions:

$$\mathcal{H}_\beta = \frac{1}{2} \sum_{\mathbf{k}} \beta_{\mathbf{k}} \left[c^\dagger_{\mathbf{k}\alpha} d^\dagger_{-\mathbf{k}\beta} + d^\dagger_{\mathbf{k}\alpha} c^\dagger_{-\mathbf{k}\beta} \right] i\sigma^y_{\alpha\beta} + \text{H.c.}, \tag{5.8}$$

where $\beta_{\mathbf{k}}$ is given by

$$\begin{aligned} \beta_{\mathbf{k}} \equiv & \frac{1}{2} \sum_{\mathbf{p}} u_1(\mathbf{k},\mathbf{p}) (i\sigma^y)^\dagger_{\alpha'\beta'} \left[\left\langle c_{-\mathbf{p}\alpha'} c_{\mathbf{p}\beta'} \right\rangle + \left\langle d_{-\mathbf{p}\alpha'} d_{\mathbf{p}\beta'} \right\rangle \right] \\ & + \frac{1}{2} \sum_{\mathbf{p},i} u_2(\mathbf{k},\mathbf{p}) (i\sigma^y)^\dagger_{\alpha'\beta'} \left\langle h^i_{-\mathbf{p}\alpha'} h^i_{\mathbf{p}\beta'} \right\rangle . \end{aligned} \tag{5.9}$$

The coupling $\beta_{\mathbf{k}}$ is proportional to the magnitude of the s^{+-} gap Δ and has some non-singular angular dependence, determined by $u_1(\mathbf{k},\mathbf{p})$ and $u_2(\mathbf{k},\mathbf{p})$, which we can safely neglect.

We assume without loss of generality that the parameters Δ and λ are real and positive. The parameter $\beta \propto \Delta$ is then also real, but its sign can be either positive or negative.

Below we consider various ratios of λ/β and two FS geometries. In each case we compute the quasi-particle dispersion in the superconducting state and determine the position of the nodal points. In all cases we find two different dispersions: One is gapped over the entire BZ, while the other contains nodal points in a subset of the parameter space.

5.3 Circular pockets

As a warm-up, consider the limiting case when the two electron pockets are identical and have full rotational symmetry, i.e., $\xi^c_{\mathbf{k}} = \xi^f_{\mathbf{k}} \equiv \xi_{\mathbf{k}}$.

5.3.1 Inter-pocket pairing only ($\beta \neq 0$, $\lambda = 0$)

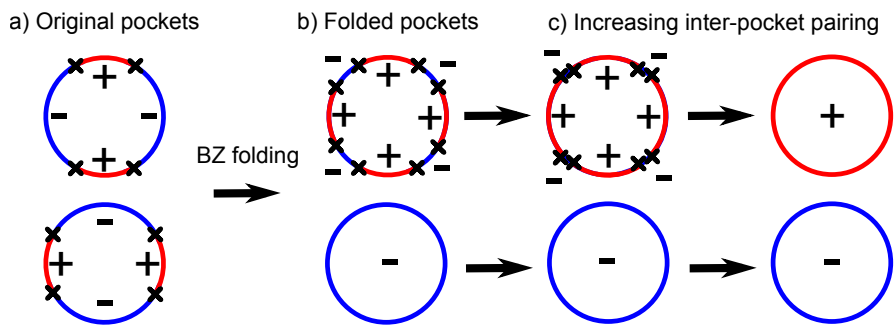

Figure 5.3: Gap structure for circular electron pockets with inter-pocket pairing. The crosses represent the location of the nodal points of the quasi-particle dispersions in the superconducting state. In a) and b) we show the unfolded and folded zones, respectively. In the folded zone, the pockets should overlap but we separate them for clarity. As we increase the inter-pocket pairing, keeping the conventional intra-pocket pairing fixed, the nodal points shift toward the diagonal lines $k_x = \pm k_y$, as seen in c). If the inter-pocket pairing reaches a critical value, the nodes merge and disappear, resulting in electron Fermi surfaces with opposite signs of the gap function.

In this special case, we find, after straightforward diagonalization of the quadratic form, that the two dispersions in the superconducting state are

$$\left(E^{\pm}_{\mathbf{k}}\right)^2 = \xi^2_{\mathbf{k}} + \left(\Delta \pm \sqrt{\Delta^2 y^2_{\mathbf{k}} + \beta^2}\right)^2, \tag{5.10}$$

where the expression in parenthesis represents an effective gap function. At $\beta = 0$, $E^+_{\mathbf{k}} = \pm\sqrt{\xi^2_{\mathbf{k}} + \Delta^2(1+|y_{\mathbf{k}}|)^2}$ and $E^-_{\mathbf{k}} = \pm\sqrt{\xi^2_{\mathbf{k}} + \Delta^2(1-|y_{\mathbf{k}}|)^2}$. This corresponds to the gap structure in the folded BZ: one band has no nodes and the other band has 8 nodes (see Fig. 5.3).

At $\beta \neq 0$, both dispersions evolve. The nodal points are still located on the FS (the locus of zero energy points in the normal state, given by $\xi_{\mathbf{k}} = 0$). The band with energy $E^+_{\mathbf{k}}$ is shifted up at a non-zero β and its effective gap function is definitely nodeless.

In contrast, the band with energy $E^-_{\mathbf{k}}$ is shifted down and the positions of the 8 nodes shift to

$$\cos(2\theta_{\mathbf{k}}) = \pm\frac{\sqrt{\Delta^2 - \beta^2}}{\alpha\Delta}. \tag{5.11}$$

As β increases, the nodal points move toward the diagonals $k_x = \pm k_y$, as shown in Fig. 5.3. At a critical value $\beta_c = \Delta$ they meet along the BZ diagonals. At larger $\beta > \beta_c$ the nodes disappear. At the same, because the nodes merge along the BZ diagonals, the sign of the gap on one FS is opposite to that on another FS. Such a gap structure has been obtained before in the analysis of possible gap configurations in LiFeAs both in orbital formalism and in band formalism [144, 204]. In the orbital formalism, such a state was termed "orbital antiphase" s^{+-} state[144].

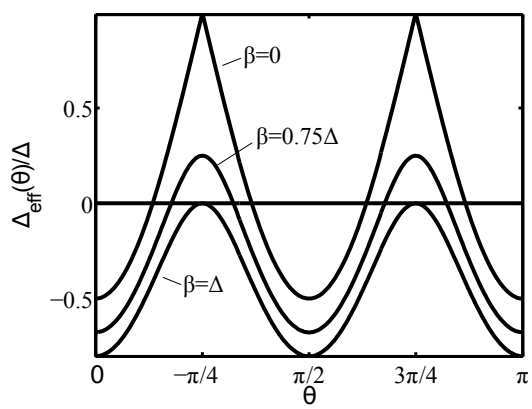

Figure 5.4: Nodal gap function with inter-pocket pairing β evaluated over the FS. As β increases, the function shifts downward and its zeroes move toward the angles $n\pi/2$, where n is an integer, which correspond to the directions given by $k_x = \pm k_y$. At $\beta = \Delta$, pairs of zeroes merge at those angles. For $\beta > \Delta$, the function is negative and has no zeroes.

An intuitive way to understand this behavior is the following: the gap function at the upper band is positive, while the one at the lower band has a roughly sinusoidal shape that crosses zero eight times, and its maxima occur at the diagonal directions $k_x = k_y$ and $k_x = -k_y$. As $|\beta|$ increases, the gap function shifts downward and thus the nodes move towards the BZ diagonals, until $|\beta|$ reaches the critical value β_c. At this point, pairs of nodal points meet and annihilate. At larger $|\beta| > \Delta$ the maxima of the gap function are located below zero, i.e., the gap is negative for all angles. This behavior is illustrated in Fig. 5.4.

5.3.2 Inter-pocket hopping only ($\lambda \neq 0$, $\beta = 0$)

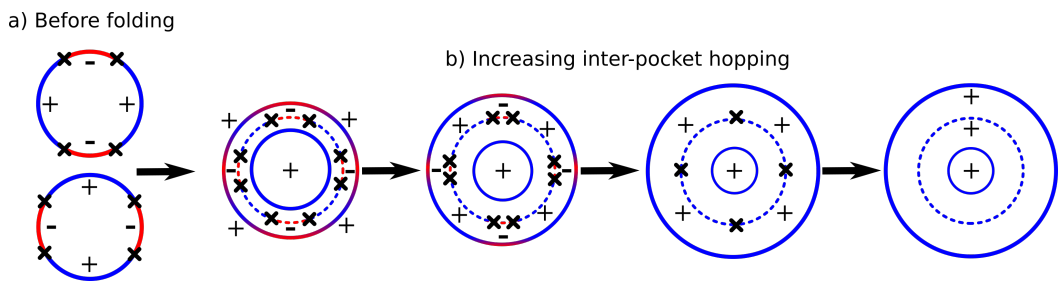

Figure 5.5: Gap structure for circular pockets with inter-pocket hopping. In a) and b) we show the unfolded and folded gap structure in the absence of hybridization, respectively. Inter-pocket hopping reconstructs the FSs as shown in c). The dashed line represents the original pockets, while the solid lines are the new set of two pockets. As the hopping parameter increases, the inner FS shrinks and the outer one becomes larger. In the superconducting state, the nodal points (represented as crosses) lie on the unhybridized FSs and shift toward the k_x and k_y axis as the hopping increases. At a critical value of this parameter the nodes meet and merge in pairs. For greater values of the parameter they vanish and the sign of the gap function becomes the same on both FSs. The separation between the FSs is purely schematic and has been exaggerated for clarity.

This case has been studied before,[203] and we briefly summarize the results for completeness. The hybridization of the electron pockets reconstructs the FSs. In order to study this effect we diagonalize the Hamiltonian $\mathcal{H}_0 + \mathcal{H}_\lambda$ by introducing new quasi-particles a and b via

$$c_{\mathbf{k}\alpha} = \frac{a_{\mathbf{k}\alpha} - b_{\mathbf{k}\alpha}}{\sqrt{2}}, \quad d_{\mathbf{k}\alpha} = \frac{a_{\mathbf{k}\alpha} + b_{\mathbf{k}\alpha}}{\sqrt{2}}. \tag{5.12}$$

After diagonalization, the non-pairing part of the Hamiltonian takes the form

$$\mathcal{H}_0' = \sum_{\mathbf{k}} \left[\xi^a_{\mathbf{k}} a^\dagger_{\mathbf{k}\alpha} a_{\mathbf{k}\alpha} + \xi^b_{\mathbf{k}} b^\dagger_{\mathbf{k}\alpha} b_{\mathbf{k}\alpha} \right], \tag{5.13}$$

where the dispersions are $\xi^a_{\mathbf{k}} = \xi_{\mathbf{k}} + \lambda$ and $\xi^b_{\mathbf{k}} = \xi_{\mathbf{k}} - \lambda$. The new FSs are concentric circles. The a pocket is smaller and the b pocket is larger than the unhybridized pockets.

In order to study the superconducting state, it is convenient to first rewrite $\mathcal{H}_\Delta$ in

terms of the new operators a and b as

$$\mathcal{H}'_\Delta = \frac{1}{2}\sum_{\mathbf{k}} \Delta \left[a^\dagger_{\mathbf{k}\alpha} a^\dagger_{-\mathbf{k}\beta} + b^\dagger_{\mathbf{k}\alpha} b^\dagger_{-\mathbf{k}\beta}\right] i\sigma^y_{\alpha\beta} \tag{5.14}$$
$$+ \frac{1}{2}\sum_{\mathbf{k}} \Delta y_{\mathbf{k}} \left[a^\dagger_{\mathbf{k}\alpha} b^\dagger_{-\mathbf{k}\beta} + b^\dagger_{\mathbf{k}\alpha} a^\dagger_{-\mathbf{k}\beta}\right] i\sigma^y_{\alpha\beta} + \text{H.c.}$$

Note that the inter-pocket pairing component $\Delta y_{\mathbf{k}}$ emerges. Diagonalizing the new Hamiltonian $\mathcal{H}'_0 + \mathcal{H}'_\Delta$, we find the two dispersions for the quasi-particles in the superconducting state given by

$$\left(E^\pm_{\mathbf{k}}\right)^2 = A_{\mathbf{k}} \pm \sqrt{B_{\mathbf{k}}}, \tag{5.15}$$

where

$$A_{\mathbf{k}} = \xi^2_{\mathbf{k}} + \Delta^2(1 + y^2_{\mathbf{k}}) + \lambda^2, \tag{5.16}$$
$$B_{\mathbf{k}} = 4\left[(\xi_{\mathbf{k}}\lambda)^2 + \Delta^2 y^2_{\mathbf{k}}(\Delta^2 + \lambda^2)\right], \tag{5.17}$$

The dispersion $E^+_{\mathbf{k}}$, as defined in (5.15), is positive for all $\mathbf{k}$ even when evaluated at $\Delta = 0$, so it has no locus of the nodal points. Both FS lines $\xi_{\mathbf{k}} = \pm\lambda$ in the normal state are part of the other dispersion $E^-_{\mathbf{k}}$. Once Δ becomes non-zero, one can easily check that E^-_k is non-zero along the normal state FSs. However, on the original, non-reconstructed FS,

$$E^-_{\mathbf{k}} = \sqrt{\Delta^2 + \lambda^2} - \Delta|y_{\mathbf{k}}| \tag{5.18}$$

This function contains 8 nodal points located at

$$\cos(2\theta_{\mathbf{k}}) = \pm\frac{\sqrt{\Delta^2 + \lambda^2}}{\alpha\Delta}. \tag{5.19}$$

As one increases λ, the nodes stay on the unhybridized FSs, but move toward the k_x or k_y axes (whichever is closer), until λ reaches a critical value $\lambda_c = \Delta\sqrt{\alpha^2 - 1}$. At this value of λ, pairs of nodal points merge and then disappear at larger λ. We show this schematically in Fig. 5.5.

The analysis of the signs of the gap requires some care. For $\lambda \gg \Delta$, the inter-pocket pairing term becomes irrelevant as the two reconstructed FSs are far apart from each other. In this limit, the gap on each reconstructed pocket is given by the fist line in (5.14) and is just Δ for both pockets. In this limit, the sign of the gap is indeed the same on both FSs. At intermediate λ, however, one cannot define the phase of the

gap function on the two FSs because in terms of the hybridized fermions the gap has contributions from both inter-pocket and inter-pocket condensates $\langle a_{\mathbf{k},\alpha} a_{-\mathbf{k},\beta}\rangle i\sigma^y_{\alpha\beta}$ and $\langle a_{\mathbf{k},\alpha} b_{-\mathbf{k},\beta}\rangle i\sigma^y_{\alpha\beta}$, respectively. Because the limiting behavior at large λ is known, it is "natural" to define both finite gaps with the same sign, as in Eq. (5.14), but we caution that this is rigorously justified only in the limit of very large λ.

5.3.3 Inter-pocket pairing and hopping ($\beta \neq 0$, $\lambda \neq 0$)

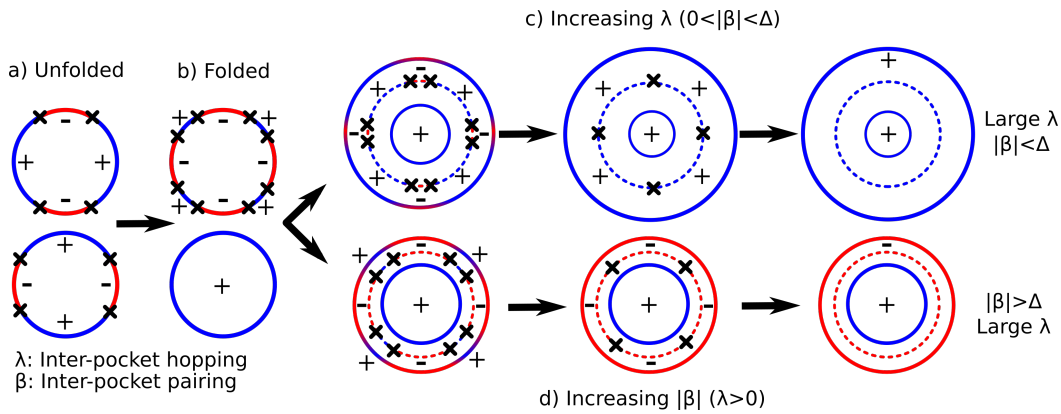

Figure 5.6: Gap structure for circular pockets with inter-pocket hopping and pairing interaction. The solid outer and inner circles represent the reconstructed FSs after hybridization. In the superconducting state, the nodal points (represented as crosses) lie on a circle (dashed line) but no longer on the unhybridized Fermi surface. As the hopping parameter λ increases, the nodes move toward the k_x and k_y axis, where they can merge and disappear. In this scenario the gap function has the same sign on both electron pockets. Increasing the pairing strength β shifts the nodes toward the diagonal lines $k_x = \pm k_y$ instead. The nodes can merge and vanish, in which case the gap function acquires opposite signs on the outer and inner pockets.

Once more, the first step is to diagonalize the Hamiltonian $\mathcal{H}_0 + \mathcal{H}_\lambda$ by introducing new pockets a and b exactly as in the case with $\beta = 0$. We then rewrite the remaining Hamiltonian in terms of the a and b operators and obtain

$$\begin{aligned}\mathcal{H}'_{\Delta+\beta} = \frac{1}{2}\sum_{\mathbf{k}} \left[(\Delta+\beta) a^\dagger_{\mathbf{k}\alpha} a^\dagger_{-\mathbf{k}\beta} + (\Delta-\beta) b^\dagger_{\mathbf{k}\alpha} b^\dagger_{-\mathbf{k}\beta}\right] i\sigma^y_{\alpha\beta} \\ + \frac{1}{2}\sum_{\mathbf{k}} \Delta y_{\mathbf{k}} \left[a^\dagger_{\mathbf{k}\alpha} b^\dagger_{-\mathbf{k}\beta} + b^\dagger_{\mathbf{k}\alpha} a^\dagger_{-\mathbf{k}\beta}\right] i\sigma^y_{\alpha\beta} + \text{H.c.}\end{aligned} \tag{5.20}$$

Observe that the coefficient β appears only in the intra-pocket terms. We diagonalize the Hamiltonian $\mathcal{H}_0' + \mathcal{H}_{\Delta+\beta}'$ and again find dispersions of the form $E_{\mathbf{k}}^{\pm} = \sqrt{A_{\mathbf{k}} \pm \sqrt{B_{\mathbf{k}}}}$, where

$$A_{\mathbf{k}} = \xi_{\mathbf{k}}^2 + \Delta^2(1 + y_{\mathbf{k}}^2) + \lambda^2 + \beta^2, \tag{5.21}$$

$$B_{\mathbf{k}} = 4\left[(\xi_{\mathbf{k}}\lambda + \Delta\beta)^2 + \Delta^2 y_{\mathbf{k}}^2(\Delta^2 + \lambda^2)\right]. \tag{5.22}$$

The dispersion $E_{\mathbf{k}}^{+}$ is fully gapped, but $E_{\mathbf{k}}^{-}$ has nodal points at momenta given by

$$\xi_{\mathbf{k}} = \lambda\beta/\Delta, \tag{5.23}$$

$$\cos 2\theta_{\mathbf{k}} = \pm\frac{\sqrt{\Delta^2 + \lambda^2 - \beta^2 - \lambda^2\beta^2/\Delta^2}}{\alpha\Delta}. \tag{5.24}$$

Note that the nodal points are now shifted from the unhybridized FS. The direction of the shift depends on the sign of β. If $\beta > 0$ ($\beta < 0$) the nodes appear between the original FSs (the ones before hybridization) and the outer (inner) hybridized FS. The nodes exist in the parameter range given by

$$0 \leq \Delta^2 + \lambda^2 - \beta^2 - \lambda^2\beta^2/\Delta^2 \leq \alpha^2\Delta^2. \tag{5.25}$$

The lower bound is reached when we keep λ fixed and increase $|\beta|$ towards critical $\beta_c = \Delta$. In this case the nodes merge at the diagonals $k_x = k_y$ or $k_x = -k_y$. The nodes disappear when $|\beta| > \beta_c$ and the intra-pocket gap components in the first line of Eq. (5.20) have different signs. In the limit of $\lambda \gg \Delta$, the inter-pocket gap component becomes irrelevant since the reconstructed FSs are far apart and in this sense the gap function has opposite signs on the two electron pockets.

The upper boundary in (5.25) is reached when we set $|\beta| < \Delta$ and increase λ. In this situation the nodes merge along the k_x and k_y directions at a critical value of λ given by

$$\lambda_c = \Delta\sqrt{\frac{(\alpha^2 - 1)\Delta^2 + \beta^2}{\Delta^2 - \beta^2}}. \tag{5.26}$$

At $\lambda > \lambda_c$, the nodes disappear and the gap function has the same sign on each electron pocket, as can be clearly seen in the limit of $\lambda \gg \Delta$. Note that λ_c grows with β, i.e., the inter-pocket pairing allows the nodes to exist in a greater range of values of λ. In this sense the pairing partially protects the nodes from disappearing due to hopping, as long

as $|\beta| < \Delta$. The behavior of the nodes when both λ and β are present is summarized in Fig. 5.6.

Since the limiting cases where β or λ are large yield different results for the relative signs of the gap function on the electron pockets, it is interesting to see how one may go from one limit to the other. Consider first a situation where $\beta = 0$ and $\lambda > \lambda_c$ (the fully gapped state with equal signs of the gaps on the two electron FSs). Now increase β. When β gets larger, λ_c increases and tends to infinity when β approaches Δ (see Eq. (5.26)). Accordingly, once β exceeds some threshold, λ_c become larger than λ and the nodal points reappear along k_x and k_y directions. As β continues to increase, the nodes split, shift toward the diagonal lines $k_x = \pm k_y$, merge there at $\beta = \Delta$, and disappear when $\beta > \Delta$, resulting in the fully-gapped state where the signs of the gaps on the two Fermi surfaces are opposite. If instead one departs from $\lambda = 0$ and $\beta > \Delta$, then increasing λ reconstructs the FSs but cannot cause the nodal points to reappear. Thus one cannot go back to the state with same signs on the FSs as long as $\beta > \Delta$. Instead, one would need to decrease Δ, reversing the process described above.

5.4 Elliptical pockets

Now we consider the more realistic case where the electron pockets are elliptical. We will take the dispersions in the form

$$\xi^c_{\mathbf{k}} = -\mu + \frac{k_x^2}{2m_1} + \frac{k_y^2}{2m_2}, \tag{5.27}$$

$$\xi^d_{\mathbf{k}} = -\mu + \frac{k_x^2}{2m_2} + \frac{k_y^2}{2m_1}. \tag{5.28}$$

It is convenient to rewrite the dispersions as $\xi^{c,d}_{\mathbf{k}} = \xi_{\mathbf{k}} \pm \delta_{\mathbf{k}} \cos 2\theta_{\mathbf{k}}$, where the + sign corresponds to $\xi^c_{\mathbf{k}}$, $\xi_{\mathbf{k}} \equiv (\xi^c_{\mathbf{k}} + \xi^d_{\mathbf{k}})/2$, and $\delta_{\mathbf{k}} \equiv \mathbf{k}^2(m_1^{-1} - m_2^{-1})/4$. Without loss of generality, we will take $\delta_{\mathbf{k}}$ to be positive.

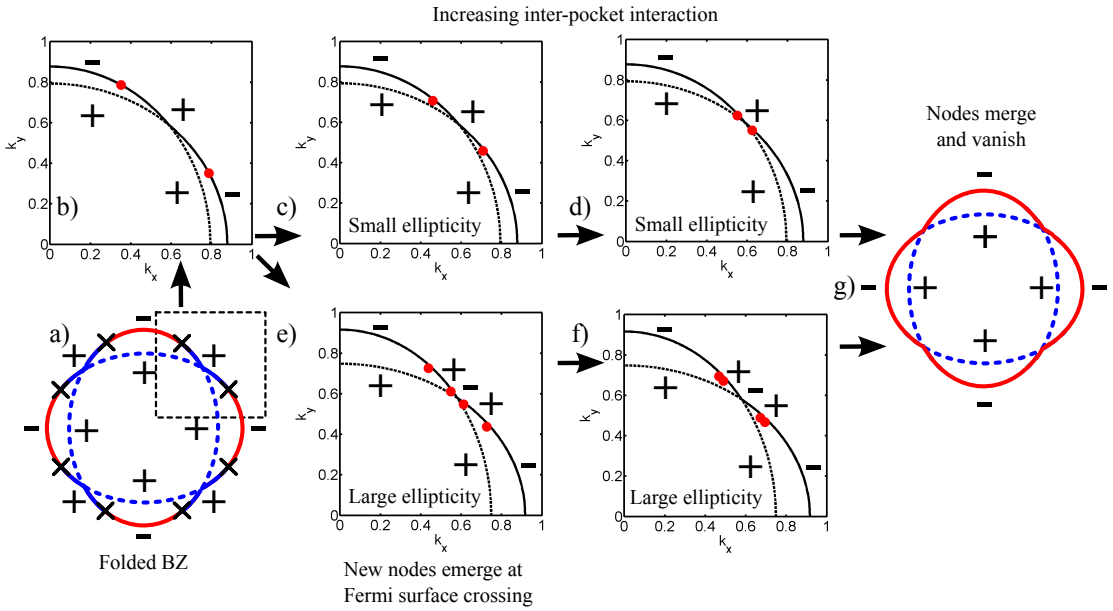

Figure 5.7: Gap structure for elliptical pockets with inter-pocket pairing. In a) we show the folded electron pockets overlapping. The crosses indicate the position of the nodal points, while the solid and dashed lines indicate opposite signs of the gap function. The evolution of the nodal points as obtained by a numerical calculation is shown in b) through f). First, b) shows the nodal points with no hybridization. If the ellipticity is below a threshold, increasing the inter-pocket pairing simply shifts the nodes toward the diagonal lines $k_x = \pm k_y$ as seen in c) and d). The nodes merge and disappear after reaching the diagonal lines and the gap structure becomes nodeless as shown in g). If this occurs, the gap function has opposite signs on the inner and outer edges of the FSs. Alternatively, if the ellipticity is higher than the threshold, the nodes do not reach the diagonal lines, but instead a node emerges at that symmetry point. As we further increase the inter-pocket pairing the node splits into two nodes which move toward the original nodes, as shown in e) and f). Eventually, the new and old nodes meet and merge, resulting again in the structure shown in g).

5.4.1 Inter-pocket pairing only ($\beta \neq 0$, $\lambda = 0$)

The dispersions after diagonalizing the Hamiltonian are given by $(E^{\pm}_{\mathbf{k}})^2 = A_{\mathbf{k}} \pm \sqrt{B_{\mathbf{k}}}$, where

$$A_{\mathbf{k}} = \frac{1}{2}\Big[(\xi^c_{\mathbf{k}})^2 + (\xi^d_{\mathbf{k}})^2 + 2\Delta^2(1 + y^2_{\mathbf{k}}) + 2\beta^2\Big], \tag{5.29}$$

$$B_{\mathbf{k}} = \frac{1}{4}\Big[\left((\xi^d_{\mathbf{k}})^2 - (\xi^c_{\mathbf{k}})^2 + 4\Delta^2 y_{\mathbf{k}}\right)^2 + 4|\beta|^2\left((\xi^c_{\mathbf{k}} - \xi^d_{\mathbf{k}})^2 + 4\Delta^2\right)\Big]. \tag{5.30}$$

Once again, $E^+_{\mathbf{k}}$ is fully gapped but $E^-_{\mathbf{k}}$ may contain nodes. Unlike the circular case, the nodes are not located on the original FSs, but at momenta $|\mathbf{k}|$ which are solutions of

$$(\delta_{\mathbf{k}} + \alpha\xi_{\mathbf{k}})\left(\xi_{\mathbf{k}}\delta_{\mathbf{k}} - \alpha\Delta^2\right) + \alpha\beta^2\delta_{\mathbf{k}} = 0. \tag{5.31}$$

Let the solutions to this equation be $\xi_{\mathbf{k}} = \bar{\xi}$ and $\delta_{\mathbf{k}} = \bar{\delta}$. The angular positions of the nodal points are given by

$$\cos^2 2\theta_{\mathbf{k}} = \frac{F(\bar{\xi}, \bar{\delta})}{(\bar{\delta}^2 + \alpha^2\Delta^2)^2}, \tag{5.32}$$

where

$$\begin{aligned} F(\bar{\xi}, \bar{\delta}) = &\left(\bar{\delta}^2 - \alpha^2\Delta^2\right)\left(\bar{\xi}^2 + \beta^2 - \Delta^2\right) \\ &- 4\alpha\Delta^2\bar{\xi}\bar{\delta}. \end{aligned} \tag{5.33}$$

Note that for each solution to Eq. (5.31) there exist 8 nodal points in the dispersion. One may solve for $\bar{\xi}$ and $\bar{\delta}$ exactly but the solution is not very illuminating. It is more useful to solve for $\bar{\xi}$ in terms of $\bar{\delta}$ and analyze how the nodal points evolve when we change $\bar{\delta}$. Expressing $\bar{\xi}$ in terms of $\bar{\delta}$ we obtain

$$\bar{\xi} = \frac{\bar{\delta}^2 - \alpha^2\Delta^2 \pm \sqrt{\left(\alpha^2\Delta^2 + \bar{\delta}^2\right)^2 - 4\alpha^2\beta^2\bar{\delta}^2}}{2\alpha\bar{\delta}}. \tag{5.34}$$

Substitution of these solutions into Eq. (5.33) yields

$$\cos^2 2\theta_{\mathbf{k}} = \frac{\bar{\delta}^2 - \alpha^2\Delta^2 \mp \sqrt{\left(\alpha^2\Delta^2 + \bar{\delta}^2\right)^2 - 4\alpha^2\beta^2\bar{\delta}^2}}{2\alpha^2\bar{\delta}^2} \tag{5.35}$$

Analyzing (5.35) we find new interesting physics. Namely, depending on the parameters, there may be 0, 8, or 16 nodal points in the dispersion. When $\bar{\delta} < \alpha\Delta$, there are

either 8 or zero nodes, as one can immediately verify. At small β, there are 8 nodes. As $|\beta|$ increases, the nodes move toward the diagonals $k_x = \pm k_y$, like in the circular case. At $|\beta| = \Delta$, pairs of nodes merge, and for $|\beta| > \Delta$ they disappear. The outcome of the disappearance of the nodes is the effective s^{+-} superconducting state with different signs of the gap on the inner and outer electron pockets, see Fig. 5.7.

When $\bar{\delta} > \alpha\Delta$, the evolution of the nodes is more interesting. At small β, there are again 8 nodes. As $|\beta|$ increases, the nodes shift towards diagonals but they do not reach $k_x = \pm k_y$ at $|\beta| = \Delta$. Instead, at this β, a new quadratic node appears in in each quadrant at the point where zone diagonals intersect the original FS. At $|\beta| > \Delta$, each quadratic node splits into two, one to the right and one to the left of a diagonal, and each new node moves toward the already existing nodes (see Fig. 5.7). Thus, there is a total of 16 nodal points. As $|\beta|$ continues increasing, the old and new nodes merge at a critical value $|\beta| = \beta_c$ given by

$$\beta_c = \left(\alpha^2\Delta^2 + \bar{\delta}^2\right)/(2|\alpha|\bar{\delta}). \tag{5.36}$$

The nodes disappear when $|\beta|$ exceeds this critical value and the end result of the evolution of the nodes is the same minus-plus gap on the inner and outer electron pockets.

We verified this behavior numerically (Fig. 5.7 actually shows the results of numerical calculations). In all numerical examples here and below we have set $\mu = 10\Delta$ and $\alpha = -1.5$. Note in passing that while the relationships presented in this analysis are exact, one must keep in mind that in general $\bar{\delta}$ by itself depends on β.

5.4.2 Inter-pocket hopping only ($\lambda \neq 0$, $\beta = 0$)

This case has been studied before [203] and we present it here for completeness, using a somewhat different computation scheme. The first step is to diagonalize the Hamiltonian $\mathcal{H}_0 + \mathcal{H}_\lambda$ by introducing new operators a and b such that

$$\begin{aligned} c_{\mathbf{k}\alpha} &= u_{\mathbf{k}} a_{\mathbf{k}\alpha} + v_{\mathbf{k}} b_{\mathbf{k}\alpha}, \\ d_{\mathbf{k}\alpha} &= -v_{\mathbf{k}} a_{\mathbf{k}\alpha} + u_{\mathbf{k}} b_{\mathbf{k}\alpha}, \end{aligned} \tag{5.37}$$

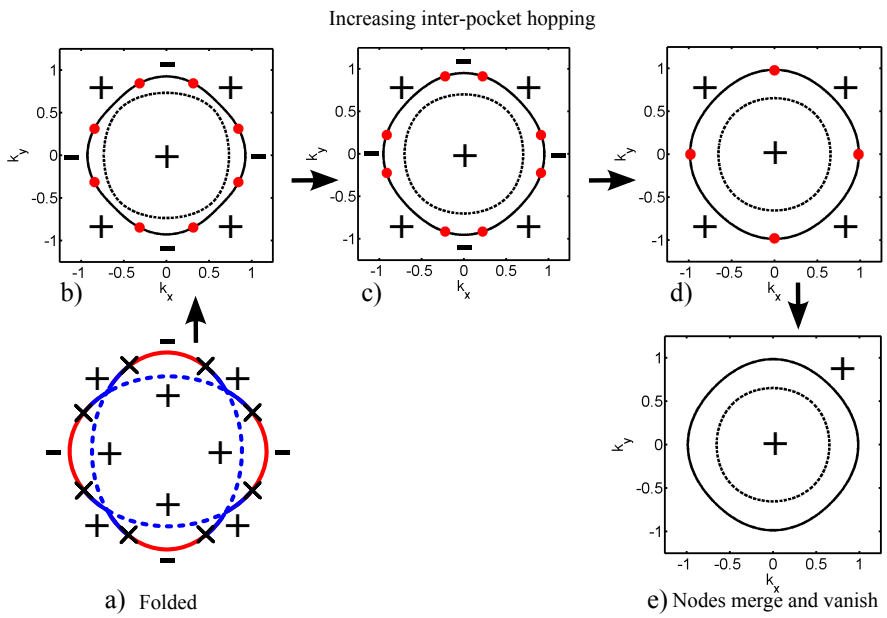

Figure 5.8: Gap structure for elliptical pockets with inter-pocket hopping. In a) we show the gap structure in the absence of hybridization. Inter-pocket hopping reconstructs the FSs as shown in b). As the hopping parameter increases, the inner FS shrinks and the outer one becomes larger. In the superconducting state, the nodal points (represented as crosses) lie near, but not exactly on FSs and shift toward the k_x and k_y axis as the hopping increases, as shown in b) and c). At a critical value of the hopping the nodes meet and merge in pairs as in d). Finally, for greater values of the parameter they vanish and the sign of the gap function becomes the same on both FSs. Subfigures b) through e) are the result of numerical calculations.

where $u_{\mathbf{k}} = \cos\psi$ and $v_{\mathbf{k}} = -\sin\psi$, and this angle ψ satisfies

$$\cos 2\psi = (\xi^c_{\mathbf{k}} - \xi^d_{\mathbf{k}})/\sqrt{(\xi^c_{\mathbf{k}} - \xi^d_{\mathbf{k}})^2 + 4\lambda^2}, \tag{5.38}$$

$$\sin 2\psi = 2\lambda/\sqrt{(\xi^c_{\mathbf{k}} - \xi^d_{\mathbf{k}})^2 + 4\lambda^2}. \tag{5.39}$$

The new Hamiltonian is

$$\mathcal{H}'_0 = \sum_{\mathbf{k}} \left[\xi^a_{\mathbf{k}} a^\dagger_{\mathbf{k}\alpha} a_{\mathbf{k}\alpha} + \xi^b_{\mathbf{k}} b^\dagger_{\mathbf{k}\alpha} b_{\mathbf{k}\alpha}\right], \tag{5.40}$$

where $\xi^{a,b}_{\mathbf{k}} = \frac{1}{2}(\xi^c_{\mathbf{k}} + \xi^d_{\mathbf{k}}) \pm \sqrt{\lambda^2 + (\xi^c_{\mathbf{k}} - \xi^d_{\mathbf{k}})^2/4}$. These new dispersions define the reconstructed FSs shown in Fig. 5.8. As the hopping parameter λ increases, the outer FS (associated with b fermions) becomes larger, while the inner FS (associated with a fermions) shrinks.

Now we consider the superconducting state. Rewriting the pairing part of the Hamiltonian in terms of the new operators we find

$$\begin{aligned}\mathcal{H}'_\Delta = &\frac{1}{2}\sum_{\mathbf{k}} \left[\Delta(1 - f_{\mathbf{k}} y_{\mathbf{k}}) a^\dagger_{\mathbf{k}\alpha} a^\dagger_{-\mathbf{k}\beta} + \Delta(1 + f_{\mathbf{k}} y_{\mathbf{k}}) b^\dagger_{\mathbf{k}\alpha} b^\dagger_{-\mathbf{k}\beta}\right] i\sigma^y_{\alpha\beta} \\ &- \frac{1}{2}\sum_{\mathbf{k}} \Delta g_{\mathbf{k}} y_{\mathbf{k}} \left[a^\dagger_{\mathbf{k}\alpha} b^\dagger_{-\mathbf{k}\beta} + b^\dagger_{\mathbf{k}\alpha} a^\dagger_{-\mathbf{k}\beta}\right] i\sigma^y_{\alpha\beta} + \text{H.c.},\end{aligned} \tag{5.41}$$

where $f_{\mathbf{k}} \equiv \cos 2\psi$ and $g_{\mathbf{k}} \equiv -\sin 2\psi$. The diagonalization of this Hamiltonian again yields dispersions in the superconducting state in the form $(E^\pm_{\mathbf{k}})^2 = A_{\mathbf{k}} \pm \sqrt{B_{\mathbf{k}}}$. In this particular case

$$A_{\mathbf{k}} = \frac{1}{2}\left[(\xi^a_{\mathbf{k}})^2 + (\xi^b_{\mathbf{k}})^2 + 2\Delta^2(1 + y^2_{\mathbf{k}})\right], \tag{5.42}$$

$$B_{\mathbf{k}} = \frac{1}{4}\left[\left((\xi^b_{\mathbf{k}})^2 - (\xi^a_{\mathbf{k}})^2 + 4\Delta^2 f_{\mathbf{k}} y_{\mathbf{k}}\right)^2 + 4\Delta^2 y^2_{\mathbf{k}} g^2_{\mathbf{k}} \left((\xi^a_{\mathbf{k}} - \xi^b_{\mathbf{k}})^2 + 4\Delta^2\right)\right]. \tag{5.43}$$

As usual, the dispersion $E^+_{\mathbf{k}}$ is nodeless, but $E^-_{\mathbf{k}}$ has nodes at momenta which are the solutions of the equation

$$(\delta_{\mathbf{k}} + \alpha\xi_{\mathbf{k}})\left(\xi_{\mathbf{k}}\delta_{\mathbf{k}} - \alpha\Delta^2\right) - \alpha\lambda^2\delta_{\mathbf{k}} = 0. \tag{5.44}$$

Each solution to this equation defines a pair $(\bar{\xi}, \bar{\delta})$ and determines the radial position of the nodal point. The angular position is then given by

$$\cos^2 2\theta_{\mathbf{k}} = \frac{F(\bar{\xi}, \bar{\delta})}{(\bar{\delta}^2 + \alpha^2\Delta^2)^2}, \tag{5.45}$$

where

$$F(\bar{\xi},\bar{\delta}) = \left(\bar{\delta}^2 - \alpha^2\Delta^2\right)\left(\bar{\xi}^2 - \lambda^2 - \Delta^2\right) - 4\alpha\Delta^2\bar{\xi}\bar{\delta}. \tag{5.46}$$

Like before, we solve for $\bar{\xi}$ in terms of $\bar{\delta}$. The solution is

$$\bar{\xi} = \frac{-\bar{\delta}^2 + \alpha^2\Delta^2 - \sqrt{\left(\alpha^2\Delta^2 + \bar{\delta}^2\right)^2 + 4\alpha^2\lambda^2\bar{\delta}^2}}{2\alpha\bar{\delta}}. \tag{5.47}$$

When we substitute this solution into Eq. (5.45) we find that the angular position of the nodes is given by

$$\cos^2 2\theta_{\mathbf{k}} = \frac{\bar{\delta}^2 - \alpha^2\Delta^2 + \sqrt{\left(\alpha^2\Delta^2 + \bar{\delta}^2\right)^2 + 4\alpha^2\lambda^2\bar{\delta}^2}}{2\alpha^2\bar{\delta}^2}. \tag{5.48}$$

The analysis of these equations shows that nodal points appear in a set of 8 and that they are not located on the FSs of the normal state, although our numerical calculations show that they remain very close to it. The location of the nodes with respect to the original FSs varies depending on the sign of α. If $\alpha > 0$, the nodes are located inside of both unhybridized FSs but outside of the smaller FS. Instead, if $\alpha < 0$ the nodes are outside the unhybridized FSs but inside the larger reconstructed FS.

In both cases, the behavior is qualitatively the same as in the limiting case of circular pockets and is summarized in Fig. 5.8, where we show the result of numerical calculations. Increasing λ shifts the nodes toward the k_x and k_y axes. The critical value of λ that causes the nodes to merge along these directions is enhanced by the ellipticity and is given by $\lambda_c = \sqrt{\left(\Delta^2 + \bar{\delta}^2\right)(\alpha^2 - 1)}$. At any larger λ the nodes disappear. In this sense, the eccentricity of the pockets tries to prevent the disappearance of the nodes.

Regarding the gap structure, we note that for large λ the inter-pocket pairing term is irrelevant as the reconstructed FSs are far apart from each other. In this limit, the gap on the reconstructed pockets is given by $\Delta(1 \pm f_{\mathbf{k}} y_{\mathbf{k}})$, where $|f_{\mathbf{k}} y_{\mathbf{k}}| \ll 1$. Thus, the phase of the gap function is equal and uniform over the the reconstructed FSs.

At smaller λ, the phase of the gap along the FSs cannot be determined as the pairing involves both intra-pocket and inter-pocket terms. Judging from the large λ limit, it seems natural to define the gap with equal sign on both FSs also at intermediate λ, see Fig. 5.8.

5.4.3 Inter-pocket pairing and hopping ($\beta \neq 0$, $\lambda \neq 0$)

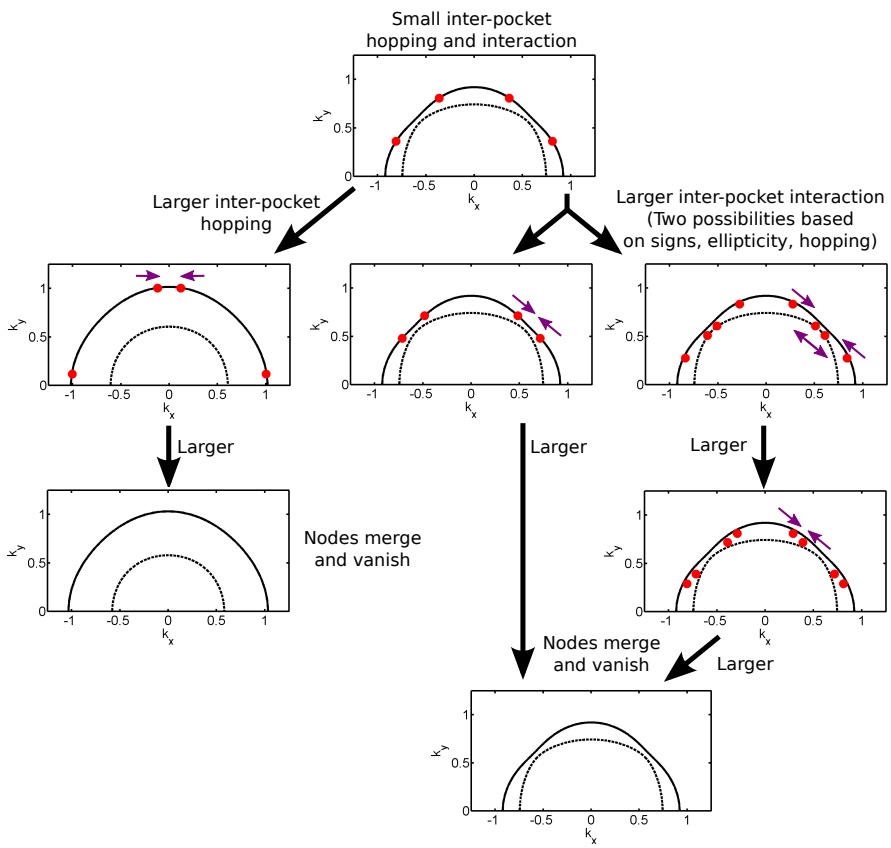

Figure 5.9: Gap structure for elliptical pockets with inter-pocket hopping and pairing. This case incorporates all the features seen in Figs. 5.7 and 5.8. The main difference is that the condition for additional nodes does not depend solely on the ellipticity, but also on the hopping parameter and the sign of the inter-pocket pairing.

This case is the most generic one. Like before, we switch to the reconstructed a and b pockets after hybridization. The pairing terms in the Hamiltonian can be rewritten in terms of a and b operators and take the form

$$\begin{aligned}\mathcal{H}'_{\Delta+\beta} = \frac{1}{2}\sum_{\mathbf{k}} \left[\Delta_{aa}(\mathbf{k}) a^{\dagger}_{\mathbf{k}\alpha} a^{\dagger}_{-\mathbf{k}\beta} + \Delta_{bb}(\mathbf{k}) b^{\dagger}_{\mathbf{k}\alpha} b^{\dagger}_{-\mathbf{k}\beta}\right] i\sigma^{y}_{\alpha\beta} \\ + \frac{1}{2}\sum_{\mathbf{k}} \Delta_{ab}(\mathbf{k}) \left[a^{\dagger}_{\mathbf{k}\alpha} b^{\dagger}_{-\mathbf{k}\beta} + b^{\dagger}_{\mathbf{k}\alpha} a^{\dagger}_{-\mathbf{k}\beta}\right] i\sigma^{y}_{\alpha\beta} + \text{H.c.},\end{aligned} \tag{5.49}$$

where

$$\Delta_{aa}(\mathbf{k}) = \Delta(1 - y_{\mathbf{k}} f_{\mathbf{k}}) - \beta g_{\mathbf{k}}, \tag{5.50}$$

$$\Delta_{bb}(\mathbf{k}) = \Delta(1 + y_{\mathbf{k}} f_{\mathbf{k}}) + \beta g_{\mathbf{k}}, \tag{5.51}$$

$$\Delta_{ab}(\mathbf{k}) = -\Delta y_{\mathbf{k}} g_{\mathbf{k}} + \beta f_{\mathbf{k}}. \tag{5.52}$$

The dispersions are given by $(E^{\pm}_{\mathbf{k}})^2 = A_{\mathbf{k}} \pm \sqrt{B_{\mathbf{k}}}$, where

$$A_{\mathbf{k}} = \frac{1}{2}\Big[(\xi^a_{\mathbf{k}})^2 + \left(\xi^b_{\mathbf{k}}\right)^2 + 2\Delta^2 \left(1 + y^2_{\mathbf{k}}\right) + 2\beta^2 \Big], \tag{5.53}$$

$$\begin{aligned} B_{\mathbf{k}} =& \frac{1}{4}\Big[\left(\left(\xi^b_{\mathbf{k}}\right)^2 - (\xi^a_{\mathbf{k}})^2 + 4\Delta^2 f_{\mathbf{k}} y_{\mathbf{k}} \right)^2 \\ & + 4\Delta^2 y^2_{\mathbf{k}} g^2_{\mathbf{k}} \left((\xi^a_{\mathbf{k}} - \xi^b_{\mathbf{k}})^2 + 4\Delta^2 \right) \Big] \\ & -2\beta\Delta g_{\mathbf{k}} \left(\xi^a_{\mathbf{k}} - \xi^b_{\mathbf{k}}\right) \left[\xi^a_{\mathbf{k}} + \xi^b_{\mathbf{k}} + \left(\xi^a_{\mathbf{k}} - \xi^b_{\mathbf{k}}\right) f_{\mathbf{k}} y_{\mathbf{k}} \right] \\ & +\beta^2 \left[4\Delta^2 + \left(\xi^a_{\mathbf{k}} - \xi^b_{\mathbf{k}}\right)^2 f^2_{\mathbf{k}} \right]. \end{aligned} \tag{5.54}$$

Once more, we search for nodes in the dispersion $E^-_{\mathbf{k}}$. The radial position of the nodes is determined by the condition

$$\left(\delta_{\mathbf{k}}\xi_{\mathbf{k}} - \alpha\Delta^2\right)\left(\delta_{\mathbf{k}} + \alpha\xi_{\mathbf{k}}\right) + \frac{\beta\lambda}{\Delta}\left(\alpha^2\Delta^2 - \delta^2_{\mathbf{k}}\right) + \alpha\left(\beta^2 - \lambda^2\right)\delta_{\mathbf{k}} = 0. \tag{5.55}$$

The solutions to this equation $(\bar{\xi}, \bar{\delta})$ are needed to find the angular position of the nodes:

$$\cos^2 2\theta_{\mathbf{k}} = \frac{F(\bar{\xi}, \bar{\delta})}{(\bar{\delta}^2 + \alpha^2\Delta^2)^2}, \tag{5.56}$$

where

$$F(\bar{\xi}, \bar{\delta}) = \left(\bar{\delta}^2 - \alpha^2\Delta^2\right)\left(\bar{\xi}^2 + \beta^2 - \lambda^2 - \Delta^2\right) + 4\alpha\Delta\bar{\delta}\left(\beta\lambda - \Delta\bar{\xi}\right). \tag{5.57}$$

Solving for $\bar{\xi}$ in terms of $\bar{\delta}$, we find that the solutions to Eq. (5.55) are

$$\bar{\xi} = \frac{1}{2\alpha\bar{\delta}}\left\{ -\bar{\delta}^2 + \alpha^2\Delta^2 \pm \left[\left(\alpha^2\Delta^2 + \bar{\delta}^2\right)^2 + 4\alpha\bar{\delta}\left(\left(\bar{\delta}^2 - \alpha^2\Delta^2\right)\frac{\lambda\beta}{\Delta} + \alpha\bar{\delta}\left(\lambda^2 - \beta^2\right) \right) \right]^{1/2} \right\}. \tag{5.58}$$

The angular location of the nodes for these solutions is given by

$$\cos^2 2\theta_{\mathbf{k}} = \frac{1}{2\alpha^2\bar{\delta}^2}\Bigg\{\bar{\delta}^2 - \alpha^2\Delta^2 + 2\alpha\delta\beta\lambda/\Delta \\ \mp \left[\left(\alpha^2\Delta^2 + \bar{\delta}^2\right)^2 + 4\alpha\bar{\delta}\left(\left(\bar{\delta}^2 - \alpha^2\Delta^2\right)\frac{\lambda\beta}{\Delta} + \alpha\bar{\delta}\left(\lambda^2 - \beta^2\right)\right)\right]^{1/2}\Bigg\}. \tag{5.59}$$

In this general case the interplay of the different parameters is considerably more complicated than in the previous limiting cases, but it does not produce any new features. We find that in general the position of the nodal points depends on the signs of both β and α, not only their magnitudes. The dependence on the sign of β comes from bilinear terms of the form $\beta\lambda$, while the dependence on the sign of α is a consequence of the ellipticity of the pockets.

The general behavior of the nodal points is summarized in Fig. 5.9. We found by numerical analysis that in general increasing λ tends to shift the nodes toward the k_x and k_y axis as usual, where they merge and disappear at a critical value of λ. In this case, the sign of the order parameter is the same on both FSs. Increasing $|\beta|$ instead shifts the nodes toward the diagonals $k_x = \pm k_y$. At $|\beta| = \Delta$ there are two possibilities, as seen in the limiting case of $\lambda = 0$. The first is that the eight nodal points merge in pairs at the diagonal lines, disappearing for $|\beta| > \Delta$.

This happens at small $\bar{\delta}$, i.e., for small eccentricity. The second is that the original nodal points do not reach the diagonal lines at this value of β, but instead four new nodes appear at those lines. Increasing $|\beta|$ further causes these four new nodal points to split into pairs, and moves the old and new nodes toward each other. At a threshold value of β they merge and then disappear. This second scenario, with 16 nodal points at intermediate β, is realized at larger $\bar{\delta}$, i.e., at larger eccentricity. In either case, the merging of nodes caused by large β means that the gap function has opposite signs on the electron pockets.

One important difference with the case of $\lambda = 0$ is that the condition for developing additional nodal points is more complicated since the sign of β and the value of λ also play a role. It is clear from the equations that the additional nodes are more likely to develop for $\beta < 0$, for $\delta > \alpha\Delta$ and for small λ. The exact conditions when additional nodes appear are given by rather involved formulas and we refrain from presenting them.

5.5 Summary

In this chapter we have investigated the effect of hybridization of the two electron pockets on the gap structure in FeSCs. We considered the case when the dominant pairing interaction is between hole and electron pockets and it yields an s^{+-} gap with accidental nodes on the electron pockets. Our goal was to understand how accidental nodes move once we include the hybridization. We argued that for an s^{+-} superconductor hybridization gives rise to two effects – hopping between electron FSs and the appearance of an additional pairing term which describes inter-pocket pairing. Each of these two effects shifts the position of the nodes and at large enough hybridization the nodes eventually disappear. However, the evolution of the nodes and the gap structure of the resulting nodeless state is different, depending on whether the inter-pocket hopping or the inter-pocket interaction is stronger. In the first case, the resulting state has the same sign of the gap on both reconstructed FSs. In the second case, there is a sign change of the superconducting gap between the inner and outer FSs.

We also showed that the evolution of the nodes with increasing inter-pocket pairing interaction is rather non-trivial, and in the intermediate regime the number of nodal points may increase from 8 to 16. We also found that the eccentricity of the pockets enlarges the critical values of the hybridization parameters, partially protecting the nodal points from disappearing. The bottom line of this analysis is that strong hybridization lifts accidental nodes, but the resulting superconducting state may be highly non-trivial, particularly when the dominant effect of hybridization is the emergence of inter-pocket pairing potential.

Chapter 6

Conclusion and Discussion

In this dissertation I have presented theoretical studies of the gap structure in iron-based superconductors, with particular focus on the sign-changing s-wave symmetry of the gap function. The first half of the thesis was concerned with experimental implications of such gap structure, while the second half explored how this structure is modified by magnetism or hybridization (in the case of accidental nodes).

In Chapter 2 we studied the spin resonance at antiferromagnetic momentum (π, π) in an s^{+-} superconducting state of FeSCs by including the contribution from the particle-particle channel, which in the superconducting state gets mixed with the particle-hole channel. We showed that for purely repulsive interactions the inclusion of this channel does not qualitatively change the spin resonance, which remains predominantly spin-exciton and only slightly shifts to higher frequencies. For an attractive density-density interaction, when both the spin-exciton resonance in the particle-hole channel and the π-resonance in the particle-particle channel are allowed, we found that the strong coupling between the two channels destroys the two-peak structure and only one peak survives, whose frequency is smaller than would be that of a spin-exciton and $\pi-$resonance in the absence of the coupling. We also argued that the strong coupling between the particle-hole and particle-particle channels is peculiar to the spin susceptibility, while the coupling is much smaller for the charge susceptibility, which, for example, is relevant for Raman scattering.

In Chapter 3 we considered two results of Raman spectroscopy of FeSCs: the $1/(T - T_0)$ behavior of the B_{1g} Raman intensity in the normal state of $NaFe_{1-x}Co_xAs$,

$Ba(Fe_{1-x}Co_x)_2As_2$, $EuFe_2As_2$, and $SrFe_2As_2$ and the development of the resonance below T_c, observed in $NaFe_{1-x}Co_xAs$ and $Ba(Fe_{1-x}Co_x)_2As_2$. We argued that the coupling of the Raman vertex to pairs of magnetic fluctuations via the Abrikosov-Larkin process can explain both of them.

Specifically, we considered the Abrikosov-Larkin process in which light couples to a particle-hole pair, which then gets converted into a pair of spin fluctuations with momenta near $\mathbf{Q}_1 = (\pi, 0)$ and $\mathbf{Q}_2 = (0, \pi)$. We analyzed the magnetically mediated Raman intensity both analytically and numerically, first at the leading two-loop order and then included interactions between pairs of magnetic fluctuations. We demonstrated explicitly that the full Raman intensity in the B_{1g} channel can be viewed as the result of the coupling of light to the Ising-nematic susceptibility via the Aslamazov-Larkin process.

We argued that the $1/(T - T_0)$ temperature dependence in the normal state is the combination of the temperature dependence of the Aslamazov-Larkin vertex and of the Ising-nematic susceptibility. We further argued that the resonance in the B_{1g} channel below T_c emerges because of two effects. One is the development of a pole in the fully renormalized Ising-nematic susceptibility. The pole occurs at a frequency $\Omega_{res,1} < 2\Omega_{mag}$, where Ω_{mag} is the minimal frequency of a dispersing spin resonance at momenta near $Q_{1,2}$ in an s^{+-} superconductor. Another effect is that spin fluctuations generate attractive interactions between low-energy fermions, which constitute particle-hole bubbles with zero momentum transfer. An attractive interaction between such fermions combined with the fact that in an s-wave superconductor a particle-hole bubble at zero momentum transfer is singular at 2Δ gives rise to an excitonic resonance at $\Omega_{res,2} < 2\Delta$. In FeSCs $\Omega_{res,1}$ and $\Omega_{res,2}$ are not far from each other, and the observed strong peak in B_{1g} Raman intensity below T_c is likely the mixture of both effects.

In Chapter 4 we argued that a superconducting state, which explicitly breaks time-reversal symmetry, appears when superconductivity emerges from a pre-existing spin-density-wave-ordered state. We found that in the presence of spin-density-wave order, the spin-triplet channel with inter-pocket pairing couples to spin-singlet intra-pocket pairings on the reconstructed Fermi surfaces. This leads to the emergence of a new pairing channel, which we labeled as $t-$pairing to emphasize that it involves a spin-triplet component. We analyzed the interplay between s^{+-} and $t-$ superconducting

orders and showed that they coexist at low T with a relative phase $0 < \theta < \pi$. As a result, the phases of the gaps on different Fermi surfaces differ by less than a multiple of π. Such a state breaks time-reversal symmetry and has been long sought in the studies of iron-based superconductors. We argued that in a generic case this symmetry gets broken in the superconducting manifold at temperatures lower than T_c. This should give rise to features in experimentally probed thermodynamic quantities.

In Chapter 5 we investigated the effect of hybridization of the two electron pockets on the gap structure. We considered the case when the dominant pairing interaction is between hole and electron pockets and it yields an s^{+-} gap with accidental nodes on the electron pockets. Our goal was to understand how accidental nodes move once we include the hybridization.

We argued that for an s^{+-} superconductor hybridization gives rise to two effects: hopping between electron Fermi surfaces and the appearance of an additional pairing term which describes inter-pocket pairing. Each of these two effects shifts the position of the nodes and at large enough hybridization the nodes eventually disappear. However, the evolution of the nodes and the gap structure of the resulting nodeless state is different, depending on whether the inter-pocket hopping or the inter-pocket interaction is stronger. In the first case, the resulting state has the same sign of the gap on both reconstructed Fermi surfaces. In the second case, there is a sign change of the superconducting gap between the inner and outer Fermi surfaces.

We also showed that the evolution of the nodes with increasing inter-pocket pairing interaction is rather non-trivial, and in the intermediate regime the number of nodal points may increase from 8 to 16. We also found that the eccentricity of the pockets enlarges the critical values of the hybridization parameters, partially protecting the nodal points from disappearing. The bottom line of this analysis is that strong hybridization lifts accidental nodes, but the resulting superconducting state may be highly non-trivial, particularly when the dominant effect of hybridization is the emergence of inter-pocket pairing potential.

References

[1] D. N. Basov and Andrey Chubukov. Manifesto for a higher T_c. *Nature Physics*, 3:57–92, 2011.

[2] J. G. Bednorz and K. A. Müller. Possible high T_c superconductivity in the Ba-La-Cu-O system. *Zeitschrift für Physik B Condensed Matter*, 64(2):189–193.

[3] Yoichi Kamihara, Takumi Watanabe, Masahiro Hirano, and Hideo Hosono. Iron-based layered superconductor La[$O_{1-x}F_x$]FeAs (x = 0.050.12) with T_c = 26 K. *Journal of the American Chemical Society*, 130(11):3296–3297, 2008, http://dx.doi.org/10.1021/ja800073m. PMID: 18293989.

[4] Andrey Chubukov and Peter J. Hirschfeld. Iron-based superconductors, seven years later. *Physics today*, 68(11):46–52, 2015, http://dx.doi.org/10.1063/PT.3.2818.

[5] Alexander L. Fetter and John Dirk Walecka. *Quantum Theory of Many-Particle Systems*. Dover Publications, 2003.

[6] Michael Tinkham. *Introduction to superconductivity*. Dover Publications, 2nd edition, 1996.

[7] A. A. Abrikosov, L. P. Gorkov, and I. E. Dzyaloshinski. *Introduction to superconductivity*. Dover Publications, 1975.

[8] Andrey Chubukov. Pairing mechanism in Fe-based superconductors. *Annual Review of Condensed Matter Physics*, 3:57–92, 2012.

[9] A. A. Kordyuk. Iron-based superconductors: Magnetism, superconductivity, and electronic structure (review article). *Low Temperature Physics*, 38(9):888–899, 2012.

[10] Johnpierre Paglione and Richard L. Greene. High-temperature superconductivity in iron-based materials. *Nature Physics*, 6:645658, 2010.

[11] Alberto Hinojosa, Andrey V. Chubukov, and Peter Wölfle. Effect of pairing fluctuations on the spin resonance in Fe-based superconductors. *Phys. Rev. B*, 90:104509, Sep 2014.

[12] V. K. Thorsmølle, M. Khodas, Z. P. Yin, Chenglin Zhang, S. V. Carr, Pengcheng Dai, and G. Blumberg. Critical quadrupole fluctuations and collective modes in iron pnictide superconductors. *Phys. Rev. B*, 93:054515, Feb 2016.

[13] W.-L. Zhang, P. Richard, H. Ding, Athena S. Sefat, J. Gillett, Suchitra E. Sebastian, M. Khodas, and G. Blumberg. On the origin of the electronic anisotropy in iron pnicitde superconductors. *arXiv:1410.6452*, Oct 2014.

[14] Y.-X. Yang, Y. Gallais, R. M. Fernandes, I. Paul, L. Chauvière, M.-A. Méasson, M. Cazayous, A. Sacuto, D. Colson, and A. Forget. Raman scattering as a probe of charge nematic fluctuations in iron based superconductors. In *JPS Conference Proceedings*, volume 3 of *Proceedings of the International Conference on Strongly Correlated Electron Systems (SCES2013)*, Tokyo, Japan, 2013.

[15] B. Muschler, W. Prestel, R. Hackl, T. P. Devereaux, J. G. Analytis, Jiun-Haw Chu, and I. R. Fisher. Band- and momentum-dependent electron dynamics in superconducting $\mathrm{Ba(Fe_{1-x}Co_x)_2as_2}$ as seen via electronic Raman scattering. *Phys. Rev. B*, 80:180510, Nov 2009.

[16] Y. Gallais, R. M. Fernandes, I. Paul, L. Chauvière, Y.-X. Yang, M.-A. Méasson, M. Cazayous, A. Sacuto, D. Colson, and A. Forget. Observation of incipient charge nematicity in $\mathrm{ba(fe_{1-x}co_x)_2As_2}$. *Phys. Rev. Lett.*, 111:267001, Dec 2013.

[17] G. R. Boyd, T. P. Devereaux, P. J. Hirschfeld, V. Mishra, and D. J. Scalapino. Probing the pairing symmetry of the iron pnictides with electronic raman scattering. *Phys. Rev. B*, 79:174521, May 2009.

[18] G. R. Boyd, P. J. Hirschfeld, and T. P. Devereaux. Effect of disorder on the electronic raman scattering in the superconducting state of iron pnictides. *Phys. Rev. B*, 82:134506, Oct 2010.

[19] Alberto Hinojosa, Jiashen Cai, and Andrey V. Chubukov. Raman resonance in iron-based superconductors: The magnetic scenario. *Phys. Rev. B*, 93:075106, Feb 2016.

[20] Alberto Hinojosa, Rafael M. Fernandes, and Andrey V. Chubukov. Time-reversal symmetry breaking superconductivity in the coexistence phase with magnetism in Fe pnictides. *Phys. Rev. Lett.*, 113:167001, Oct 2014.

[21] Alberto Hinojosa and Andrey V. Chubukov. Gap structure in Fe-based superconductors with accidental nodes: The role of hybridization. *Phys. Rev. B*, 91:224502, Jun 2015.

[22] J. Rossat-Mignod, L.P. Regnault, C. Vettier, P. Bourges, P. Burlet, J. Bossy, J.Y. Henry, and G. Lapertot. Neutron scattering study of the $YBa_2Cu_3O_{6+x}$ system. *Physica C: Superconductivity*, 185:86 – 92, 1991.

[23] H. A. Mook, M. Yethiraj, G. Aeppli, T. E. Mason, and T. Armstrong. Polarized neutron determination of the magnetic excitations in $YBa_2Cu_3O_7$. *Phys. Rev. Lett.*, 70:3490–3493, May 1993.

[24] Hung Fai Fong, B. Keimer, P. W. Anderson, D. Reznik, F. Doğan, and I. A. Aksay. Phonon and magnetic neutron scattering at 41 mev in $YBa_2Cu_3O_7$. *Phys. Rev. Lett.*, 75:316–319, Jul 1995.

[25] HF Fong, Ph Bourges, Y Sidis, LP Regnault, A Ivanov, GD Gu, N Koshizuka, and B Keimer. Neutron scattering from magnetic excitations in $Bi_2Sr_2CaCu_2O_{8+\delta}$. *Nature*, 398(6728):588–591, 1999.

[26] Ph Bourges, Y Sidis, HF Fong, LP Regnault, J Bossy, A Ivanov, and B Keimer. The spin excitation spectrum in superconducting $YBa_2Cu_3O_{6.85}$. *Science*, 288(5469):1234–1237, 2000.

[27] H He, Ph Bourges, Y Sidis, C Ulrich, LP Regnault, S Pailhes, NS Berzigiarova, NN Kolesnikov, and B Keimer. Magnetic resonant mode in the single-layer high-temperature superconductor $Tl_2Ba_2CuO_{6+\delta}$. *Science*, 295(5557):1045–1047, 2002.

[28] G Yu, Y Li, EM Motoyama, and M Greven. A universal relationship between magnetic resonance and superconducting gap in unconventional superconductors. *Nature Physics*, 5(12):873–875, 2009.

[29] NK Sato, N Aso, K Miyake, R Shiina, P Thalmeier, G Varelogiannis, C Geibel, F Steglich, P Fulde, and T Komatsubara. Strong coupling between local moments and superconducting heavyelectrons in UPd_2Al_3. *Nature*, 410(6826):340–343, 2001.

[30] C Stock, C Broholm, J Hudis, Hye Jung Kang, and C Petrovic. Spin resonance in the d-wave superconductor $CeCoIn_5$. *Physical Review Letters*, 100(8):087001, 2008.

[31] AD Christianson, EA Goremychkin, R Osborn, S Rosenkranz, MD Lumsden, CD Malliakas, IS Todorov, H Claus, DY Chung, Mercouri G Kanatzidis, et al. Unconventional superconductivity in $Ba_{0.6}K_{0.4}Fe_2As_2$ from inelastic neutron scattering. *Nature*, 456(7224):930–932, 2008.

[32] Mark D Lumsden, Andrew D Christianson, Daniel Parshall, Matthew B Stone, Stephen E Nagler, GJ MacDougall, HA Mook, K Lokshin, T Egami, DL Abernathy, et al. Two-dimensional resonant magnetic excitation in $BaFe_{1.84}Co_{0.16}As_2$. *Physical Review Letters*, 102(10):107005, 2009.

[33] Songxue Chi, Astrid Schneidewind, Jun Zhao, Leland W Harriger, Linjun Li, Yongkang Luo, Guanghan Cao, Zhuan Xu, Micheal Loewenhaupt, Jiangping Hu, et al. Inelastic neutron-scattering measurements of a three-dimensional spin resonance in the FeAs-based $BaFe_{1.9}Ni_{0.1}As_2$ superconductor. *Physical review letters*, 102(10):107006, 2009.

[34] Shiliang Li, Ying Chen, Sung Chang, Jeffrey W Lynn, Linjun Li, Yongkang Luo, Guanghan Cao, Zhuan Xu, and Pengcheng Dai. Spin gap and magnetic resonance in superconducting $BaFe_{1.9}Ni_{0.1}As_2$. *Physical Review B*, 79(17):174527, 2009.

[35] DS Inosov, JT Park, P Bourges, DL Sun, Y Sidis, A Schneidewind, K Hradil, D Haug, CT Lin, B Keimer, et al. Normal-state spin dynamics and temperature-dependent spin-resonance energy in optimally doped $BaFe_{1.85}Co_{0.15}As_2$. *Nature Physics*, 6(3):178–181, 2010.

[36] J-P Castellan, S Rosenkranz, EA Goremychkin, DY Chung, IS Todorov, Mercouri G Kanatzidis, I Eremin, J Knolle, AV Chubukov, S Maiti, et al. Effect of fermi surface nesting on resonant spin excitations in $Ba_{1-x}K_xFe_2As_2$. *Physical review letters*, 107(17):177003, 2011.

[37] Yiming Qiu, Wei Bao, Yang Zhao, Collin Broholm, V Stanev, Z Tesanovic, YC Gasparovic, S Chang, Jin Hu, Bin Qian, et al. Spin gap and resonance at the nesting wave vector in superconducting $FeSe_{0.4}Te_{0.6}$. *Physical review letters*, 103(6):067008, 2009.

[38] DN Argyriou, A Hiess, A Akbari, I Eremin, MM Korshunov, Jin Hu, Bin Qian, Zhiqiang Mao, Yiming Qiu, Collin Broholm, et al. Incommensurate itinerant antiferromagnetic excitations and spin resonance in the $FeTe_{0.6}Se_{0.4}$ superconductor. *Physical Review B*, 81(22):220503, 2010.

[39] N Bulut and DJ Scalapino. Weak-coupling analysis of the neutron-scattering spectral weight. *Physical Review B*, 47(6):3419, 1993.

[40] II Mazin and Victor M Yakovenko. Neutron scattering and superconducting order parameter in $YBa_2Cu_3O_7$. *Physical review letters*, 75(22):4134, 1995.

[41] DZ Liu, Y Zha, and K Levin. Theory of neutron scattering in the normal and superconducting states of $YBa_2Cu_3O_{6+x}$. *Physical review letters*, 75(22):4130, 1995.

[42] N Bulut and DJ Scalapino. Neutron scattering from a collective spin fluctuation mode in a cuo 2 bilayer. *Physical Review B*, 53(9):5149, 1996.

[43] AJ Millis and H Monien. Bilayer coupling in the yttrium-barium family of high-temperature superconductors. *Physical Review B*, 54(22):16172, 1996.

[44] D Manske, I Eremin, and KH Bennemann. Analysis of the resonance peak and magnetic coherence seen in inelastic neutron scattering of cuprate superconductors: A consistent picture with tunneling and conductivity data. *Physical Review B*, 63(5):054517, 2001.

[45] M R Norman. Relation of neutron incommensurability to electronic structure in high-temperature superconductors. *Physical Review B*, 61(21):14751, 2000.

[46] MR Norman. Magnetic collective mode dispersion in high-temperature superconductors. *Physical Review B*, 63(9):092509, 2001.

[47] Andrey V Chubukov, Boldizsár Jankó, and Oleg Tchernyshyov. Dispersion of the neutron resonance in cuprate superconductors. *Physical Review B*, 63(18):180507, 2001.

[48] Ar Abanov, Andrey V Chubukov, and Jörg Schmalian. Fingerprints of spin mediated pairing in cuprates. *Journal of Electron Spectroscopy and Related Phenomena*, 117:129–151, 2001.

[49] F Onufrieva and P Pfeuty. Spin dynamics of a two-dimensional metal in a superconducting state: Application to the high-t c cuprates. *Physical Review B*, 65(5):054515, 2002.

[50] Ilya Eremin, Dirk K Morr, Andrey V Chubukov, KH Bennemann, and Michael R Norman. Novel neutron resonance mode in $d_{x^2-y^2}$-wave superconductors. *Physical review letters*, 94(14):147001, 2005.

[51] Ar Abanov, AV Chubukov, and MR Norman. Gap anisotropy and universal pairing scale in a spin-fluctuation model of cuprate superconductors. *Physical Review B*, 78(22):220507, 2008.

[52] O Tchernyshyov, MR Norman, and AV Chubukov. Neutron resonance in high-T_c superconductors is not the π particle. *Physical Review B*, 63(14):144507, 2001.

[53] MM Korshunov and I Eremin. Theory of magnetic excitations in iron-based layered superconductors. *Physical Review B*, 78(14):140509, 2008.

[54] Dirk K Morr and David Pines. The resonance peak in cuprate superconductors. *Physical review letters*, 81(5):1086, 1998.

[55] Jan Brinckmann and Patrick A Lee. Slave boson approach to neutron scattering in $YBa_2Cu_3O_{6+y}$ superconductors. *Physical review letters*, 82(14):2915, 1999.

[56] Matthias Eschrig. The effect of collective spin-1 excitations on electronic spectra in high-T_c superconductors. *Advances in Physics*, 55(1-2):47–183, 2006.

[57] AV Chubukov and LP Gorkov. Spin resonance in three-dimensional superconductors: The case of $CeCoIn_5$. *Physical review letters*, 101(14):147004, 2008.

[58] D Vollhardt and P Wolfle. *The phases of Helium 3*. Taylor and Francis, New York, 1990.

[59] S Graser, T A Maier, P J Hirschfeld, and D J Scalapino. Near-degeneracy of several pairing channels in multiorbital models for the Fe pnictides. *New Journal of Physics*, 11(2):025016, 2009.

[60] Douglas J Scalapino. A common thread: The pairing interaction for unconventional superconductors. *Reviews of Modern Physics*, 84(4):1383, 2012.

[61] Eugene Demler and Shou-Cheng Zhang. Theory of the resonant neutron scattering of high-T_c superconductors. *Physical review letters*, 75(22):4126, 1995.

[62] Eugene Demler, Hiroshi Kohno, and Shou-Cheng Zhang. π excitation of the $t-J$ model. *Physical Review B*, 58(9):5719, 1998.

[63] Eduardo Fradkin and Steven A Kivelson. High-temperature superconductivity: Ineluctable complexity. *Nature Physics*, 8(12):864–866, 2012.

[64] Patrick A Lee. Amperean pairing and the pseudogap phase of cuprate superconductors. *Physical Review X*, 4(3):031017, 2014.

[65] Daniel F Agterberg, Drew S Melchert, and Manoj K Kashyap. Emergent loop current order from pair density wave superconductivity. *Physical Review B*, 91(5):054502, 2015.

[66] Wei-Cheng Lee, Jairo Sinova, AA Burkov, Yogesh Joglekar, and AH MacDonald. Theory of reduced superfluid density in underdoped cuprate superconductors. *Physical Review B*, 77(21):214518, 2008.

[67] Wei-Cheng Lee and AH MacDonald. Weak-coupling theory of photoemission and inelastic neutron scattering and the mechanism of superconductivity in the cuprates. *Physical Review B*, 78(17):174506, 2008.

[68] I Fomin, P Schmitteckert, and P Wölfle. Comment on pseudospin symmetry and new collective modes of the hubbard model. *Physical review letters*, 69(1):214, 1992.

[69] Zhihao Hao and AV Chubukov. Resonance peak in neutron scattering experiments on the cuprates revisited: The case of exciton versus π-resonance and magnetic plasmon. *Physical Review B*, 79(22):224513, 2009.

[70] I Eremin, G Zwicknagl, P Thalmeier, and P Fulde. Feedback spin resonance in superconducting $CeCu_2Si_2$ and $CeCoIn_5$. *Physical review letters*, 101(18):187001, 2008.

[71] Seiichiro Onari and Hiroshi Kontani. Neutron inelastic scattering peak by dissipationless mechanism in the s^{++}-wave state in iron-based superconductors. *Physical Review B*, 84(14):144518, 2011.

[72] II Mazin and J Schmalian. Pairing symmetry and pairing state in ferropnictides: Theoretical overview. *Physica C: Superconductivity*, 469(9):614–627, 2009.

[73] Andrey V Chubukov, DV Efremov, and Ilya Eremin. Magnetism, superconductivity, and pairing symmetry in iron-based superconductors. *Physical Review B*, 78(13):134512, 2008.

[74] AV Chubukov, MG Vavilov, and AB Vorontsov. Momentum dependence and nodes of the superconducting gap in the iron pnictides. *Physical Review B*, 80(14):140515, 2009.

[75] Alexander F Kemper, Thomas A Maier, Siegfried Graser, Hai-Ping Cheng, PJ Hirschfeld, and DJ Scalapino. Sensitivity of the superconducting state and magnetic susceptibility to key aspects of electronic structure in ferropnictides. *New Journal of Physics*, 12(7):073030, 2010.

[76] S Raghu, Xiao-Liang Qi, Chao-Xing Liu, DJ Scalapino, and Shou-Cheng Zhang. Minimal two-band model of the superconducting iron oxypnictides. *Physical Review B*, 77(22):220503, 2008.

[77] Andrey V Chubukov, DV Efremov, and Ilya Eremin. Magnetism, superconductivity, and pairing symmetry in iron-based superconductors. *Physical Review B*, 78(13):134512, 2008.

[78] M Khodas, AV Chubukov, and G Blumberg. Collective modes in multiband superconductors: Raman scattering in iron selenides. *Physical Review B*, 89(24):245134, 2014.

[79] B. Valenzuela, M. J. Calderón, G. León, and E. Bascones. Optical conductivity and Raman scattering of iron superconductors. *Phys. Rev. B*, 87:075136, Feb 2013.

[80] Andrey V. Chubukov, Ilya Eremin, and Maxim M. Korshunov. Theory of Raman response of a superconductor with extended s-wave symmetry: Application to the iron pnictides. *Phys. Rev. B*, 79:220501, Jun 2009.

[81] C. Sauer and G. Blumberg. Screening of the Raman response in multiband superconductors: Application to iron pnictides. *Phys. Rev. B*, 82:014525, Jul 2010.

[82] D. J. Scalapino and T. P. Devereaux. Collective d-wave exciton modes in the calculated Raman spectrum of Fe-based superconductors. *Phys. Rev. B*, 80:140512, Oct 2009.

[83] S. Sugai, Y. Mizuno, K. Kiho, M. Nakajima, C. H. Lee, A. Iyo, H. Eisaki, and S. Uchida. Pairing symmetry of the multiorbital pnictide superconductor $BaFe_{1.84}Co_{0.16}As_2$ from Raman scattering. *Phys. Rev. B*, 82:140504, Oct 2010.

[84] S. Sugai, Y. Mizuno, K. Kiho, M. Nakajima, C. H. Lee, A. Iyo, H. Eisaki, and S. Uchida. Erratum: Pairing symmetry of the multiorbital pnictide superconductor $BaFe_{1.84}Co_{0.16}As_2$ from Raman scattering [phys. rev. b **82** , 140504(r) (2010)]. *Phys. Rev. B*, 83:019903, Jan 2011.

[85] I. I. Mazin, T. P. Devereaux, J. G. Analytis, Jiun-Haw Chu, I. R. Fisher, B. Muschler, and R. Hackl. Pinpointing gap minima in $Ba(Fe_{0.94}Co_{0.06})_2As_2$ via band-structure calculations and electronic Raman scattering. *Phys. Rev. B*, 82:180502, Nov 2010.

[86] F. Kretzschmar, B. Muschler, T. Böhm, A. Baum, R. Hackl, Hai-Hu Wen, V. Tsurkan, J. Deisenhofer, and A. Loidl. Raman-scattering detection of nearly degenerate s-wave and d-wave pairing channels in iron-based $Ba_{0.6}K_{0.4}Fe_2As_2$ and $Rb_{0.8}Fe_{1.6}Se_2$ superconductors. *Phys. Rev. Lett.*, 110:187002, May 2013.

[87] M. V. Klein and S. B. Dierker. Theory of Raman scattering in superconductors. *Phys. Rev. B*, 29:4976–4991, May 1984.

[88] Thomas P. Devereaux and Rudi Hackl. Inelastic light scattering from correlated electrons. *Rev. Mod. Phys.*, 79:175–233, Jan 2007.

[89] T. Strohm and M. Cardona. Electronic Raman scattering in $YBa_2Cu_3O_7$ and other superconducting cuprates. *Phys. Rev. B*, 55:12725–12735, May 1997.

[90] SL Cooper and MV Klein. Light scattering studies of the low frequency excitation spectra of high temperature superconductors. *Comments Cond. Mat. Phys*, 15(2):99–124, 1990.

[91] RRP Singh. *Comments Cond. Mat. Phys*, 15:241, 1991.

[92] RM Fernandes, AV Chubukov, and J Schmalian. What drives nematic order in iron-based superconductors? *Nature physics*, 10(2):97–104, 2014.

[93] Yann Gallais and Indranil Paul. Charge nematicity and electronic Raman scattering in iron-based superconductors. *Comptes Rendus Physique*, 17(12):113 – 139, 2016. Iron-based superconductors / Supraconducteurs base de fer.

[94] Hiroyuki Yamase and Roland Zeyher. Electronic Raman scattering from orbital nematic fluctuations. *Physical Review B*, 88(12):125120, 2013.

[95] Hiroyuki Yamase and Roland Zeyher. Spin nematic fluctuations near a spin-density-wave phase. *New Journal of Physics*, 17(7):073030, 2015.

[96] G Blumberg. private communication.

[97] Yann Gallais, Indranil Paul, Ludivine Chauvière, and Jörg Schmalian. Nematic resonance in the Raman response of iron-based superconductors. *Phys. Rev. Lett.*, 116:017001, Jan 2016.

[98] Matthias Eschrig. The effect of collective spin-1 excitations on electronic spectra in high-T_c superconductors. *Advances in Physics*, 55(1-2):47–183, 2006.

[99] Youichi Yamakawa, Seiichiro Onari, and Hiroshi Kontani. Nematicity and magnetism in FeSe and other families of Fe-based superconductors. *Physical Review X*, 6(2):021032, 2016.

[100] AV Chubukov. Renormalization group analysis of competing orders and the pairing symmetry in Fe-based superconductors. *Physica C: Superconductivity*, 469(9):640–650, 2009.

[101] RM Fernandes, AV Chubukov, J Knolle, I Eremin, and J Schmalian. Preemptive nematic order, pseudogap, and orbital order in the iron pnictides. *Physical Review B*, 85(2):024534, 2012.

[102] S Caprara, C Di Castro, M Grilli, and D Suppa. Charge-fluctuation contribution to the Raman response in superconducting cuprates. *Physical review letters*, 95(11):117004, 2005.

[103] Hiroshi Kontani, Tetsuro Saito, and Seiichiro Onari. Origin of orthorhombic transition, magnetic transition, and shear-modulus softening in iron pnictide superconductors: Analysis based on the orbital fluctuations theory. *Physical Review B*, 84(2):024528, 2011.

[104] U. Karahasanovic, F. Kretzschmar, T. Böhm, R. Hackl, I. Paul, Y. Gallais, and J. Schmalian. Manifestation of nematic degrees of freedom in the Raman response function of iron pnictides. *Phys. Rev. B*, 92:075134, Aug 2015.

[105] M Khodas and A Levchenko. Raman scattering as a probe of nematic correlations. *Physical Review B*, 91(23):235119, 2015.

[106] Ar Abanov and Andrey V Chubukov. A relation between the resonance neutron peak and ARPES data in cuprates. *Physical review letters*, 83(8):1652, 1999.

[107] Chenglin Zhang, H.-F. Li, Yu Song, Yixi Su, Guotai Tan, Tucker Netherton, Caleb Redding, Scott V. Carr, Oleg Sobolev, Astrid Schneidewind, Enrico Faulhaber, L. W. Harriger, Shiliang Li, Xingye Lu, Dao-Xin Yao, Tanmoy Das, A. V. Balatsky, Th. Brückel, J. W. Lynn, and Pengcheng Dai. Distinguishing $s^{\pm}$ and s^{++} electron pairing symmetries by neutron spin resonance in superconducting $NaFe_{0.935}Co_{0.045}As$. *Phys. Rev. B*, 88:064504, Aug 2013.

[108] QQ Ge, ZR Ye, M Xu, Y Zhang, J Jiang, BP Xie, Y Song, CL Zhang, Pengcheng Dai, DL Feng, et al. Anisotropic but nodeless superconducting gap in the presence of spin-density wave in iron-pnictide superconductor $NaFe_{1-x}Co_xAs$. *Physical Review X*, 3(1):011020, 2013.

[109] K Terashima, Y Sekiba, JH Bowen, K Nakayama, T Kawahara, T Sato, P Richard, Y-M Xu, LJ Li, GH Cao, et al. Fermi surface nesting induced strong pairing in iron-based superconductors. *Proceedings of the National Academy of Sciences*, 106(18):7330–7333, 2009.

[110] Rafeal M Fernandes, Lindsay H VanBebber, Shobo Bhattacharya, Premala Chandra, Veerle Keppens, David Mandrus, Michael A McGuire, Brian C Sales, Athena S Sefat, and Joerg Schmalian. Effects of nematic fluctuations on the

elastic properties of iron arsenide superconductors. *Physical review letters*, 105(15):157003, 2010.

[111] Rafael M Fernandes and Jörg Schmalian. Manifestations of nematic degrees of freedom in the magnetic, elastic, and superconducting properties of the iron pnictides. *Superconductor Science and Technology*, 25(8):084005, 2012.

[112] Y. Zhang, C. He, Z. R. Ye, J. Jiang, F. Chen, M. Xu, Q. Q. Ge, B. P. Xie, J. Wei, M. Aeschlimann, X. Y. Cui, M. Shi, J. P. Hu, and D. L. Feng. Symmetry breaking via orbital-dependent reconstruction of electronic structure in detwinned NaFeAs. *Phys. Rev. B*, 85:085121, Feb 2012.

[113] C. He, Y. Zhang, B. P. Xie, X. F. Wang, L. X. Yang, B. Zhou, F. Chen, M. Arita, K. Shimada, H. Namatame, M. Taniguchi, X. H. Chen, J. P. Hu, and D. L. Feng. Electronic-structure-driven magnetic and structure transitions in superconducting NaFeAs single crystals measured by angle-resolved photoemission spectroscopy. *Phys. Rev. Lett.*, 105:117002, Sep 2010.

[114] ST Cui, SY Zhu, AF Wang, S Kong, SL Ju, XG Luo, XH Chen, GB Zhang, and Z Sun. Evolution of the band structure of superconducting NaFeAs from optimally doped to heavily overdoped Co substitution using angle-resolved photoemission spectroscopy. *Physical Review B*, 86(15):155143, 2012.

[115] Z.-H. Liu, P. Richard, K. Nakayama, G.-F. Chen, S. Dong, J.-B. He, D.-M. Wang, T.-L. Xia, K. Umezawa, T. Kawahara, S. Souma, T. Sato, T. Takahashi, T. Qian, Yaobo Huang, Nan Xu, Yingbo Shi, H. Ding, and S.-C. Wang. Unconventional superconducting gap in $NaFe_{0.95}Co_{0.05}As$ observed by angle-resolved photoemission spectroscopy. *Phys. Rev. B*, 84:064519, Aug 2011.

[116] I Paul. Nesting-induced large magnetoelasticity in the iron-arsenide systems. *Physical Review B*, 90(11):115102, 2014.

[117] Andrey Chubukov. *Itinerant Electron Scenario*, pages 255–329. Springer International Publishing, Cham, 2015.

[118] Ar Abanov, Andrey V Chubukov, and J Schmalian. Quantum-critical theory of the spin-fermion model and its application to cuprates: normal state analysis. *Advances in Physics*, 52(3):119–218, 2003.

[119] Valentin Stanev, Jian Kang, and Zlatko Tesanovic. Spin fluctuation dynamics and multiband superconductivity in iron pnictides. *Phys. Rev. B*, 78:184509, Nov 2008.

[120] Sevda Avci, Omar Chmaissem, JM Allred, S Rosenkranz, Ilya Eremin, Andrey V Chubukov, DE Bugaris, DY Chung, Mercouri G Kanatzidis, J-P Castellan, et al. Magnetically driven suppression of nematic order in an iron-based superconductor. *Nature communications*, 5, 2014.

[121] AE Böhmer, F Hardy, L Wang, T Wolf, P Schweiss, and C Meingast. Superconductivity-induced re-entrance of the orthorhombic distortion in $Ba_{1-x}K_xFe_2As_2$. *Nature communications*, 6, 2015.

[122] Xiaoyu Wang, Jian Kang, and Rafael M Fernandes. Magnetic order without tetragonal-symmetry-breaking in iron arsenides: Microscopic mechanism and spin-wave spectrum. *Physical Review B*, 91(2):024401, 2015.

[123] Jian Kang, Xiaoyu Wang, Andrey V. Chubukov, and Rafael M. Fernandes. Interplay between tetragonal magnetic order, stripe magnetism, and superconductivity in iron-based materials. *Phys. Rev. B*, 91:121104, Mar 2015.

[124] TA Maier and DJ Scalapino. Theory of neutron scattering as a probe of the superconducting gap in the iron pnictides. *Physical Review B*, 78(2):020514, 2008.

[125] Vladimir Cvetkovic and Oskar Vafek. Space group symmetry, spin-orbit coupling, and the low-energy effective Hamiltonian for iron-based superconductors. *Physical Review B*, 88(13):134510, 2013.

[126] Z Li, R Zhou, Y Liu, DL Sun, J Yang, CT Lin, and Guo-qing Zheng. Microscopic coexistence of antiferromagnetic order and superconductivity in $Ba_{0.77}K_{0.23}Fe_2As_2$. *Physical Review B*, 86(18):180501, 2012.

[127] R Zhou, Z Li, J Yang, DL Sun, CT Lin, and Guo-qing Zheng. Quantum criticality in electron-doped $BaFe_{2-x}Ni_xAs_2$. *Nature communications*, 4, 2013.

[128] DK Pratt, W Tian, A Kreyssig, JL Zarestky, S Nandi, N Ni, SL Budko, PC Canfield, AI Goldman, and RJ McQueeney. Coexistence of competing antiferromagnetic and superconducting phases in the underdoped $Ba(Fe_{0.953}Co_{0.047})_2As_2$ compound using x-ray and neutron scattering techniques. *Physical review letters*, 103(8):087001, 2009.

[129] I. I. Mazin, D. J. Singh, M. D. Johannes, and M. H. Du. Unconventional superconductivity with a sign reversal in the order parameter of $LaFeAsO_{1-x}F_x$. *Phys. Rev. Lett.*, 101:057003, Jul 2008.

[130] Kazuhiko Kuroki, Seiichiro Onari, Ryotaro Arita, Hidetomo Usui, Yukio Tanaka, Hiroshi Kontani, and Hideo Aoki. Unconventional pairing originating from the disconnected Fermi surfaces of superconducting $LaFeAsO_{1-x}F_x$. *Phys. Rev. Lett.*, 101:087004, Aug 2008.

[131] Vladimir Cvetkovic and Zlatko Tesanovic. Valley density-wave and multiband superconductivity in iron-based pnictide superconductors. *Phys. Rev. B*, 80:024512, Jul 2009.

[132] Junhua Zhang, Rastko Sknepnek, Rafael M Fernandes, and Jörg Schmalian. Orbital coupling and superconductivity in the iron pnictides. *Physical Review B*, 79(22):220502, 2009.

[133] PJ Hirschfeld, MM Korshunov, and II Mazin. Gap symmetry and structure of Fe-based superconductors. *Reports on Progress in Physics*, 74(12):124508, 2011.

[134] Wei-Cheng Lee, Shou-Cheng Zhang, and Congjun Wu. Pairing state with a time-reversal symmetry breaking in FeAs-based superconductors. *Phys. Rev. Lett.*, 102:217002, May 2009.

[135] Valentin Stanev and Zlatko Tešanović. Three-band superconductivity and the order parameter that breaks time-reversal symmetry. *Physical Review B*, 81(13):134522, 2010.

[136] Johan Carlström, Julien Garaud, and Egor Babaev. Length scales, collective modes, and type-1.5 regimes in three-band superconductors. *Physical Review B*, 84(13):134518, 2011.

[137] S. Maiti, M. M. Korshunov, and A. V. Chubukov. Gap symmetry in KFe_2As_2 and the cos 4θ gap component in LiFeAs. *Phys. Rev. B*, 85:014511, Jan 2012.

[138] T. A. Maier, P. J. Hirschfeld, and D. J. Scalapino. Evolution of the neutron resonances in AFe_2Se_2. *Phys. Rev. B*, 86:094514, Sep 2012.

[139] Christian Platt, Ronny Thomale, Carsten Honerkamp, Shou-Cheng Zhang, and Werner Hanke. Mechanism for a pairing state with time-reversal symmetry breaking in iron-based superconductors. *Physical Review B*, 85(18):180502, 2012.

[140] M Khodas and AV Chubukov. Interpocket pairing and gap symmetry in Fe-based superconductors with only electron pockets. *Physical review letters*, 108(24):247003, 2012.

[141] G. Livanas, A. Aperis, P. Kotetes, and G. Varelogiannis. Nematicity from mixed $s_{\pm} + d_{x^2-y^2}$ states in iron-based superconductors. *Phys. Rev. B*, 91:104502, Mar 2015.

[142] M Marciani, L Fanfarillo, Claudio Castellani, and L Benfatto. Leggett modes in iron-based superconductors as a probe of time-reversal symmetry breaking. *Physical Review B*, 88(21):214508, 2013.

[143] Fan Yang, Fa Wang, and Dung-Hai Lee. Fermiology, orbital order, orbital fluctuations, and Cooper pairing in iron-based superconductors. *Physical Review B*, 88(10):100504, 2013.

[144] ZP Yin, K Haule, and G Kotliar. Spin dynamics and orbital-antiphase pairing symmetry in iron-based superconductors. *Nature Physics*, 10(11):845–850, 2014.

[145] Ningning Hao and Jiangping Hu. Odd parity pairing and nodeless antiphase $s^{\pm}$ in iron-based superconductors. *Phys. Rev. B*, 89:045144, Jan 2014.

[146] Rafael M. Fernandes and Andrew J. Millis. Nematicity as a probe of superconducting pairing in iron-based superconductors. *Phys. Rev. Lett.*, 111:127001, Sep 2013.

[147] Saurabh Maiti and Andrey V Chubukov. $s + is$ state with broken time-reversal symmetry in Fe-based superconductors. *Physical Review B*, 87(14):144511, 2013.

[148] F. Ahn, I. Eremin, J. Knolle, V. B. Zabolotnyy, S. V. Borisenko, B. Büchner, and A. V. Chubukov. Superconductivity from repulsion in LiFeAs: Novel s-wave symmetry and potential time-reversal symmetry breaking. *Phys. Rev. B*, 89:144513, Apr 2014.

[149] Valentin Stanev. Model of collective modes in three-band superconductors with repulsive interband interactions. *Physical Review B*, 85(17):174520, 2012.

[150] Shi-Zeng Lin and Xiao Hu. Massless Leggett mode in three-band superconductors with time-reversal-symmetry breaking. *Physical review letters*, 108(17):177005, 2012.

[151] Congjun Wu and JE Hirsch. Mixed triplet and singlet pairing in ultracold multicomponent fermion systems with dipolar interactions. *Physical Review B*, 81(2):020508, 2010.

[152] S. Avci, O. Chmaissem, E. A. Goremychkin, S. Rosenkranz, J.-P. Castellan, D. Y. Chung, I. S. Todorov, J. A. Schlueter, H. Claus, M. G. Kanatzidis, A. Daoud-Aladine, D. Khalyavin, and R. Osborn. Magnetoelastic coupling in the phase diagram of $Ba_{1-x}K_xFe_2As_2$ as seen via neutron diffraction. *Phys. Rev. B*, 83:172503, May 2011.

[153] M-H Julien, H Mayaffre, M Horvatić, C Berthier, XD Zhang, W Wu, GF Chen, NL Wang, and JL Luo. Homogeneous vs. inhomogeneous coexistence of magnetic order and superconductivity probed by NMR in Co-and K-doped iron pnictides. *EPL (Europhysics Letters)*, 87(3):37001, 2009.

[154] Erwin Wiesenmayer, Hubertus Luetkens, Gwendolyne Pascua, Rustem Khasanov, Alex Amato, Heidi Potts, Benjamin Banusch, Hans-Henning Klauss, and Dirk

Johrendt. Microscopic coexistence of superconductivity and magnetism in $Ba_{1-x}K_xFe_2As_2$. *Phys. Rev. Lett.*, 107:237001, Nov 2011.

[155] P. Marsik, K. W. Kim, A. Dubroka, M. Rössle, V. K. Malik, L. Schulz, C. N. Wang, Ch. Niedermayer, A. J. Drew, M. Willis, T. Wolf, and C. Bernhard. Coexistence and competition of magnetism and superconductivity on the nanometer scale in underdoped $BaFe_{1.89}Co_{0.11}As_2$. *Phys. Rev. Lett.*, 105:057001, Jul 2010.

[156] Long Ma, G. F. Ji, Jia Dai, X. R. Lu, M. J. Eom, J. S. Kim, B. Normand, and Weiqiang Yu. Microscopic coexistence of superconductivity and antiferromagnetism in underdoped $Ba(Fe_{1-x}Ru_x)_2As_2$. *Phys. Rev. Lett.*, 109:197002, Nov 2012.

[157] Peng Cai, Xiaodong Zhou, Wei Ruan, Aifeng Wang, Xianhui Chen, Dung-Hai Lee, and Yayu Wang. Visualizing the microscopic coexistence of spin density wave and superconductivity in underdoped $NaFe_{1-x}Co_xAs$. *Nature communications*, 4:1596, 2013.

[158] Q. Q. Ge, Z. R. Ye, M. Xu, Y. Zhang, J. Jiang, B. P. Xie, Y. Song, C. L. Zhang, Pengcheng Dai, and D. L. Feng. Anisotropic but nodeless superconducting gap in the presence of spin-density wave in iron-pnictide superconductor $NaFe_{1-x}Co_xAs$. *Phys. Rev. X*, 3:011020, Mar 2013.

[159] M Yi, Y Zhang, Z-K Liu, X Ding, J-H Chu, AF Kemper, N Plonka, B Moritz, M Hashimoto, S-K Mo, et al. Dynamic competition between spin-density wave order and superconductivity in underdoped $Ba_{1-x}K_xFe_2As_2$. *Nature communications*, 5, 2014.

[160] GC Psaltakis and EW Fenton. Superconductivity and spin-density waves: organic superconductors. *Journal of Physics C: Solid State Physics*, 16(20):3913, 1983.

[161] Masakazu Murakami and Hidetoshi Fukuyama. Backward scattering and coexistent state in two-dimensional electron system. *Journal of the Physical Society of Japan*, 67(8):2784–2791, 1998.

[162] Bumsoo Kyung. Mean-field study of the interplay between antiferromagnetism and d-wave superconductivity. *Phys. Rev. B*, 62:9083–9088, Oct 2000.

[163] A Aperis, G Varelogiannis, P B Littlewood, and B D Simons. Coexistence of spin density wave, d-wave singlet and staggered π-triplet superconductivity. *Journal of Physics: Condensed Matter*, 20(43):434235, 2008.

[164] J-P Ismer, Ilya Eremin, Enrico Rossi, Dirk K Morr, and G Blumberg. Theory of multiband superconductivity in spin-density-wave metals. *Physical review letters*, 105(3):037003, 2010.

[165] Kazuhiro Kuboki and Keiji Yano. Microscopic derivation of Ginzburg–Landau equations for coexistent states of superconductivity and magnetism. *Journal of the Physical Society of Japan*, 81(6):064711, 2012.

[166] W Rowe, I Eremin, A T Rmer, B M Andersen, and P J Hirschfeld. Doping asymmetry of superconductivity coexisting with antiferromagnetism in spin fluctuation theory. *New Journal of Physics*, 17(2):023022, 2015.

[167] D Parker, MG Vavilov, AV Chubukov, and II Mazin. Coexistence of superconductivity and a spin-density wave in pnictide superconductors: Gap symmetry and nodal lines. *Physical Review B*, 80(10):100508, 2009.

[168] Pouyan Ghaemi and Ashvin Vishwanath. Anomalous Zeeman response of the coexisting superconducting and spin-density-wave phases as a probe of extended s-wave pairing in ferropnictide superconductors. *Physical Review B*, 83(22):224513, 2011.

[169] AB Vorontsov, MG Vavilov, and AV Chubukov. Interplay between magnetism and superconductivity in the iron pnictides. *Physical Review B*, 79(6):060508, 2009.

[170] A. B. Vorontsov, M. G. Vavilov, and A. V. Chubukov. Superconductivity and spin-density waves in multiband metals. *Phys. Rev. B*, 81:174538, May 2010.

[171] Rafael M Fernandes, Daniel K Pratt, Wei Tian, Jerel Zarestky, Andreas Kreyssig, Shibabrata Nandi, Min Gyu Kim, Alex Thaler, Ni Ni, Paul C Canfield, et al. Unconventional pairing in the iron arsenide superconductors. *Physical Review B*, 81(14):140501, 2010.

[172] Rafael M Fernandes and Jörg Schmalian. Transfer of optical spectral weight in magnetically ordered superconductors. *Physical Review B*, 82(1):014520, 2010.

[173] Johannes Knolle, I Eremin, J Schmalian, and R Moessner. Magnetic resonance from the interplay of frustration and superconductivity. *Physical Review B*, 84(18):180510, 2011.

[174] S Maiti, RM Fernandes, and AV Chubukov. Gap nodes induced by coexistence with antiferromagnetism in iron-based superconductors. *Physical Review B*, 85(14):144527, 2012.

[175] Weicheng Lv, Adriana Moreo, and Elbio Dagotto. Double magnetic resonance and spin anisotropy in Fe-based superconductors due to static and fluctuating antiferromagnetic orders. *Physical Review B*, 89(10):104510, 2014.

[176] Jacob Schmiedt, PMR Brydon, and Carsten Timm. Superconducting pairing in the spin-density-wave phase of iron pnictides. *Physical Review B*, 89(5):054515, 2014.

[177] Ilya Eremin and Andrey V Chubukov. Magnetic degeneracy and hidden metallicity of the spin-density-wave state in ferropnictides. *Physical Review B*, 81(2):024511, 2010.

[178] RM Fernandes, AV Chubukov, J Knolle, I Eremin, and J Schmalian. Preemptive nematic order, pseudogap, and orbital order in the iron pnictides. *Physical Review B*, 85(2):024534, 2012.

[179] Saurabh Maiti and Andrey V Chubukov. Renormalization group flow, competing phases, and the structure of superconducting gap in multiband models of iron-based superconductors. *Physical Review B*, 82(21):214515, 2010.

[180] Christian Platt, Werner Hanke, and Ronny Thomale. Functional renormalization group for multi-orbital Fermi surface instabilities. *Advances in Physics*, 62(4-6):453–562, 2013.

[181] S. Kasahara, T. Shibauchi, K. Hashimoto, K. Ikada, S. Tonegawa, R. Okazaki, H. Shishido, H. Ikeda, H. Takeya, K. Hirata, T. Terashima, and Y. Matsuda.

Evolution from non-Fermi- to Fermi-liquid transport via isovalent doping in $BaFe_2(As_{1-x}P_x)_2$ superconductors. *Phys. Rev. B*, 81:184519, May 2010.

[182] Ying Ran, Fa Wang, Hui Zhai, Ashvin Vishwanath, and Dung-Hai Lee. Nodal spin density wave and band topology of the FeAs-based materials. *Physical Review B*, 79(1):014505, 2009.

[183] J Knolle, I Eremin, and R Moessner. Multiorbital spin susceptibility in a magnetically ordered state: Orbital versus excitonic spin density wave scenario. *Physical Review B*, 83(22):224503, 2011.

[184] Rahul Nandkishore, LS Levitov, and AV Chubukov. Chiral superconductivity from repulsive interactions in doped graphene. *Nature Physics*, 8(2):158–163, 2012.

[185] MG Vavilov and AV Chubukov. Phase diagram of iron pnictides if doping acts as a source of disorder. *Physical Review B*, 84(21):214521, 2011.

[186] RM Fernandes, MG Vavilov, and AV Chubukov. Enhancement of T_c by disorder in underdoped iron pnictide superconductors. *Physical Review B*, 85(14):140512, 2012.

[187] Mareike Hoyer, Sergey V Syzranov, and Jörg Schmalian. Effect of weak disorder on the phase competition in iron pnictides. *Physical Review B*, 89(21):214504, 2014.

[188] Yuxuan Wang and Andrey Chubukov. Charge-density-wave order with momentum $(2Q, 0)$ and $(0, 2Q)$ within the spin-fermion model: Continuous and discrete symmetry breaking, preemptive composite order, and relation to pseudogap in hole-doped cuprates. *Phys. Rev. B*, 90:035149, Jul 2014.

[189] Troels Arnfred Bojesen, Egor Babaev, and Asle Sudbø. Phase transitions and anomalous normal state in superconductors with broken time-reversal symmetry. *Physical Review B*, 89(10):104509, 2014.

[190] M. Yamashita, Y. Senshu, T. Shibauchi, S. Kasahara, K. Hashimoto, D. Watanabe, H. Ikeda, T. Terashima, I. Vekhter, A. B. Vorontsov, and Y. Matsuda. Nodal

gap structure of superconducting $BaFe_2(As_{1-x}P_x)_2$ from angle-resolved thermal conductivity in a magnetic field. *Phys. Rev. B*, 84:060507, Aug 2011.

[191] AI Coldea, JD Fletcher, A Carrington, JG Analytis, AF Bangura, J-H Chu, AS Erickson, IR Fisher, NE Hussey, and RD McDonald. Fermi surface of superconducting LaFePO determined from quantum oscillations. *Physical review letters*, 101(21):216402, 2008.

[192] S Kasahara, K Hashimoto, H Ikeda, T Terashima, Y Matsuda, and T Shibauchi. Contrasts in electron correlations and inelastic scattering between LiFeP and LiFeAs revealed by charge transport. *Physical Review B*, 85(6):060503, 2012.

[193] K Hashimoto, S Kasahara, R Katsumata, Y Mizukami, M Yamashita, H Ikeda, T Terashima, A Carrington, Y Matsuda, and T Shibauchi. Nodal versus nodeless behaviors of the order parameters of LiFeP and LiFeAs superconductors from magnetic penetration-depth measurements. *Physical review letters*, 108(4):047003, 2012.

[194] S Maiti, MM Korshunov, TA Maier, PJ Hirschfeld, and AV Chubukov. Evolution of symmetry and structure of the gap in iron-based superconductors with doping and interactions. *Physical Review B*, 84(22):224505, 2011.

[195] Katsuhiro Suzuki, Hidetomo Usui, and Kazuhiko Kuroki. Possible three-dimensional nodes in the s^{+-} superconducting gap of $BaFe_2(As_{1-x}P_x)_2$. *Journal of the Physical Society of Japan*, 80(1):013710, 2011, http://dx.doi.org/10.1143/JPSJ.80.013710.

[196] Tetsuro Saito, Seiichiro Onari, and Hiroshi Kontani. Emergence of fully gapped s_{++}-wave and nodal d-wave states mediated by orbital and spin fluctuations in a ten-orbital model of KFe_2Se_2. *Phys. Rev. B*, 83:140512, Apr 2011.

[197] Chia-Hui Lin, Tom Berlijn, Limin Wang, Chi-Cheng Lee, Wei-Guo Yin, and Wei Ku. One-Fe versus two-Fe Brillouin zone of Fe-based superconductors: Creation of the electron pockets by translational symmetry breaking. *Physical review letters*, 107(25):257001, 2011.

[198] Jiangping Hu and Ningning Hao. S_4 symmetric microscopic model for iron-based superconductors. *Phys. Rev. X*, 2:021009, May 2012.

[199] MJ Calderón, B Valenzuela, and E Bascones. Tight-binding model for iron pnictides. *Physical Review B*, 80(9):094531, 2009.

[200] A. Moreo, M. Daghofer, J. A. Riera, and E. Dagotto. Properties of a two-orbital model for oxypnictide superconductors: Magnetic order, B_{2g} spin-singlet pairing channel, and its nodal structure. *Phys. Rev. B*, 79:134502, Apr 2009.

[201] Maria Daghofer, Andrew Nicholson, Adriana Moreo, and Elbio Dagotto. Three orbital model for the iron-based superconductors. *Physical Review B*, 81(1):014511, 2010.

[202] Takashi Miyake, Kazuma Nakamura, Ryotaro Arita, and Masatoshi Imada. Comparison of ab initio low-energy models for LaFePO, LaFeAsO, $BaFe_2As_2$, LiFeAs, FeSe, and FeTe: electron correlation and covalency. *Journal of the Physical Society of Japan*, 79(4):044705, 2010.

[203] M Khodas and AV Chubukov. Vertical loop nodes in iron-based superconductors. *Physical Review B*, 86(14):144519, 2012.

[204] F Ahn, I Eremin, J Knolle, VB Zabolotnyy, SV Borisenko, B Büchner, and AV Chubukov. Superconductivity from repulsion in LiFeAs: Novel s-wave symmetry and potential time-reversal symmetry breaking. *Physical Review B*, 89(14):144513, 2014.

[205] II Mazin. Symmetry analysis of possible superconducting states in $K_xFe_ySe_2$ superconductors. *Physical Review B*, 84(2):024529, 2011.

[206] I. A. Nekrasov, Z. V. Pchelkina, and M. V. Sadovskii. Electronic structure of prototype AFe2As2 and ReOFeAs high-temperature superconductors: A comparison. *JETP Letters*, 88(2):144–149, 2008.

[207] Y. Su, P. Link, A. Schneidewind, Th. Wolf, P. Adelmann, Y. Xiao, M. Meven, R. Mittal, M. Rotter, D. Johrendt, Th. Brueckel, and M. Loewenhaupt. Antiferromagnetic ordering and structural phase transition in $Ba_2Fe_2As_2$ with Sn incorporated from the growth flux. *Phys. Rev. B*, 79:064504, Feb 2009.

[208] Jiangang Guo, Shifeng Jin, Gang Wang, Shunchong Wang, Kaixing Zhu, Tingting Zhou, Meng He, and Xiaolong Chen. Superconductivity in the iron selenide $K_xFe_2Se_2$ ($0 \leq x \leq 1.0$). *Phys. Rev. B*, 82:180520, Nov 2010.

[209] Amalia I Coldea. Quantum oscillations probe the normal electronic states of novel superconductors. *Philosophical Transactions of the Royal Society of London A: Mathematical, Physical and Engineering Sciences*, 368(1924):3503–3517, 2010.

[210] A Carrington, AI Coldea, JD Fletcher, NE Hussey, CMJ Andrew, AF Bangura, JG Analytis, J-H Chu, AS Erickson, IR Fisher, et al. Quantum oscillation studies of the fermi surface of LaFePO. *Physica C: Superconductivity*, 469(9):459–468, 2009.

Appendix A

Glossary and Acronyms

Care has been taken in this thesis to minimize the use of jargon and acronyms, but this cannot always be achieved. This appendix defines jargon terms in a glossary, and contains a table of acronyms and their meaning.

A.1 Glossary

- **Exciton** – A bound state of an electron and a hole in a many-body system.
- **Critical temperature** (T_c) – The temperature below which a material is superconducting.

A.2 Acronyms

Table A.1: Acronyms

Acronym	Meaning
BCS	Bardeen-Cooper-Schrieffer
BZ	Brillouin zone
FeSCs	Iron-based superconductors
FS	Fermi surface

Continued on next page

Table A.1 – continued from previous page

Acronym	Meaning
RPA	Random phase approximation
SC	Superconductivity (or superconducting)
SDW	Spin density wave
T	Temperature
T_c	Critical temperature (see above)